Max-Planck-Institut für Intelligente Systeme
(**ehemals Max-Planck-Institut für Metallforschung**)
Stuttgart

Nitriding of iron-based ternary alloys: Fe-Cr-Ti and Fe-Cr-Al

Kyung Sub Jung

Dissertation
an der

Universität Stuttgart

Bericht Nr. 234
April 2011

Nitriding of iron-based ternary alloys:
Fe-Cr-Ti and Fe-Cr-Al

von der Fakultät Chemie der Universität Stuttgart
zur Erlangung der Würde eines Doktors der
Naturwissenschaften (Dr. rer. nat.) genehmigte Abhandlung

vorgelegt von

Kyung Sub Jung

aus Busan/South Korea

Hauptberichter:	Prof. Dr. Ir. E. J. Mittemeijer
Mitberichter:	Prof. Dr. J. Bill
Prüfungsvorsitzender:	Prof. Dr. Th. Schleid

Tag der Einreichung:	27.12.2010
Tag der mündlichen Prüfung:	07.04.2011

MAX-PLANCK-INSTITUT FÜR INTELLIGENTE SYSTEME, STUTTGART
(ehemals MAX-PLANCK-INSTITUT FÜR METALLFORSCHUNG)
MATERIALWISSENSCHAFT DER UNIVERSITÄT, STUTTGART

STUTTGART, 2011

Contents

Chapter 1

Introduction

1.1 General introduction

To improve mechanical (i.e. hardness increase, fatigue and wear resistance) and chemical (i.e. corrosion resistance) properties of ferritic iron-based alloys and/or steel components, nitriding is one of the oldest and most important thermochemical surface treatments by which nitrogen is introduced into ferritic steel components at elevated temperatures (typically between 500 - 580°C [1, 2]).

As compared with a purely thermal surface treatment involving the austenite-martensite transition, nitriding is associated with a very small volumetric distortion of the workpiece, i.e. it provides excellent control of the workpiece dimensions, and therefore is widely adopted in industry.

The nitrided zone of ferritic iron-based alloys usually consists of (i) a compound layer (i.e. "white layer", due to its "white" appearance on light micrographs) at the specimen surface which is composed of iron nitrides (ε-$Fe_{2-3}N$ and/or γ'-Fe_4N), and (ii) the diffusion zone underneath the compound layer, where nitrogen is either dissolved or has precipitated as alloying element nitrides (cf. Fig. 1.1). The improvement of wear resistance and anti-corrosion properties is mainly attributed to the compound layer, while improvement of the fatigue resistance and hardness is mainly attributed to the interstitial nitrogen dissolved in the ferrite matrix and/or alloying element nitride precipitates developed in the diffusion zone.
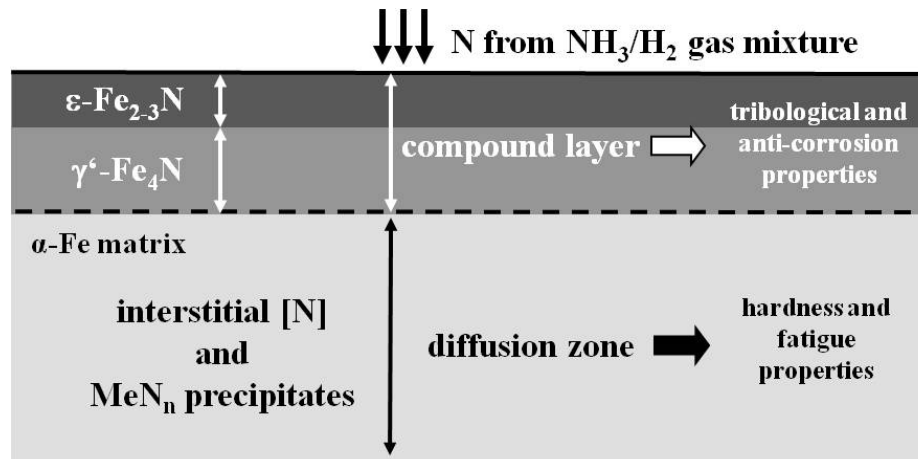
Fig. 1.1: Schematic illustration of the nitrided zone of an iron-based workpiece. The nitrided zone can be subdivided into the compound layer and the diffusion zone.

Typical nitriding steels are medium-carbon steels containing strong nitride-forming elements such as aluminium, chromium, titanium, vanadium and molybdenum.

In order to introduce nitrogen into ferritic workpieces two important requirements have to be fulfilled: (i) a nitrogen-concentration gradient, which can be established by keeping the nitrogen concentration at the specimen surface higher than underneath and (ii) an appropriate nitrogen diffusivity, which depends on the nitriding temperature. Against this background several methods are available to deliver nitrogen to the specimen, such as gaseous nitriding (employing a NH_3/H_2 gas mixture), salt bath (liquid) nitriding (employing cyanides and cyanates) and plasma nitriding (by ionizing by glow discharge a gas atmosphere of N_2 or a N_2/H_2 gas mixture).

Among several nitriding methods, gaseous nitriding is the most well-known and widely adopted technology, because of its possibility of precise tuning of the chemical potential of nitrogen during nitriding just by controlling nitriding temperature and nitriding potential, r_N [2].

The schematic view of the gaseous nitriding apparatus, which was used for the experimental work of the present thesis, is shown in Fig. 1.2.
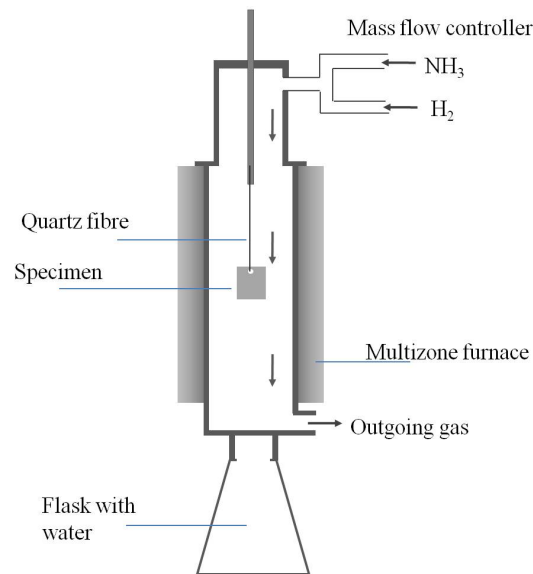
Fig. 1.2: Schematic view of gaseous nitriding apparatus consisting of vertical, multizone quartz-tube furnace, gas-flow installation controlled by a mass-flow controller and temperature controller for furnace.

It consists of a vertical, multi-zone quartz-tube furnace, which allows a precise temperature control within ± 1K in each temperature zone (three in number). Mass-flow controllers which adjust the mass flow of the components of the nitriding gas mixture (i.e. ammonia and hydrogen).

The specimen is suspended on a rod with a quartz fiber and centered in the furnace. The nitriding process is stopped by breaking the quartz fiber mechanically in the furnace so that the specimen can fall through an opened valve into a water-filled flask which is flushed with pure nitrogen gas in order to avoid possible oxidation of the specimen during quenching.

The gaseous nitriding atmosphere consists of an ammonia/hydrogen gas mixture at an elevated temperature. During gaseous nitriding of ferritic iron-based alloys, a local equilibrium exists between the specimen surface and an atmospheric ammonia/hydrogen gas mixture. The introduced ammonia dissociates at the specimen

surface according to a catalytic reaction and thus released nitrogen atoms diffuse into the specimen.

1.2 Thermodynamics of gaseous nitriding

Pure N_2 gas as a nitrogen donating medium is not suitable for gaseous nitriding because the nitrogen activity at atmospheric pressure is much too low [2, 3].

The gaseous nitriding of α-Fe under a gas mixture comprising NH_3/H_2 at a given nitriding temperature can be characterized by the following overall reaction at the specimen surface:

$$NH_3 \Leftrightarrow N_\alpha + \frac{3}{2} H_2 \qquad (1.1)$$

where N_α denotes nitrogen dissolved in the octahedral interstices of the α-Fe matrix. The equilibrium constant of the above reaction, K, is given by:

$$K = \frac{a_{N_\alpha} \cdot f_{H_2}^{3/2}}{f_{NH_3}} \qquad (1.2)$$

where a_{N_α} denotes the activity of dissolved nitrogen in the ferrite matrix, with respect to the reference state (in the reference state $a_{N_\alpha} = 1$) and f_i represents the fugacity of gas component i.

The chemical potential of a gas component i, μ_i, obeys:

$$\mu_i \equiv \mu_i^0 + RT \ln\left(\frac{f_i}{f_i^0}\right) \qquad (1.3)$$

where μ_i^0 denotes the chemical potential of the reference state of component i (μ_i^0 is temperature dependent at the selected pressure of the reference state), f_i represents the fugacity of gas component i (superscript "0" denotes the reference state), R is the gas constant and T is the absolute temperature.

The chemical potential of dissolved nitrogen in ferrite matrix, μ_{N_α}, satisfies:

$$\mu_{N_\alpha} \equiv \mu_{N_\alpha}^0 + RT \ln a_{N_\alpha} \tag{1.4}$$

where $\mu_{N_\alpha}^0$ denotes the chemical potential of the reference state of nitrogen dissolved in the ferrite matrix reference state (again temperature dependent at the selected pressure of the reference state). There are no prerequisites for the selection of the reference state. Therefore, the relevant reference state should always be specified when activities are discussed.

Considering ideal gases the fugacity of each gas component in Eq. (1.3) can be replaced by the partial pressure of each gas component, p_i, then setting the partial pressure of the reference state of each gas component at 1atm (i.e. p_i^0 = 1atm). Then Eq. (1.3) becomes:

$$\mu_i \equiv \mu_i^0 + RT \ln p_i \tag{1.5}$$

It should be emphasized that p_i must be expressed in the same unit as p_i^0 (here, atm).

By substitution of f_i by p_i in Eq. (1.2), it follows:

$$a_{N_\alpha} = K \cdot \left(\frac{p_{NH_3}}{p_{H_2}^{3/2}} \right) \tag{1.6}$$

In view of the relatively small amount of dissolved nitrogen, Henrian behavior can be assumed. Then the activity of nitrogen dissolved in the ferrite matrix is proportional with its concentration and thus:

$$c_N = K \cdot \frac{p_{NH_3}}{p_{H_2}^{3/2}} \tag{1.7}$$

where c_N denotes the concentration of nitrogen dissolved in pure α-Fe lattice, where K now incorporates the activity coefficient. The partial pressure ratio, $p_{NH_3} / p_{H_2}^{3/2}$ is referred to as the *nitriding potential* and is denoted by r_N. From Eq. (1.7) it can be

noticed that at constant temperature the amount of interstitially dissolved nitrogen in the ferrite matrix depends linearly on the nitriding potential, r_N.

The nitriding potential can be adjusted directly by the composition of the gas mixture in the furnace. The composition of the gas mixture (i.e. mole fractions of ammonia and hydrogen) can be controlled to a high degree of accuracy with well calibrated mass-flow controllers (variance within 1% of the adjusted value in ml/min). Besides nitriding temperature and time, the nitriding potential is the most decisive, independent parameter for a controlled nitriding processing.

1.3 The Fe-N phase diagram

The standard phase diagram which describes the thermodynamically "stable" phases of the Fe-N system as function of temperature and composition at constant pressure, is presented in Fig. 1.3a [4]. It is important to realize the Fig. 1.3a does not describe the equilibrium between Fe and N_2 at atmospheric pressure. In order to achieve gaseous nitriding by N_2 gas, N_2 pressures up to several thousand atmospheres have to be applied [2, 3].

Due to this practical impossibility of using N_2 gas for gaseous nitriding at atmospheric pressure, an ammonia/hydrogen gas mixture is used as a nitrogen donating medium (cf. section 1.2). The equilibrium phases at the specimen surface between pure α-Fe and an ammonia/hydrogen gas mixture have been determined by Lehrer [5]. Such a Lehrer diagram describes borders of the Fe-N phase field as function of temperature and nitriding potential, as shown in Fig. 1.3b. Besides the phase boundaries in the Lehrer diagram shown in Fig. 1.3b, additional lines of constant nitrogen concentration (i.e. isoconcentration lines) have been drawn [6].

According to the Lehrer diagram, distinction can be made of two cases; (i) *internal* nitriding and (ii) *external* nitriding. In the first case, nitrogen is only interstitially dissolved in the octahedral interstices of ferrite matrix and thus only a nitrogen diffusion zone can be established in the specimen (cf. Fig. 1.1). In the second case, iron nitrides (ϵ-$Fe_{2-3}N$ and/or γ'-Fe_4N) develop at the specimen surface, i.e. a compound layer occurs on top of the diffusion zone (cf. Fig. 1.1).
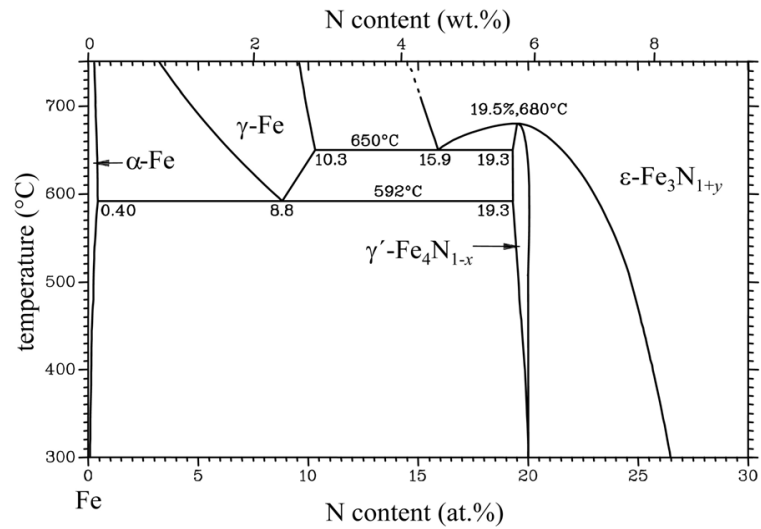
Fig. 1.3a: Part of the standard Fe-N phase diagram.
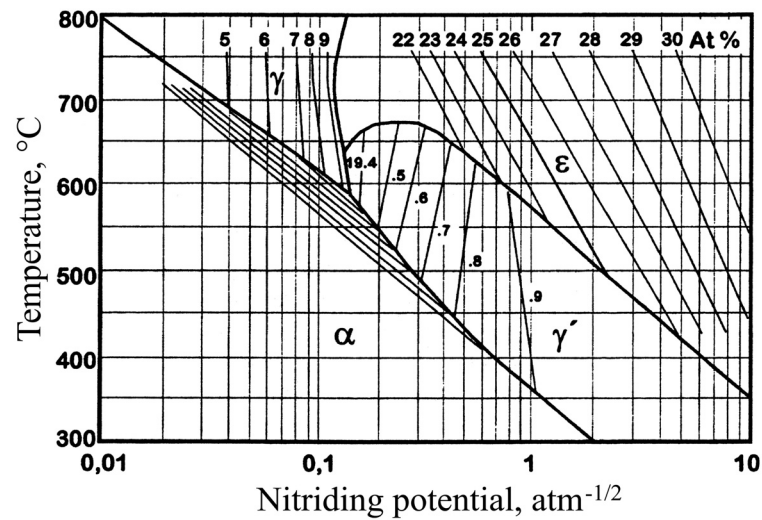
Fig. 1.3b: Equilibrium phases at the surface of pure α-Fe as function of temperature and nitriding potential.

1.4 Nitriding of Fe-Me alloys

During nitriding of iron-based ferritic Fe-Me alloys, where Me is an alloying element
which has a relatively high affinity for nitrogen, such as Ti [7-10], V [11-17], Cr [18-
24], Al [25-32] and Mo [33-36], nitride precipitates of the alloying elements develop in
the diffusion zone. The associated increases of hardness and fatigue resistance strongly
depend on the chemical composition of the precipitates, their morphology, size and
their coherency with the ferrite matrix.

The precipitation of MeN_n nitride can be written as:

$$NH_3 + Me_\alpha \Leftrightarrow MeN_n + \frac{3}{2}H_2 \tag{1.8}$$
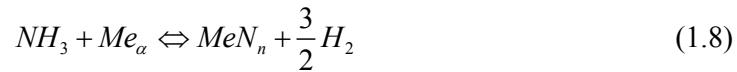
In many cases, the MeN_n nitride precipitates have a cubic, rock-salt type crystal-
structure (i.e. TiN [7, 10], VN [17] , CrN [24] and AlN [29]) and as, furthermore, the
lattice parameter of these nitride, a_{MeN_n} has a value close to $\sqrt{2} \cdot a_{\alpha-Fe}$ where $a_{\alpha-Fe}$ is
the lattice parameter of pure ferrite, then a Bain orientation relationship between nitride
precipitates and the ferrite matrix can be observed [17, 37, 38]:

$\{001\}_{MeNn}$ // $\{001\}_{\alpha-Fe}$ and $<110>_{MeNn}$ // $<100>_{\alpha-Fe}$

Due to the coherent nature of the interface ($\{001\}_{MeNn}$ // $\{001\}_{\alpha-Fe}$) between
nitride precipitates and ferrite matrix and the orientation relationship, a strong
anisotropic misfit-strain field is invoked. The misfit strain perpendicular to the habit
plane, $\delta\perp$ is very much larger than that parallel to the habit plane, $\delta_{//}$. As a consequence
the nitride precipitates develop as thin platelets.

Upon nitriding of Fe-Me alloys, the shape of the built-up nitrogen
concentration-depth profiles is influenced by the presence of alloying elements. A
parameter characterizing the strength of the interaction in ferrite matrix between
(substitutionally) dissolved alloying element (Me) and (interstitially) dissolved nitrogen

can be defined as the ratio of the energy gained (i.e. chemical Gibbs energy) and the energy lost (i.e. energy required: strain and interfacial Gibbs energies) on precipitation of the inner nitride [27, 38] .

An interaction parameter as defined above facilitates the understanding of two extremes of precipitation kinetics observed upon nitriding of a thin Fe-Me alloy specimen (see Fig. 1.4):

(i) *strong nitride formers*: after nitriding the microstructure is characterized by a relatively sharp interface between nitrided zone and unnitrided core. In the nitrided zone, practically all Me has precipitated. In the core nitrogen is virtually absent. Nitriding kinetics is predominantly controlled by diffusion of nitrogen in the ferrite. Alloying elements belonging to this category are Ti and V.

(ii) *weak nitride formers*: after nitriding the microstructure is characterized by a very diffuse (or no) case-core boundary in conjunction with a virtually constant nitrogen concentration. Nitriding kinetics is predominantly controlled by diffusion of the alloying elements in the ferrite matirx. Alloying elements belonging to this category are Al and Si.

(iii) *intermediate nitride formers*: depending on temperature and alloying-element concentration, nitriding behavior varying between those of the above mentioned, extreme cases can be obtained. Alloying elements belonging to this category are Cr and Mo.
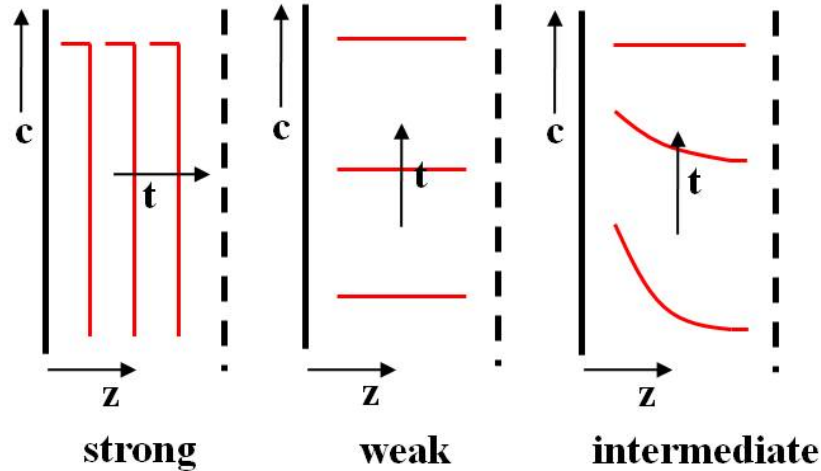
Fig. 1.4: Types of MeN interaction during nitriding of an Fe-Me alloy. C, t and z denote nitrogen concentration, nitriding time and depth below the specimen surface, respectively.

1.5 Excess nitrogen

Quantitative investigations (i.e. electron probe microanalysis and/or weight measurement) performed after nitriding revealed that the total amount of absorbed nitrogen (i.e. $[N]_{tot}$) in the Fe-Me alloys is larger than the amount of nitrogen necessary for the formation of the stoichiometric inner nitride precipitate (i.e. $[N]_{MeN_n}$) and realization of the equilibrium amount of dissolved nitrogen in the unstrained ferrite matrix (i.e. $[N]_\alpha^0$). The sum of the latter two contributions is known as the normal nitrogen (i.e. $[N]_{nor} = [N]_{MeN_n} + [N]_\alpha^0$). The additional amount of nitrogen is called excess nitrogen (i.e. $[N]_{ex} = [N]_{tot} - [N]_{nor}$) [8, 9].

1.5.1 Sites for the excess nitrogen; nitrogen-absorption isotherm

Excess nitrogen atoms can be located at several sites: (i) *adsorbed* at the coherent interface between the nitride precipitates and the ferrite matrix; $[N]_{interface}$ [8, 9, 37], (ii) additionally *dissolved* in octahedral interstices of the ferrite lattice strained owing to the

lattice misfit of inner nitride precipitates and the ferrite matrix; $[N]_{strain}$ [39] and (iii) trapped at dislocations; $[N]_{dislocation}$ [13]. Thus, if the Fe-Me alloys are nitrided under conditions such that no iron nitrides can be formed at the surface (i.e. in the α-region according to the Lehrer diagram, cf. Fig. 1.3b), the total nitrogen uptake of the alloy can be given as:

$$[N]_{tot} = [N]_\alpha^0 + [N]_{MeN_n} + [N]_{interface} + [N]_{strain} + [N]_{dislocation} \qquad (1.9)$$

The excess nitrogen, $[N]_{ex}$ can be further subdivided into two types according to their role during nitriding: (i) mobile excess nitrogen (i.e. $[N]_{strain}$) which participates in the diffusion process during nitriding, thus increasing the diffusion-zone depth and (ii) immobile excess nitrogen (i.e. $[N]_{interface}$ and $[N]_{dislocation}$) which is relatively strongly bonded to the alloying element nitrides and thus does not participate in the diffusion process (the amount of $[N]_{dislocation}$ can be neglected in recrystallized samples due to their relatively low dislocation density) [14, 20].

The total amount of nitrogen dissolved in nitrided Fe-Me alloys at a given nitriding temperature shows a linear behaviour as function of the nitriding potential, r_N according to Eq. (1.7). A nitrogen-absorption isotherm can be used to differentiate various kinds of differently (chemically) bonded nitrogen. Any point on a nitrogen-absorption isotherm indicates the equilibrium amount of nitrogen absorbed by the specimen at a given nitriding potential. To determine experimentally nitrogen-absorption isotherms, it is essential to establish a homogeneous, constant nitrogen content throughout the cross-section of the specimen. Further, the precipitation morphology should not change during determination of the absorption isotherm. Therefore a preceding pre-nitriding treatment is performed at a temperature higher than

applied for determination of the absorption isotherm, to ensure a constant precipitate morphology.

A nitrogen-absorption isotherm as determined for Fe-Me alloys can be schematically presented in Fig. 1.5a. The three types of absorbed nitrogen atoms can be discerned [8, 9]:

(i)   Type I: nitrogen strongly bonded to alloying element in the corresponding stoichiometric MeN_n nitride. As compared with nitrogen types II and III, this nitrogen cannot be removed by de-nitriding in a pure H_2 atmosphere. Type I nitrogen is indicated by level 'A' in Fig. 1.5a.

(ii)   Type II: nitrogen adsorbed at the nitride precipitates/ferrite matrix interface (i.e. $[N]_{interface}$). As compared to Type I nitrogen, this nitrogen is less strongly bonded and can be (partly) removed by de-nitriding (cf. Fig. 1.5b). As above mentioned, this nitrogen is called immobile excess nitrogen as it does not take part in the diffusion process. This type II nitrogen corresponds with the difference between levels 'B' and 'A' in Fig. 1.5a.

(iii)   Type III: nitrogen dissolved in the octahedral interstices of the ferrite matrix surrounding the precipitates (cf. Fig. 1.5c). According to the Eq. (1.7), the amount of interstitially dissolved nitrogen shows a linear dependence with the nitriding potential, r_N. The straight line dependence above level 'B' in Fig. 1.5a represents nitrogen dissolved interstitially in the ferrite matrix, (i.e.

$[N]_\alpha = [N]_{strain} + [N]_\alpha^0$). This type of nitrogen contributes to the diffusion of nitrogen and is easily removed by a de-nitriding treatment.
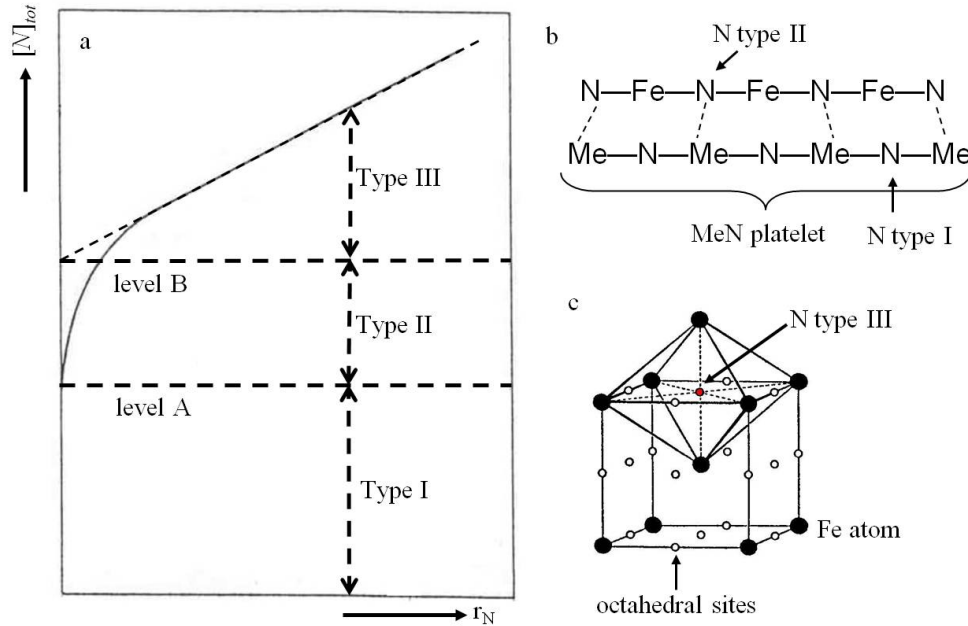
Fig. 1.5: (a) Schematic presentation of a nitrogen absorption isotherm, (b) The $(110)_{MeN}$ // $(100)_{\alpha\text{-Fe}}$ interface: (i) nitrogen bonded to Me atom to form MeN nitride (type I nitrogen) and (ii) nitrogen in octahedral interstices at the α-Fe matrix is adsorbed nitrogen which in direct contact with Me atom at the habit plane (type II nitrogen). (c) Type III nitrogen is dissolved in the α-Fe matrix and is incorporated in octahedral interstices of the α-Fe matrix.

1.5.2 Excess nitrogen adsorbed at the precipitate/matrix interface: $[N]_{interface}$

It has been suggested that large number of nitrogen atoms in nitrided Fe-Me binary alloy can be adsorbed at the (coherent) interfaces between the nitride precipitates and the ferrite matrix; $[N]_{interface}$ (cf. Fig. 1.5b) [8, 9, 14]. The amount of adsorbed nitrogen at the interface between nitride precipitates/ferrite matrix depends on: (i) total precipitate-matrix interfacial area (in general the larger interfacial area, the higher amount of $[N]_{interface}$), (ii) interface structure (i.e. structure and morphology of nitride

precipitates, their orientation relationship and degree of coherency with the ferrite matrix) and (iii) chemical affinity of alloying element and nitrogen.

The MeN precipitate with cubic, rock-salt crystal-structure type platelet with adsorbed nitrogen atoms at the broad faces of the nitride platelets can be regarded as a MeN_X compound as shown in Fig. 1.5b, i.e. (X-1) nitrogen atoms per MeN_X molecule are bonded/adsorbed to the coherent faces of the platelet:

$$X = \frac{[N]_{MeN} + [N]_{interface}}{[N]_{MeN}} \tag{1.10}$$

The value of X has a maximal value of 3 for a monolayer MeN precipitate platelet, assuming that at every octahedral interstice adjacent to the broad faces of the nitride platelet one excess nitrogen atom is trapped.

The value of X thus gives indirect information on the average thickness of the precipitate platelet. For MeN precipitates of cubic, rock-salt type crystal structure experiencing a Bain-type orientation relationship with the ferrite matrix, with $\{001\}_{\alpha\text{-Fe}}$ as habit plane, the thickness of a monolayer of MeN equals one half of the lattice parameter of the fcc unit cell of MeN, a_{MeN}. Assuming that at every octahedral interstice in the ferrite matrix *at* the interface one excess nitrogen atom is trapped, it follows:

$$X = \frac{n+2}{n} \tag{1.11}$$

where n is the number of MeN monolayers comprising the MeN platelet. Accordingly, the thickness of the MeN platelet is given by,

$$thickness = n \cdot (\frac{a_{MeN}}{2}) = \frac{2}{(X-1)} \cdot \frac{a_{MeN}}{2} \tag{1.12}$$

1.5.3 Excess nitrogen dissolved in the strained ferrite: $[N]_{strain}$

The presence of misfitting second phase particles can lead to elastic distortion of the surrounding matrix. The corresponding stress field (characterized by a tensile hydrostatic component [40, 41]) influences the thermodynamics of nitrogen dissolution in the ferrite-matrix. The ferrite-matrix lattice dilation generated by the misfitting inner nitride precipitates, due to the hydrostatic component of the image-stress field of finite bodies (i.e. ferrite matrix), provides a geometrical understanding for the occurrence of enhanced solubility of nitrogen. The enhancement of the lattice solubility, i.e. $[N]_{strain}$, with respect to that of the reference state (i.e. $[N]_{\alpha}^{0}$ for unstrained ferrite) can be given by [38]:

$$\frac{[N]_{\alpha}}{[N]_{\alpha}^{0}} = \exp\left[\frac{V_N}{RT}\left(\frac{4\varepsilon G_{\alpha}}{(1+\varepsilon)^3}CY_{MeN_X}^0\right)\right] \tag{1.13}$$

where $[N]_{\alpha} = [N]_{\alpha}^{0} + [N]_{strain}$ and with

misfit parameter:
$$\varepsilon = \frac{[V_{MeN} + (X-1)fV_{MeN}]^{1/3} - V_{\alpha}^{1/3}}{V_{\alpha}^{1/3}} \tag{1.14}$$

(elastic) constant:
$$C = \frac{3K_{MeN}}{(3K_{MeN} + 4G_{\alpha})} \tag{1.15}$$

and volume fraction of MeN$_x$:

$$Y_{MeN_X}^0 = \frac{[Me](V_{MeN} + (X-1)fV_{MeN})}{(1-[Me])V_{\alpha} + [Me](V_{MeN} + (X-1)fV_{MeN})} \tag{1.16}$$

where V_N is the partial molar volume of nitrogen dissolved in the ferrite matrix, V_{α} and V_{MeN} are the molar volumes of ferrite and the MeN precipitates, X is defined by Eq. (1.11), G_{α} is the shear modulus of the ferrite matrix, K_{MeN} is the bulk modulus of the MeN precipitate and $[Me]$ is the atomic fraction of alloying element in the specimen. The parameter f describes the extent to which the full misfit due to building out of the

lattice of the MeN precipitate by the adsorbed nitrogen atoms, which acts as an entity, is experienced ($0 \leq f \leq 1$).

1.6 Outlook of the thesis

Although nitriding has long been applied successfully in industry, a pronounced lack of fundamental knowledge exists, which obstructs a quantitative modeling of the nitriding process. Indeed, technological applications are still largely based on phenomenology. Hence, a strong need for fundamental research on nitriding can be identified.

Investigations of the precipitation behaviour of inner nitrides in the diffusion zone and the corresponding change of the material microstructure and hence material properties have been focused until now on relatively simple, binary Fe-Me alloys such as: Fe-Ti [7-10], Fe-V [11-17], Fe-Cr [18-24] and Fe-Al [25-32].

To understand the nitriding behaviour of commercial steel components, which contain more than one alloying element, the next step is investigation of iron-based ternary Fe-Me$_1$-Me$_2$ alloys. In the present study the nitriding behaviour of Fe-Cr-Ti and Fe-Cr-Al alloys was investigated. With Me$_1$ as Cr and Me$_2$ as Ti or Al, the nitriding behaviour of such ternary alloys was investigated.

At the beginning of the present work, different Fe-Cr-Me$_2$ (Me$_2$ = Al or Ti) alloys were (gas) nitrided followed by X-ray diffraction analysis (XRD), electron probe microanalysis (EPMA), microhardness measurement and classical metallography to get information about the inner nitride precipitate phases and the microstructure of the nitrided zone. Although the response of the alloy specimens upon exposure to the nitriding atmosphere was evident (i.e. plastic deformation of the specimens, brittleness, open grain boundaries and a significant hardness increase), it was difficult to identify the composition and microstructure of the inner nitride precipitates precisely with the

above mentioned methods due to their ultra-fine scale. The application of transmission electron microscopy methods (including electron energy loss spectroscopy (EELS)) finally provided detailed data on the microstructure and composition of the developed inner nitride precipitates.

Chapter 2 presents results concerning the investigation of the microstructure of the nitride precipitates and quantitative analysis of the amount of absorbed nitrogen (i.e. normal and excess nitrogen) upon nitriding of Fe-Ti-Cr alloys. Different Ti/Cr atomic ratios were employed (Ti/Cr = 0.45, 0.87 and 1.90), while keeping the total amount of alloying elements at about 0.30 at.%. Instead of separate precipitations of stable cubic, rock-salt crystal-structure type TiN and CrN nitrides, mixed $Ti_{1-x}Cr_xN$ nitride precipitates developed in the nitrided zone. The precipitates are of platelet morphology (length $\leq$ 30 nm and thickness $\leq$ 3 nm) and of cubic, rock-salt crystal-structure type. The misfit-strain field around the nitride platelets in the ferrite matrix is strongly anisotropic. Further, the misfit strain increases with increasing Ti/Cr atomic ratio. As a consequence, most pronouncedly for the highest Ti/Cr atomic ratio, a tetragonally distorted ferrite matrix surrounds the nitride precipitates. The amount of nitrogen taken up was determined quantitatively by measuring so-called nitrogen-absorption isotherms. It follows that the absorbed amount of so-called excess nitrogen dissolved in the matrix, $[N]_{strain}$ and adsorbed at the nitride-platelet faces, $[N]_{interface}$ increases distinctly with increasing Ti/Cr atomic ratio. The former is due to the increase of tensile hydrostatic component induced by image-misfit stress with increasing Ti/Cr atomic ratio. The latter is the consequence of enlarged interfacial area (thinner platelets and a higher nucleus density with increasing Ti/Cr atomic ratio) and the higher chemical affinity of Ti for N than of Cr for N.

In Chapter 3 the formation of mixed $Cr_{1-x}Al_xN$ nitride, as exhibited by its morphology and uptake of nitrogen as function of Cr/Al atomic ratio is discussed for alloys having a total amount of alloying element equal to 1.5 at.%. Upon nitriding of Fe-Cr-Al alloys, metastable, mixed $Cr_{1-x}Al_xN$ nitrides of cubic, rock-salt crystal-structure type precipitate in the ferrite matrix; the system thus avoids the difficult nucleation of stable AlN (hexagonal, wurtzite structure type) precipitates in the ferrite matrix. The ease of mixed nitride nucleation and thus the nucleation density increases with increasing Cr/Al atomic ratio. Such an effect does not occur for nitrided Fe-Cr-Ti alloys (see above) as both equilibrium nitrides, CrN and TiN, have the same (rock-salt type) crystal structure as the corresponding metastable mixed $Cr_{1-x}Ti_xN$ precipitate. The amount of excess nitrogen taken up by the specimen increases with decreasing Cr/Al atomic ratio. The degree of coherency at the $Cr_{1-x}Al_xN$-platelet faces increases with increasing Cr/Al atomic ratio, which reflects the decrease of the absolute value of the linear misfit parameter parallel to the interface, $\left|\delta_{//}\right|$, with increasing Cr/Al atomic ratio (for the alloys investigated within the range 0.21-2.00), opposite to the trend for the overall misfit parameter.

The amount of excess nitrogen dissolved in the ferrite matrix, $[N]_{strain}$, increases with increasing Cr/Me_2 atomic ratio for Me_2 = Al and decreases with increasing Cr/Me_2 atomic ratio for Me_2 = Ti. The antagonistic behaviour can be understood as consequences of the overall misfit (i.e. volumetric misfit) between nitride platelet and ferrite matrix that increases with increasing Cr/Al atomic ratio and thus decreases with increasing Cr/Ti atomic ratio.

Chapter 4 focuses on the development and application of a numerical model for the kinetics of nitriding of Fe-2at.%Cr-2at.%Ti as exhibited by the evolution of the nitrogen-concentration depth profile as function of nitriding temperature and nitriding

potential. The numerical model has as important (fit) parameters: the surface nitrogen content, the solubility product(s) of the alloying elements and dissolved nitrogen in the ferrite matrix, and a parameter defining the composition of the inner nitride precipitate. These parameters are determined by fitting thus calculated nitrogen-depth profiles to experimental data obtained by EPMA measurements. The results obtained demonstrate that mixed nitrides precipitate, as confirmed by TEM investigation, and exhibit the role of excess nitrogen: The mobile excess nitrogen has a pronounced influence on the increase of the diffusion-zone depth, whereas the immobile excess nitrogen influences the content (i.e. height) of nitrogen of the nitrided zone.

References

[1] S. Lampman, Introduction to surface hardening of steel. ASM Handbook: Heat Treating. Metals Park, Ohio, ASM International. 4 (1991) 259.

[2] E.J. Mittemeijer and S.T. Slycke, Surf. Eng. 12 (1996) 152.

[3] E.J. Mittemeijer and M.A.J. Somers, Surf. Eng. 13 (1997) 483.

[4] H.A. Wriedt, N.A. Gokcen and R.H. Nafziger, Bull. Alloy Phase Diagrams 8 (1987) 355.

[5] E. Lehrer, Z. Elektrochem. 36 (1930) 383.

[6] R. Hoffmann, E.J. Mittemeijer and M.A.J. Somers, HTM 51 (1996) 162.

[7] D.H. Kirkwood, O.E. Atasoy and S.R. Keown, Metals. Sci. 8 (1974) 49.

[8] H.H. Podgurski and F.N. Davis, Acta Metall. 29(1981) 1.

[9] D.S. Rickerby, S. Henderson, A. Hendry and K.H. Jack, Acta Metall. 34 (1986) 1687.

[10] D.H. Jack, Acta Metall. 24 (1976) 137.

[11] W.D. Welch and S.H. Carpenter, Acta Metall. 21 (1973) 1169.

[12] A.D. Krawitz, Scripta Metall. 11 (1977) 117.

[13] S.S. Hosmani, R.E. Schacherl and E.J. Mittemeijer, Acta Mater. 53 (2005) 2069.

[14] S.S. Hosmani, R.E. Schacherl and E.J. Mittemeijer, Acta Mater. 54 (2006) 2783.

[15] M. Pope, P. Grieveson and K.H. Jack, Scan. J. Metall. 2 (1973) 29.

[16] M.M. Yang and A.D. Krawitz, Metall. Trans. 15A (1984) 1545.

[17] N. E. Vives Diaz, S. S. Hosmani, R. E. Schacherl and E. J. Mittemeijer, Acta Mater. 56 (2008) 4137.

[18] P.M. Hekker, H.C.F. Rozendaal and E.J. Mittemeijer, J. Mater. Sci. 20 (1985) 718.

[19] R.E. Schacherl, P.C.J. Graat and E.J. Mittemeijer, Z. Metallkd. 93(2002) 468.

[20] R.E. Schacherl, P.C.J. Graat and E.J. Mittemeijer, Metall. Mater. Trans. 35A (2004) 3387.

[21] B. Mortimer, P. Grieveson and K.H. Jack, Scand. J. Metals. 1 (1972) 203.

[22] S.S. Hosmani, R.E. Schacherl and E.J. Mittemeijer, Mater. Sci. Technol. 21 (2005) 113.

[23] S.S. Hosmani, R.E. Schacherl and E.J. Mittemeijer, J. Mater. Sci. 43 (2008) 2618.

[24] S.S. Hosmani, R.E. Schacherl, L.L. Dobrzyńska and E.J. Mittemeijer, Phil. Mag. 88 (2008) 2411.

[25] H.H. Podgurski, R.A. Oriani, F.N. Davis with Appendix by J.C.M. Li and Y.T. Chou, Trans. Metall. Soc. AIME: 245 (1969) 1603.

[26] H.H. Podgurski and H.E. Knechtel, Trans. Metall. Soc. AIME: 245 (1969) 1595.

[27] M.H. Biglari, C.M. Brakman, M.A.J. Somers, W.G. Sloof and E.J. Mittemeijer, Z. Metallkd. 84 (1993) 2.

[28] M.H. Biglari, C.M. Brakman, M.A.J. Somers, W.G. Sloof, E.J. Mittemeijer and S. Van Der Zwaag, Z. Metallkd. 84 (1993) 124.

[29] M.H. Biglari, C.M. Brakman, E.J. Mittemeijer and S. Van Der Zwaag, Phil. Mag. A 72 (1995) 1281.

[30] M.H. Biglari, C.M. Brakman, E.J. Mittemeijer and S. Van Der Zwaag, Phil. Mag. A 72 (1995) 931.

[31] S. Meka, S.S. Hosmani, A.R. Clauss and E.J. Mittemeijer, Int. J. Mater. Res. 99 (2008) 808.

[32] S. Meka, R.E. Schacherl, E. Bischoff and E.J. Mittemeijer, Adv. Mat. Res. 89-91 (2010) 371.

[33] S.S. Brenner and S.R. Goodman, Scripta Metall. 5 (1971) 865.

[34] J.H. Driver, D.C. Unthank and K.H. Jack, Phil. Mag. 26 (1972) 1227.

[35] J.H. Driver and J.M. Papazian, Acta Metall. 21 (1973) 1139.

[36] R. Wagner and S.S. Brenner, Acta Metall. 26 (1978) 197.

[37] E.C. Bain, Trans. AIME 70 (1924) 25.

[38] M.A.J. Somers, R.M. Lankreijer and E.J. Mittemeijer, Phil. Mag. A 59 (1989) 353.

[39] H.A. Wriedt and L.S. Darken, Trans. TMS–AIME 233 (1965) 111.

[40] E.J. Mittemeijer, P. Van Mourik and Th. D. De Keijser, Phil. Mag. A 43 (1981) 1157.

[41] E.J. Mittemeijer and A. Van Gent, Scripta Metall. 18 (1984) 825.

[42] J. Crank, The Mathematics of Diffusion, Clarendon Press, Oxford (1970).

[43] K. Bongartz, D.F. Lupton and H. Schuster, Metall. Trans. 11A (1980) 1883.

[44] K. Bongartz, W.J. Quadakkers, R. Schulten and H. Nickel, Meall. Trans. 20A (1989) 1021.

[45] Y. Sun and T. Bell, Mater. Sci. Eng., 224A (1997) 36.

[46] S.S. Hosmani, R.E. Schacherl and E.J. Mittemeijer, Metall. Mater. Trans., 38A (2007) 7.

Chapter 2

Nitride formation and excess nitrogen uptake upon nitriding ferritic Fe-Ti-Cr alloys

K. S. Jung, S. Meka, R. E. Schacherl, E. Bischoff and E. J. Mittemeijer

Abstract

The microstructure of the nitrided zone of Fe-Ti-Cr alloys, containing a total of 0.30 at.% (Ti + Cr) alloying elements, with varying Ti/Cr atomic ratio (0.45, 0.87 and 1.90), was investigated by X-ray diffraction (XRD) and transmission electron microscopy (TEM). The stable TiN and CrN nitrides did not precipitate upon nitriding. Instead, ultrafine, metastable, mixed $Ti_{1-x}Cr_xN$ nitride precipitates developed in the nitrided zone: the precipitates were of platelet morphology (length $\leq$ 30 nm and thickness $\leq$ 3 nm) and of cubic, rock-salt crystal-structure type. The misfit strain around the nitride platelets in the ferrite matrix increases with increasing Ti/Cr atomic ratio. As a consequence, most pronouncedly for the highest Ti/Cr atomic ratio, a tetragonally distorted ferrite matrix surrounds the precipitates, as evidenced both by XRD and TEM. The amount of nitrogen taken up was determined quantitatively by measuring so-called nitrogen-absorption isotherms. It follows that the absorbed amount of so-called excess nitrogen dissolved in the matrix and adsorbed at the nitride-platelet faces increases distinctly with increasing Ti/Cr atomic ratio. The results were discussed in terms of the dependence of misfit strain on the Ti/Cr atomic ratio and the higher chemical affinity of Ti for N than of Cr for N.

2.1 Introduction

Nitriding is a widely-used thermochemical surface treatment for, in particular, ferritic steels [1]. The improvement of mechanical properties by means of the formation of inner nitrides plays for this method a crucial role. Due to the possibility of precise control of the nitriding atmosphere, i.e. the chemical potential of nitrogen can be tuned [2], gaseous nitriding of metallic alloys, by applying a NH_3/H_2 gas mixture at atmospheric pressure, is often applied to introduce nitrogen in the ferrite matrix at the surface of a specimen. Note that the application of specific NH_3/H_2 gas mixtures allows the adjustment of the chemical potential of nitrogen corresponding hypothetically to thousands of atmospheres of pure N_2 gas [3].

During *internal* nitriding of iron-based alloy (i.e. the nitriding potential is that low that no iron nitride develops at the surface) containing alloying elements (Me) with a strong affinity for nitrogen, as Cr, Al, V and Ti, fine alloying element nitride precipitates can develop in the nitrided zone adjacent to the surface (called "diffusion zone"), which leads to a pronounced increase of the hardness of the nitrided component. The increase of hardness and related (mechanical) properties strongly depends on the amount of alloying elements, the chemical composition of the nitride precipitates, degree of coherency of the nitride precipitates with the matrix and the precipitate size and morphology [4, 5].

Until now, most studies concerning internal nitriding have focused on binary Fe-Me alloy systems, i.e. Fe-Cr, Fe-Al, Fe-V and Fe-Ti [6-23]. However, commercial nitriding steels often contain more than one alloying element with affinity for nitrogen. Only a few investigations were performed until now on ternary Fe-Me$_1$-Me$_2$ alloy systems. Recently, Ti-based ternary nitrides such as (Ti,Al)N, (Ti,Zr)N and (Ti,Cr)N have gained much attention as second phases particles in steels due to their contribution

to the enhanced performance for cutting tools and machinery components, e.g. regarding wear/corrosion protection [24-28].

In the present work, Ti and Cr were selected as alloying elements, because both Cr and Ti, as separate alloying elements, can form nitrides which are cubic (rock-salt crystal structure), albeit of different lattice constants (a_{CrN} = 4.13Å and a_{TiN} = 4.23Å). Cr and Ti have different chemical affinity for nitrogen (Ti has an affinity for N much larger than that of Cr for N). Both TiN and CrN exhibit a Bain orientation relationship ($\{001\}_{bcc, Fe}$ // $\{001\}_{fcc, MeN}$, $<100>_{bcc, Fe}$ // $<110>_{fcc, MeN}$) for the nitride precipitates with the ferrite matrix [22, 23, 29-31].

The current project involves investigation of the nitriding behaviour of ternary Fe-Ti-Cr alloys. Different Ti/Cr atomic ratios have been employed (Ti/Cr = 0.45, 0.87 and 1.90), while keeping the total amount of alloying element at about 0.30 at.%. The microstructure of the precipitates in the nitrided zone has been investigated by means of X-ray diffraction (XRD) and transmission electron microscopy (TEM). Furthermore, the amount of absorbed nitrogen during nitriding was investigated quantitatively by the analysis of nitrogen-absorption isotherms.

2.2 Experimental

2.2.1 Specimen preparation

Ingots of Fe-Ti-Cr alloys, containing about 0.30 at.% (Ti + Cr) with varying Ti/Cr atomic ratio (0.45, 0.87 and 1.90) were prepared from pure Fe (99.98 wt.%), pure Ti (99.999 wt.%) and pure Cr (99.999 wt.%) using a light-arc furnace. The molten alloys were cast as buttons, with a shape given by a diameter of 40 mm and a height of 15 mm. The precise composition of the Fe-Ti-Cr alloys was analyzed, applying (i) inductive coupled plasma-optic emission spectroscopy (ICP-OES) to determine the

content of the alloying elements Ti and Cr, (ii) a combustion method to determine the

light elements C and S and (iii) a hot-extraction to determine the light elements O and

N. The composition of the alloys is shown in Table 2.1.

The cast buttons were cold-rolled to foils with a thickness of about 0.2 mm. In

order to reduce the rolling induced texture of the specimen, specimens of the as cast

buttons were rolled in different directions. The foils thus obtained were cut into

rectangular specimens (15×15 mm^2) and subsequently ground and polished. The

polished specimens were encapsulated in a quartz tube filled with Ar and annealed at

1073K for 2h to establish a recrystallized grain structure (grain size of about 30 μm).

Before nitriding the specimens were ground and polished (last step: 1 μm diamond

paste) and cleaned ultrasonically with ethanol.

Table 2.1: Composition of the cast alloys, as determined by chemical analysis: Cr and
Ti contents were determined by inductive coupled plasma-optic emission spectroscopy
(ICP-OES) and the light element impurity contents were determined by a combustion
method for C and S, and by hot extraction for O and N.

element / alloy	Cr	Ti	Ti/Cr	N	O	S	C
	(at. pct)			(μg/g)			
Fe-0.10at.%Cr-0.19at.%Ti	0.10 (±0.01)	0.19 (± 0.02)	1.90	< 10	13 ± 5	< 10	9 ± 2
Fe-0.15at.%Cr-0.13at.%Ti	0.15 (±0.02)	0.13 (±0.01)	0.87	< 10	15 ± 5	19 ± 5	7 ± 2
Fe-0.20at.%Cr-0.09at.%Ti	0.20 (±0.02)	0.09 (±0.01)	0.45	< 10	21 ± 5	22 ± 5	6 ± 2

2.2.2 Nitriding

For nitriding the specimen were suspended at a quartz fiber and placed in the middle of

a vertical tube furnace. The gaseous nitriding experiments were performed in a flux of

ammonia/hydrogen gas mixture (NH$_3$: >99.998 vol.% and H$_2$: 99.999 vol.%). The

fluxes of both gases were precisely adjusted with mass flow controllers. The gas flow rate was kept at 500 ml/min, which, because the inner diameter of the tube furnace is 28 mm, corresponds to a linear gas velocity of 1.35 cm/s in the furnace, which is sufficient to avoid any significant (thermal) decomposition of ammonia in the nitriding atmosphere [3].

To maintain a homogeneous precipitation morphology over the entire specimen thickness, during the determination of the absorption isotherms, pre- and denitriding steps were performed prior to the nitrogen-absorption isotherm measurements. The prenitriding step involved nitriding at 853K for 48h with a nitriding potential (cf. Ref. 3) of $r_N = 0.104$ atm$^{-1/2}$. After completion of this prenitriding the specimen was quenched into water at room temperature. Subsequently, the specimen was denitrided in a pure H_2 atmosphere at 743K for 72h.

Nitrogen-absorption isotherms were determined at a temperature of 833K for nitriding potentials r_N in the range from 0.054 atm$^{-1/2}$ to 0.140 atm$^{-1/2}$ (the specimen was nitrided at each nitriding potential for 48h; for details, see Table 2.2). The prenitriding treatment was performed at a nitriding temperature 20K higher than the temperature applied to record the nitrogen-absorption isotherms. The prenitriding at an elevated temperature assures that the precipitation morphology of the specimens does not change during the determination of the nitrogen-absorption isotherms. All applied nitriding treatments in the present work were performed in the α-region of the Lehrer diagram [32, 33] thus ensuring that no iron nitride formation at the specimen surface occurred.

Table 2.2: Applied nitriding parameters for the prenitriding, denitriding and nitriding experiments for determination of the nitrogen-absorption isotherms of the Fe-Ti-Cr alloys.

	Temp. (K)	Time (h)	NH_3 (ml/min)	H_2 (ml/min)	r_N (atm$^{-1/2}$)
pre-nitriding	853	48	45	455	0.104
de-nitriding	743	72	.	500	.
absorption isotherms	833	48	58 50 40 25	442 450 460 475	0.140 0.117 0.091 0.054

The amount of nitrogen uptake and/or loss was determined by weight measurements after and before nitriding or denitriding using a Mettler microbalance with an accuracy of 0.1 µg. In order to obtain an accurate weight value, the average value of ten weight measurements was taken.

2.2.3 X-ray diffraction

X-ray diffraction (XRD) analysis of the specimens before and after nitriding was performed employing a Philips X'Pert diffractometer in Bragg-Brentano geometry using Co-K$_\alpha$ (λ=1.7889Å) radiation and a graphite monochromator in the diffracted beam. The measurements were performed in the diffraction-angle, 2θ, range of 40° - 130° with a step size of 0.05°. The contribution of the Co-Kα_2 radiation of the recorded diffractograms, was removed according to Ref. 34. The thus corrected diffractograms were evaluated by fitting a Pearson VII profile-shape function, using TOPAS software, for the diffraction-line profiles in the diffractograms.

2.2.4 Microhardness measurement

Microhardness values before and after nitriding were obtained by carrying out hardness measurements across the cross-section of specimens employing a Vickers microhardness tester (Leica VMHT Mot). A load of 100 mN, an indenter speed of 30 µm/s and a holding time of 12 sec for each indentation were applied. The distances between the indentations and the length of both indentation-diagonals were measured with a calibrated light optical microscope (Zeiss Axiophot microscope equipped with Olympus ColorView IIIu digital camera) using analySIS Imaging software. The microhardness values reported in this paper are the average of five measurements made at the same depths of the specimen cross-section.

2.2.5 Transmission electron microscopy

Samples for transmission electron microscopy (TEM) were prepared from the middle of the nitrided zone as follows.

Discs ($\Phi = 3$ mm) were stamped with a mechanical punch from sheets produced by removing material mechanically from both sides (faces) of a nitrided specimen. These discs were thinned, to obtain an electron-transparent area, applying the jet-electropolishing technique employing a Struers Tenupol-3 apparatus (bath composition: 85 vol.% acetic acid and 15 vol.% perchloric acid, current: 24 mA $\leq I \leq$ 42 mA, voltage: 19.5V, temperature: 278K, flow rate setting: "20", and treatment time: 174 sec $\leq t \leq$ 242 sec) and subsequently rinsed in ethanol, acetone and isopropanol. To generate a hole in the middle of the sample, the discs were fixed during the jet-electropolishing treatment between two platinum rings.

TEM analysis was performed using a Philips CM 200 transmission electron microscope operated at 200 kV. Bright field (BF) images and selected area diffraction patterns (SADPs) were taken by a Gatan CCD camera.

2.2.6 Electron probe microanalysis (EPMA)

To determine the (depth) distribution of the alloying elements and nitrogen after nitriding of the specimens, electron probe microanalysis (EPMA) was performed on specimen cross sections employing a Cameca SX100 instrument. Pieces of the specimen were cut to prepare cross-sections by subsequently embedding of these pieces with a Polyfast (Struers, a conductive bakelite resin with carbon filler embedding material), followed by grinding and polishing (last step: 1 μm diamond paste). A focused electron beam at an accelerating voltage of 15 kV and a current of 100 nA was applied. To obtain the element contents in the specimens, the intensities of the characteristic Ti-K_α, Cr-K_α, Fe-K_β and N-K_α X-ray emission peaks were determined at points separated at distances of 2 μm along lines perpendicular to the surface of the specimen in the specimen cross section. The concentrations of Ti, Cr and Fe were determined on the basis of the ratio of the corresponding characteristic X-ray emission peak intensity of the specimen and that of a standard specimen (i.e. pure Ti, pure Cr and pure Fe) by applying the $\Phi(\rho z)$-correction [35].

For the determination of the characteristic X-ray emission peak of nitrogen a correction procedure had to be applied, because of severe overlap of the N-K_α and Ti-L_l X-ray emission peaks. The correction procedure, known as *ratio method*, is as follows [36]:

(i) EMPA analysis of the nitrided Fe-Ti-Cr alloy specimen ("SPE"), provides the intensity $I_{Ti\text{-}K\alpha}{}^{SPE}$ and the total intensity at the 2θ position of the N-K$_\alpha$ emission peak, $I_{tot(N)}{}^{SPE}$, which intensity consists of both $I_{N\text{-}K\alpha}{}^{SPE}$ and a contribution $I_{Ti\text{-}L1(N)}{}^{SPE}$ at the 2θ position of N-K$_\alpha$.

(ii) The 2θ position and standard intensity of the N-K$_\alpha$ X-ray emission peak are obtained using Fe$_4$N as a standard material.

(iii) Intensities of the Ti-K$_\alpha$ emission peak ($I_{Ti\text{-}K\alpha}{}^{STD}$ at its own specific 2θ value) and of the Ti-L$_l$ emission peak at the 2θ position of the N-K$_\alpha$ peak position ($I_{Ti\text{-}L1(N)}{}^{STD}$) are obtained using a pure Ti standard specimen ("STD").

(iv) Assuming a constant Ti-L$_l$(N) and Ti-K$_\alpha$ intensity ratio in standard ("STD") and nitrided specimen ("SPE"), i.e. ignoring a possible emission peak shift between standard material and the specimen, a correction factor, *CF* can be given as follows;

$$CF = \left(\frac{I_{Ti-L_1(N)}{}^{STD}}{I_{Ti-K_\alpha}{}^{STD}} \right) = \left(\frac{I_{Ti-L_1(N)}{}^{SPE}}{I_{Ti-K_\alpha}{}^{SPE}} \right) \qquad (2.1)$$

(v) The nitrogen intensity, $I_{N\text{-}K\alpha}{}^{SPE}$, can now be calculated from $I_{tot(N)}{}^{SPE}$ and $I_{Ti\text{-}K\alpha}{}^{SPE}$:

$$\begin{aligned} I_{N-K_\alpha}{}^{SPE} &= I_{tot(N)}{}^{SPE} - I_{Ti-L_1(N)}{}^{SPE} \\ &= I_{tot(N)}{}^{SPE} - CF \times I_{Ti-K_\alpha}{}^{SPE} \end{aligned} \qquad (2.2)$$

Finally, the concentration of nitrogen is obtained from the ratio of the thus obtained N-K$_\alpha$ intensity of the specimen and that of the standard material (γ'-Fe$_4$N), applying the Φ(ρz) approach (see above).

2.3 Results and evaluation

2.3.1 The nitrided microstructure

X-ray diffractograms were taken from the specimen surface before and after nitriding for all Fe-Ti-Cr alloys (Ti/Cr atomic ratio = 0.45, 0.87 and 1.90). Only ferrite reflections appear in the diffractograms. For all alloys, the diffraction peaks of the ferrite, particularly the $200_{\alpha\text{-Fe}}$ reflection, had strongly broadened after nitriding (Figs. 2.1a-c).
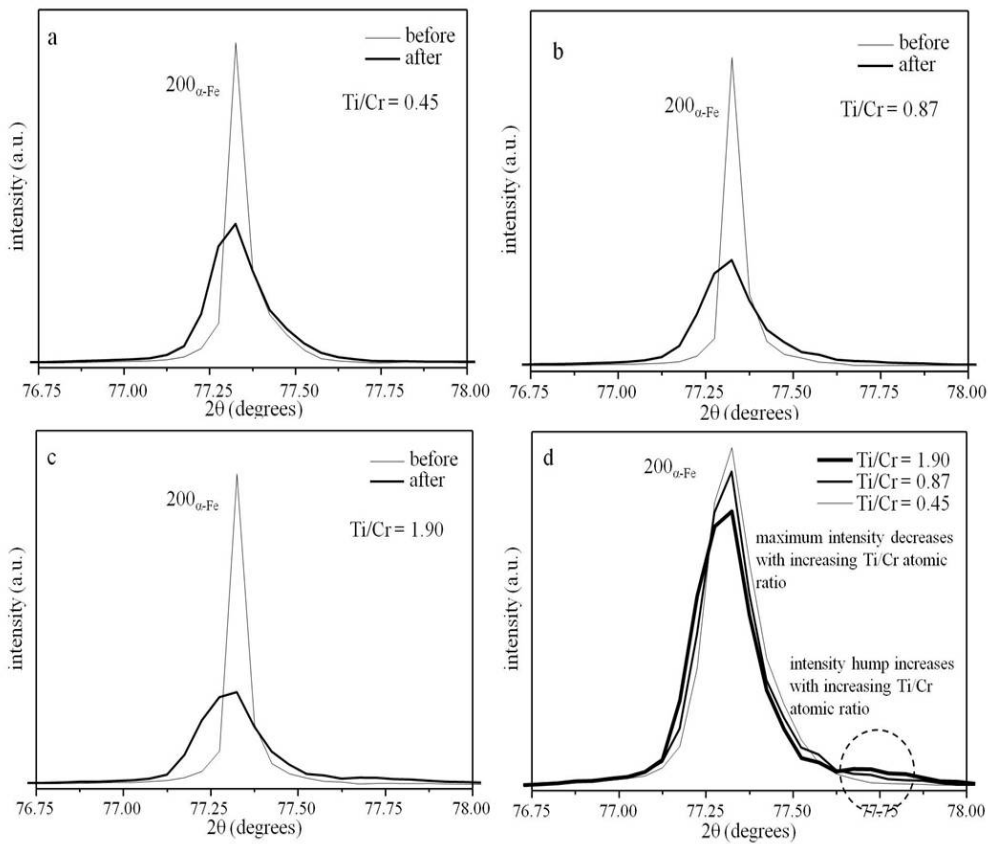
Fig. 2.1: X-ray diffractograms of the $200_{\alpha\text{-Fe}}$ reflection ($76.5° < 2\theta < 78.5°$, Co-K$_\alpha$ radiation, step size 0.05°; normalized with respect to the integral intensity) before and after nitriding of the Fe-Ti-Cr alloy concerned; (a) Ti/Cr = 0.45, (b) Ti/Cr = 0.87, (c) Ti/Cr = 1.90; (d) composite of all $200_{\alpha\text{-Fe}}$ reflections (a - c) after nitriding. The nitriding experiments were performed at 853K for 48h with nitriding potential $r_N = 0.104$ atm$^{-1/2}$.

The occurrence of pronounced diffraction-line broadening of the ferrite reflexes upon nitriding without the appearance of separate alloying element nitride reflections, can be

ascribed to the development of microstrain due to the formation of (largely) coherent precipitates in the ferrite matrix which diffract coherently with the matrix, as discussed in Ref. 37. In addition to the observed broadening of the $200_{\alpha\text{-Fe}}$ diffraction line, an intensity hump arises at the high-angle side of the $200_{\alpha\text{-Fe}}$ reflection. It becomes more pronounced with increasing the Ti/Cr atomic ratio of the specimen (see, especially, the dashed circle in Fig. 2.1d).

TEM bright field (BF) and corresponding selected area diffraction patterns (SADPs) of nitrided Fe-Ti-Cr alloys with Ti/Cr = 0.45 and 1.90 are shown in Figs.2.2a and b, respectively.
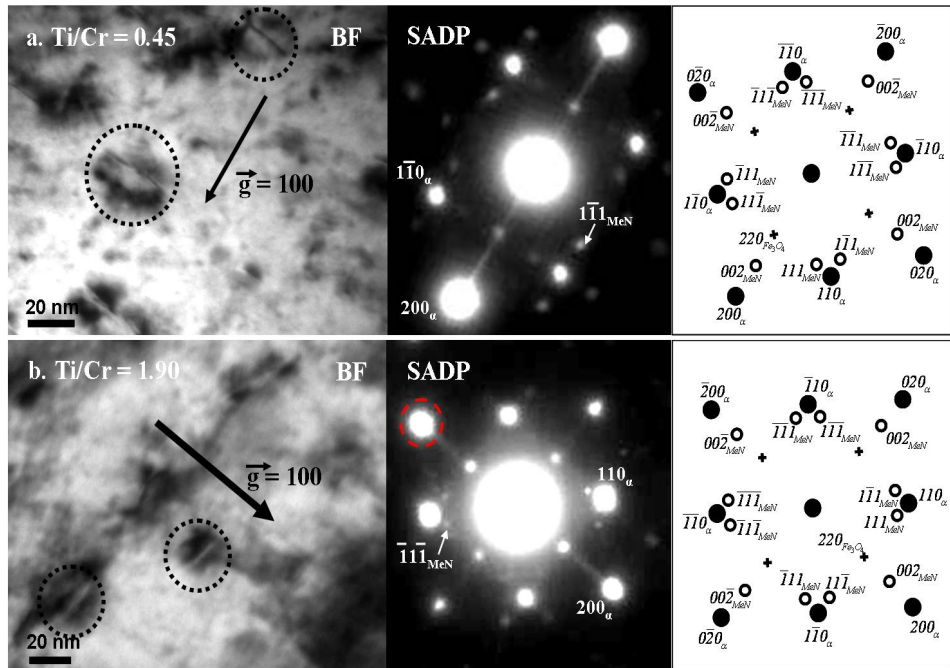
Fig. 2.2: TEM BF images (left) showing diffraction contrast due to fine (misfitting) $Ti_{1-x}Cr_xN$ nitride platelets in the ferrite matrix. (a) Ti/Cr = 0.45 and (b) Ti/Cr = 1.90. The dotted open circles in the BF images indicate locations where fine nitride platelets had developed, giving rise to misfit-strain field induced "coffee-bean" contrast. The SADPs (middle) were taken at electron-beam directions close to $[001]_{\alpha\text{-Fe}}$. The SADP of the Fe-Ti-Cr, Ti/Cr = 1.90 alloy in (b) shows elongated $200_{\alpha\text{-Fe}}$ diffraction spots (see dashed circle), which is composed of a cubic ferrite 200 diffraction spot and a 200 diffraction spot originating from tetragonally strained ferrite (see text). Schematic diffraction patterns (right), corresponding with the SADPs shown, for the concerned electron-beam, i.e. $[001]_{\alpha\text{-Fe}}$ direction and nitride precipitates complying with a Bain orientation relationship with the α-Fe matrix (black dots: diffraction spots of the ferrite matrix; unfilled circles: diffraction spots of the nitride precipitates).

The electron-beam direction in both SADPs is close to (i.e. does not coincide exactly with) the [001] zone axis of the ferrite, in order to avoid strong diffraction by the matrix and to reveal the presence of the precipitates by their diffraction contrast. The TEM BF show an ultra-thin platelet morphology of the nitride precipitates in the ferrite matrix (see the dotted circles in the BF images, which indicate regions showing the typical coffee-bean contrast due to the misfit-strain between the thin nitride platelets and the ferrite matrix for platelets parallel to the $[001]_{\alpha\text{-Fe}}$ electron beam/zone axis; the nitride platelets in the dotted circles are parallel to $(100)_{\alpha\text{-Fe}}$ matrix lattice planes (see below)). The size of the platelets (length $\leq$ 30 nm and thickness $\leq$ 3 nm) does not depend significantly on the Ti/Cr atomic ratio.

The SADPs show pronounced streaks through the $200_{\alpha\text{-Fe}}$ diffraction spots in the $<100>_{\alpha\text{-Fe}}$ directions and additional diffraction spots near the $110_{\alpha\text{-Fe}}$ diffraction spots corresponding with a lattice spacing, d, which is compatible with the spacing of the {111} lattice planes of a cubic, rock-salt structure-type nitride (MeN). Moreover, particularly for the highest Ti/Cr ratio (see SADP in Fig. 2.2b), the $200_{\alpha\text{-Fe}}$ diffraction spots have split into two; one corresponding to cubic ferrite (d_{200} of cubic ferrite from SADP = 1.43Å) and another one corresponding to tetragonally distorted ferrite.

The intensity hump observed in the X-ray diffractograms at the high-angle side of the $200_{\alpha\text{-Fe}}$ reflection (see dashed circle in Fig. 2.1d) is compatible with the occurrence of a split $200_{\alpha\text{-Fe}}$ spot in the SADP shown in Fig. 2.2b. As demonstrated here by fitting (using a Pearson VII profile-shape function) to the overall $200_{\alpha\text{-Fe}}$ reflection shown in Fig. 2.1c, the overall reflection is composed of two peaks (see Fig. 2.3 for the nitrided Fe-Ti-Cr alloy with Ti/Cr = 1.90): one is ascribed to a cubic ferrite 200 reflection (d_{200} of cubic ferrite = 1.43Å) and the other one is ascribed to the 200/002 doublet reflection of tetragonally distorted ferrite (d_{200} of tetragonal ferrite = 1.43Å, d_{002} of tetragonal ferrite = 1.42Å). The

fit of the tetragonal doublet and cubic reflections to the measured intensity data, as shown

in Fig. 2.3, was performed adopting the procedure described in Ref. 37 (Note that in Ref.

37 the c and a lattice parameters of the bct phase have been, unconventionally, defined

such that c = b instead of a = b). These d-spacings, derived from the XRD pattern, are well

compatible with the split $200_{\alpha\text{-Fe}}$ diffraction spot in the SADP shown in Fig. 2.2b.
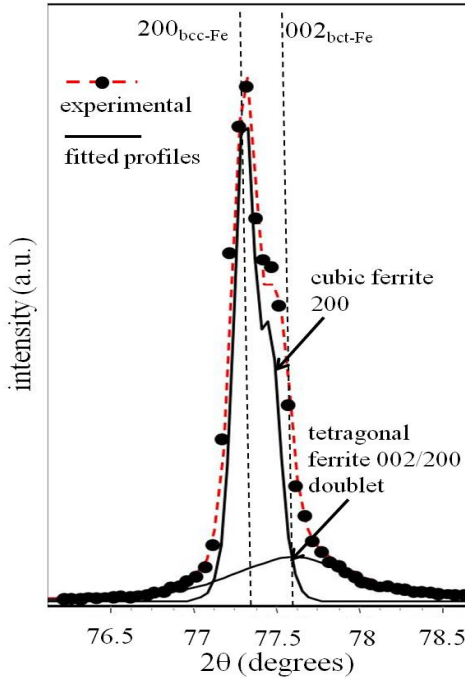
Fig. 2.3: Contributions of the 200 reflection of the (cubic, bcc) ferrite and the 200/002 doublet reflection of the tetragonally distorted (bct) ferrite to the total observed diffraction profile as evaluated by fitting a Pearson VII profile-shape function for the various reflection contributions (Ti/Cr = 1.90).

The positions in the SADPs of the 111_{MeN} diffraction spots, near the $110_{\alpha\text{-Fe}}$

diffraction spots and ascribed to the face centred cubic, rock-salt type MeN structure, are

compatible with the occurrence of a Bain orientation relationship of cubic, rock-salt

structure type MeN precipitates with the bcc ferrite matrix,: $\{001\}_{\text{bcc}}$ // $\{001\}_{\text{fcc}}$, $<100>_{\text{bcc}}$

// $<110>_{\text{fcc}}$ (cf. Refs. 37 and 38).

The nitride platelets develop with $\{001\}_{\alpha\text{-Fe}}$ lattice planes as habit planes. The mismatch of the nitride platelet with the ferrite matrix is such that, in order to maintain coherency, the ferrite matrix in the immediate surroundings of the nitride platelets is anisotropically, tetragonally deformed: A compressive misfit stress develops in the directions normal to the platelet (i.e. in a $<001>_{\alpha\text{-Fe}}$ direction), whereas a tensile misfit stress develops parallel to the platelet faces (i.e. in $<100/010>_{\alpha\text{-Fe}}$ directions). The surrounding ferrite matrix of the nitride platelet can thus be considered as a bct phase (see Fig. 2.4).
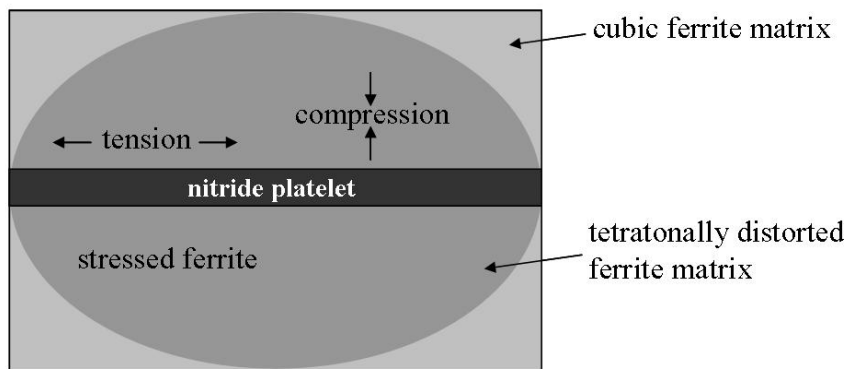
Fig. 2.4: Schematic presentation of a misfitting coherent nitride platelet and the surrounding ferrite matrix, and the associated state of stress in the matrix.

If precipitates of CrN and TiN would have developed separately in the ferrite matrix during nitriding, the diffraction spots of both nitrides should be distinguishable (in the SADPs). However, the SADPs show only singular 111 reflections of a cubic, rock-salt crystal structure type MeN nitride. This suggests that Ti and Cr have precipitated together in a cubic, rock-salt type mixed $Ti_{1-x}Cr_xN$ nitride (such mixed precipitation, leading to a metastable precipitate, $(Me_1,Me_2)N$, in principle prone to decomposition into the two equilibrium precipitates, Me_1N and Me_2N, was observed for the first time upon nitriding Fe-Cr-Al alloys [38]). The d-spacing measured from the 111 reflection of the mixed $Ti_{1-x}Cr_xN$ (Ti/Cr = 0.45) is 2.41Å, which (indeed) is in-between the 111 d-spacing of CrN

(2.38Å) and the 111 d-spacing of TiN (2.44Å). Furthermore, the lattice parameter derived from the 111 reflection of mixed $Ti_{1-x}Cr_xN$ with Ti/Cr = 0.45 (see above), which is 4.17Å, agrees well with that reported for a (Ti, Cr)N (Ti/Cr = 0.45) film produced by reactive cathodic sputtering [39, 40].

The lattice parameters of mixed $Ti_{1-x}Cr_xN$ nitride, as derived from the reflections recorded in the SADPs, are shown as function of the relative Ti content in Fig. 2.5, together with those pertaining to pure CrN and pure TiN. Evidently, the lattice parameter of mixed $Ti_{1-x}Cr_xN$ nitride increases linearly with increasing relative Ti content, indicating that the substitutional solid solution of Ti and Cr in the mixed nitride complies with Vegard's law. This provides further support for the above interpretation implying that mixed $Ti_{1-x}Cr_xN$ nitride forms upon nitriding.
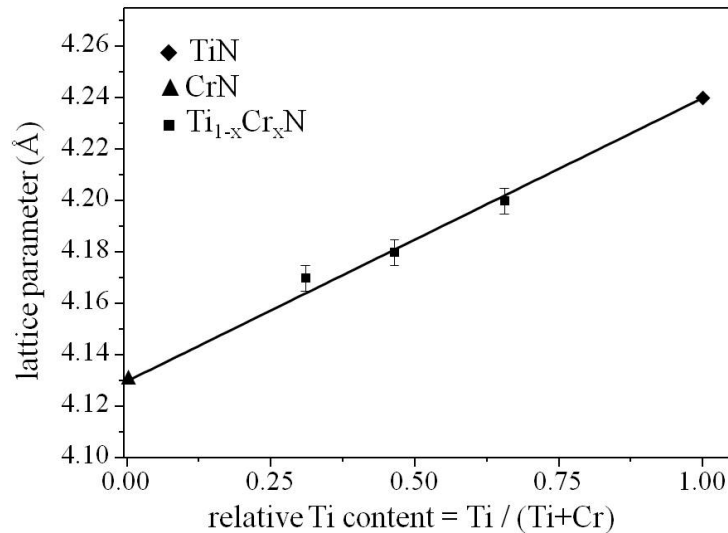
Fig. 2.5: Lattice parameters of pure CrN (open triangle), pure TiN (open diamond) and mixed $Ti_{1-x}Cr_xN$ (open squares) as a function of relative Ti atomic content (relative with respect to the total amount of alloying elements, i.e. Ti + Cr).

2.3.2 Quantitative analysis of excess nitrogen uptake

A nitrogen-absorption isotherm shows the dependence of the amount of nitrogen taken up by a (homogeneously) nitrided specimen as function of the nitriding potential, r_N (directly related to the chemical potential of nitrogen absorbed in the ferrite matrix for a given nitriding atmosphere [2]). The analysis of nitrogen-absorption isotherms allows distinction of various kinds of differently (chemically) bonded nitrogen.

The amount of nitrogen absorbed in the ferrite matrix upon nitriding by means of an NH_3/H_2 gas mixture can be described by the equilibrium:

$$NH_3 \Leftrightarrow [N]_\alpha + \frac{3}{2}H_2 \tag{2.3}$$

where $[N]_\alpha$ is the concentration of nitrogen dissolved interstitially in the ferrite matrix. The solubility of nitrogen in ferrite matrix, $[N]_\alpha$, is proportional to the nitriding potential, r_N ($= \dfrac{p_{NH_3}}{p_{H_2}^{3/2}}$, with p as partial pressure), according to

$$[N]_\alpha = K \cdot r_N \tag{2.4}$$

where K is the equilibrium constant for Eq. (2.3) and where it has been assumed that the activity coefficient of the nitrogen atoms is constant and has been incorporated in K [2].

Any point on a nitrogen-absorption isotherm indicates the equilibrium amount of nitrogen absorbed by the specimen at a given nitriding potential. To determine experimentally nitrogen-absorption isotherms, it is essential to establish a homogeneous, constant nitrogen content throughout the cross-section of the specimen. Further, the precipitation morphology should not change during determination of the absorption isotherm. Therefore the preceding prenitriding treatment (cf. section 2.2.2) is performed at a temperature higher than applied for determination of the absorption

isotherm, to ensure a constant precipitate morphology. It has been verified that such conditions have been realized in the present work (see what follows).

Elemental concentration-depth profiles determined for the entire cross section of the specimens (pre)nitrided at 853K for 48h (EPMA data) are shown in Figs. 2.6a-c for the alloys with Ti/Cr = 0.45, 0.87 and 1.90, respectively. Evidently, after the homogeneous nitriding, the nitrogen uptake is larger than the amount of nitrogen required for the precipitation of all Ti and Cr as mixed $Ti_{1-x}Cr_xN$ nitride, $[N]_{Ti_{1-x}Cr_xN}$, plus the amount of nitrogen necessary to establish the equilibrium solubility in an unstrained ferrite matrix, $[N]_\alpha^0$. This so called amount of "normal" nitrogen, $[N]_{nor} \equiv [N]_{Ti_{1-x}Cr_xN} + [N]_\alpha^0$, has been indicated by the horizontal-dashed line in Figs. 2.6a-c. The difference between the experimentally obtained total amount of nitrogen, $[N]_{tot}$, and the amount of "normal" nitrogen, $[N]_{nor}$, is defined as excess nitrogen, $[N]_{ex}$ (for details see Ref. 18 and 31).

After prenitriding, the specimens were subsequently denitrided in a pure H_2 (500 ml/min) atmosphere at 743K for 72h. After the denitriding step, the nitrogen content which remains in the specimen was determined by weighing. The remaining nitrogen content in the Fe-Ti-Cr alloys amounts to 0.25 ($\pm$0.04), 0.25 ($\pm$0.01) and 0.26 ($\pm$0.01) at.%[*] for the alloys with Ti/Cr = 0.45, 0.87 and 1.90, respectively, which can be fully attributed to nitrogen strongly bonded to Ti and Cr in corresponding nitride precipitates $Ti_{1-x}Cr_xN$. This indicates that all excess nitrogen was removed from the specimens by the denitriding treatment.

---

[*] The error ranges indicated were taken equal to the *maximal* deviation from the average value calculated on the basis of the ten weight measurements before and after (de)nitriding.
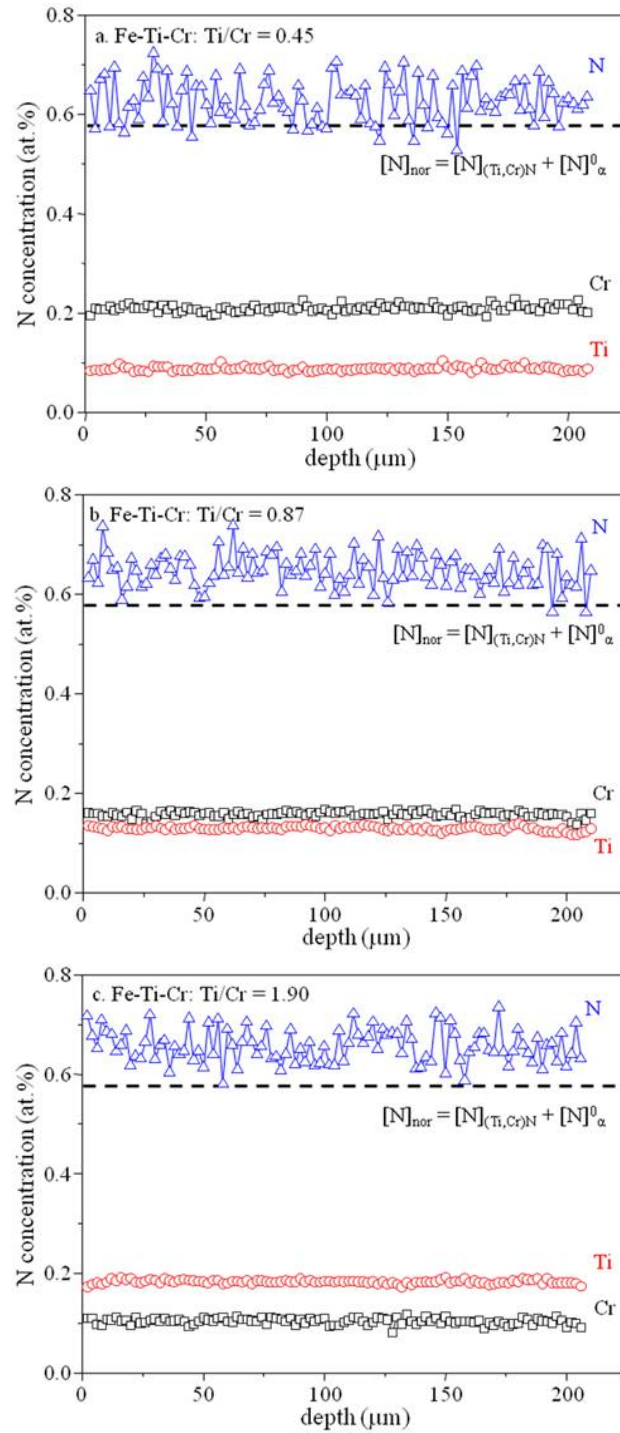
Fig. 2.6: N, Ti and Cr (EPMA) concentration-depth profiles measured for the entire cross sections of nitrided Fe-Ti-Cr specimens (a) Ti/Cr = 0.45, (b) Ti/Cr = 0.87 and (c) Ti/Cr = 1.90 after pre-nitriding (48h at 853K with r_N = 0.104 atm$^{-1/2}$). The dashed horizontal line denotes the amount of "normal" nitrogen: sum of the amounts of nitrogen necessary to transform all alloying elements into alloying element nitrides, $[N]_{Ti_{1-x}Cr_xN}$, and of nitrogen dissolved interstitially in the unstrained ferrite matrix, $[N]_\alpha^0$.

The nitrogen-absorption isotherms for each specimen (after prenitriding and denitriding, as discussed above) are shown in Figs. 2.7a-c for the alloys with Ti/Cr = 0.45, 0.87 and 1.90, respectively. A straight line (dashed line in Figs. 2.7a-c) can well be fitted (least squares analysis) to the data points representing the total amount of absorbed nitrogen. The extrapolation to $r_N = 0$ yields the data point 'A' on the ordinate as shown in Figs. 2.7a-c. The nitrogen level indicated with 'B' on the ordinate in Figs. 2.7a-c represents the amount of nitrogen required for the formation of stoichiometric mixed $Ti_{1-x}Cr_xN$ nitride precipitates (i.e. $[N]_{Ti_{1-x}Cr_xN}$), i.e. the (measured) amount of nitrogen remaining after denitriding (see above).
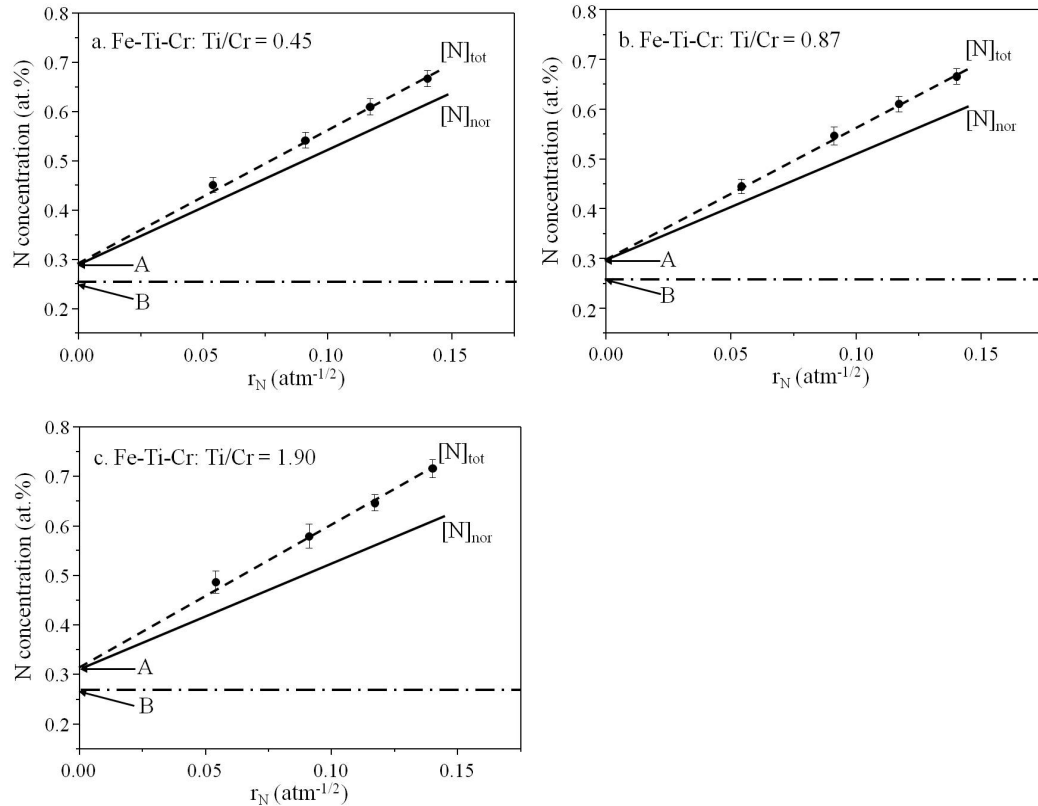
Fig. 2.7: Nitrogen-absorption isotherms after successive prenitriding and denitriding treatments for Fe-Ti-Cr alloys (a) Ti/Cr = 0.45, (b) Ti/Cr = 0.87 and (c) Ti/Cr = 1.90. The linear portions of the nitrogen-absorption isotherms have been indicated by the dashed lines which intersect the ordinates at $r_N = 0$ at nitrogen levels indicated by A. The nitrogen levels after de-nitriding (horizontal dash-dot lines) have been indicated by B.

Hence, in line with the reasoning applied for e.g. Fe-V [19] and Fe-Cr [6] alloys, it is suggested that the difference $A - B$ can be ascribed to (excess) nitrogen adsorbed at the interface between nitride precipitate and ferrite matrix, $[N]_{interface}$. The thus obtained $[N]_{interface}$ values have been gathered, together with the values of levels A and B, in Table 2.3 and Fig. 2.8a.
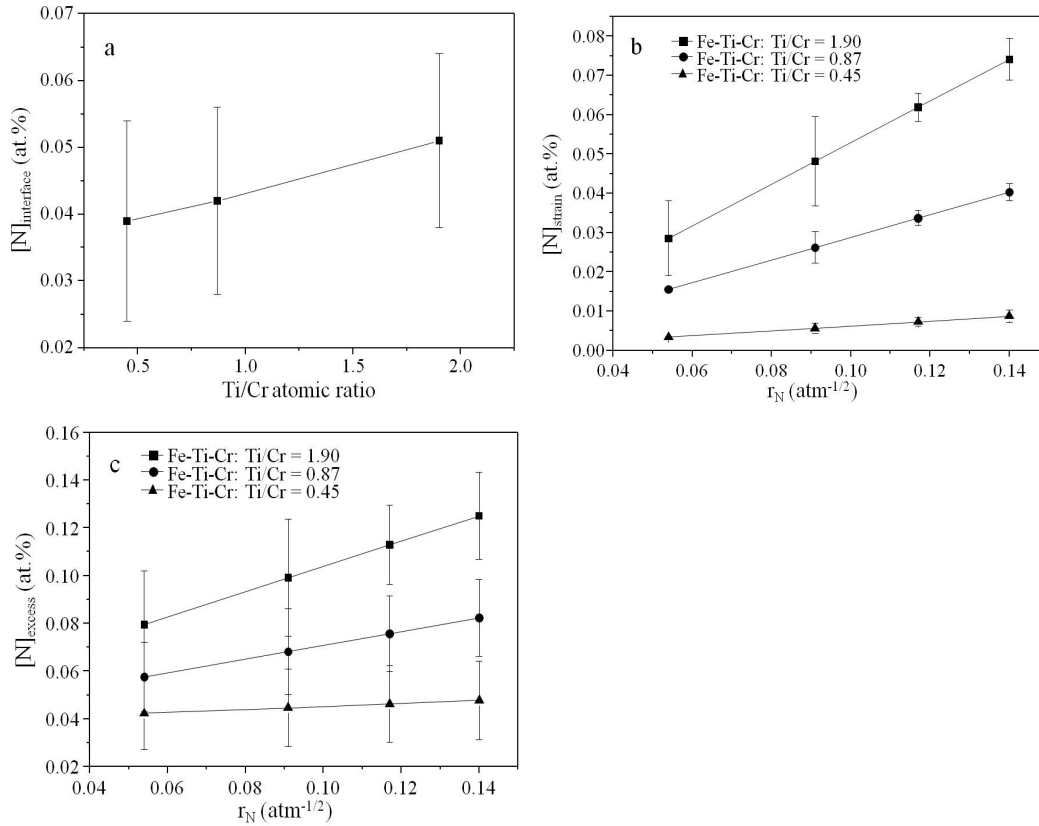
Fig. 2.8: Excess nitrogen (a) adsorbed at the nitride precipitates/ferrite matrix interface, $[N]_{interface}$, as function of Ti/Cr atomic ratio (b) dissolved interstitially in the ferrite matrix due to the presence of a misfit-strain field, $[N]_{strain}$ and (c) total amount of excess nitrogen (= $[N]_{interface} + [N]_{strain}$) for Fe-Ti-Cr alloys (Ti/Cr = 0.45, 0.87 and 1.90) as function of the nitriding potential, r_N.

Table 2.3: The values of nitrogen uptake at level A (interception of the dashed line in Figs. 2.7a-c with the ordinate, i.e. at nitriding potential, $r_N = 0$), at level B (as obtained after denitriding) and the accordingly calculated amount of nitrogen adsorbed at the interface nitride precipitate/ferrite matrix, $[N]_{interface}$ (i.e. $A - B$).

alloy	A (at. pct)	B (at. pct)	$[N]_{interface}$ (at. pct)
Fe-Ti-Cr: Ti/Cr = 0.45	0.290	0.251 (±0.015)	0.039 (±0.015)
Fe-Ti-Cr: Ti/Cr = 0.87	0.296	0.254 (±0.014)	0.042 (±0.014)
Fe-Ti-Cr: Ti/Cr = 1.90	0.311	0.260 (±0.013)	0.051 (±0.013)

The composition of a $Ti_{1-x}Cr_xN$ precipitate together with the interfacial adsorbed excess nitrogen, $[N]_{interface}$, can be described as $Ti_{1-x}Cr_xN_y$, where

$$y = \frac{[N]_{Ti_{1-x}Cr_xN} + [N]_{interface}}{[N]_{Ti_{1-x}Cr_xN}} = \frac{level\ A}{level\ B} \tag{2.5}$$

The value of y thus obtained contains indirect information on the average thickness of the precipitate platelet. As shown above (see section 2.3.1), $Ti_{1-x}Cr_xN$ precipitates develop as platelets of cubic, rock-salt crystal structure type obeying a Bain orientation relationship with the ferrite matrix. With $\{001\}_{Ti_{1-x}Cr_xN}$ as a habit plane, the thickness of a monolayer of $Ti_{1-x}Cr_xN$ is one half of the lattice parameter of the rock-salt crystal structure type (i.e. $\frac{a_{Ti_{1-x}Cr_xN}}{2}$). If at every octahedral interstice in the ferrite matrix *at* the nitride/matrix interface one excess nitrogen atom is trapped, it follows

$$y = \frac{n+2}{n} \tag{2.6}$$

where n is the number of $Ti_{1-x}Cr_xN$ monolayers comprising the platelet. Thus the thickness t of a $Ti_{1-x}Cr_xN$ platelet follows from

$$t = n \cdot \frac{a_{Ti_{1-x}Cr_xN}}{2} = \frac{a_{Ti_{1-x}Cr_xN}}{y-1} \tag{2.7}$$

Using lattice-parameter data of mixed $Ti_{1-x}Cr_xN$ nitride as obtained in this work (see Fig. 2.5) the thus obtained nitride-platelet thickness values have been gathered in Table 2.4 together with the corresponding y values. These deduced thickness values obtained are well compatible with the data obtained by the TEM investigations (see section 2.3.1).

Table 2.4: The value of y in $Ti_{1-x}Cr_xN_y$ and the accordingly deduced (see text) average thickness of the $Ti_{1-x}Cr_xN$ platelets (calculated using Eq. (2.6)) for Fe-Ti-Cr alloys with atomic ratio Ti/Cr = 0.45, 0.87 and 1.90.

alloy	y in $Ti_{1-x}Cr_xN_y$	average thickness of platelets (nm)
Fe-Ti-Cr: Ti/Cr = 0.45	1.16	2.6
Fe-Ti-Cr: Ti/Cr = 0.87	1.18	2.3
Fe-Ti-Cr: Ti/Cr = 1.90	1.20	2.1

As follows from Eq. (2.4), $[N]_\alpha = [N]_{tot} - A$ represents the amount of nitrogen dissolved in the ferrite matrix. The normal amount of dissolved nitrogen, $[N]_\alpha^0$, is represented by $[N]_\alpha^0 = [N]_{nor} - A$; see the full line indicated with $[N]_{nor}$ in Figs. 2.7a-c. The difference between the dashed and full straight lines represents excess nitrogen dissolved in the ferrite matrix. This dissolved excess nitrogen, $[N]_{strain}$, is due to the presence of strain fields around the misfitting nitride precipitates [31]. Positive volumetric misfit is associated with the precipitation of nitride precipitates in the ferrite matrix. Assuming fully elastic accommodation of the misfit, then a finite matrix shows positive lattice dilation. The matrix lattice dilation generated by the misfitting nitrides, induced by the hydrostatic component of the image-stress field of finite bodies, provides a geometrical understanding for the occurrence of an enhanced amount of dissolved nitrogen.

From the slope of the extrapolated straight dashed line, S, the amount of $[N]_{strain}$ can be calculated:

$$S = \frac{\Delta[N]_\alpha}{\Delta r_N} = \frac{\Delta[N]_\alpha^0 + \Delta[N]_{strain}}{\Delta r_N} = S_\alpha^0 + \frac{\Delta[N]_{strain}}{\Delta r_N} \qquad (2.8)$$

The value of S_α^0 at a given nitriding temperature can be taken from the nitriding behavior of pure α-Fe (such data used here have been taken from Ref. 41). Hence from the slope S the value of $[N]_{strain}$ can be given as fraction of r_N: see Fig. 2.8b. It follows that $[N]_{strain}$ increases distinctly with increasing Ti/Cr atomic ratio. This suggests that the level of microstrain in the ferrite matrix increases with increasing Ti/Cr atomic ratio.

This result is compatible with the measured microhardness data: the average microhardness of the specimens before and after nitriding is shown in Fig. 2.9 as a function of the Ti/Cr atomic ratio. The nitriding induced increase of the microhardness increases significantly with increasing Ti/Cr atomic ratio. Also the X-ray diffraction data suggest an increase of microstrain level with increasing Ti/Cr atomic ratio (see the XRD results and their discussion in section 2.3.1).
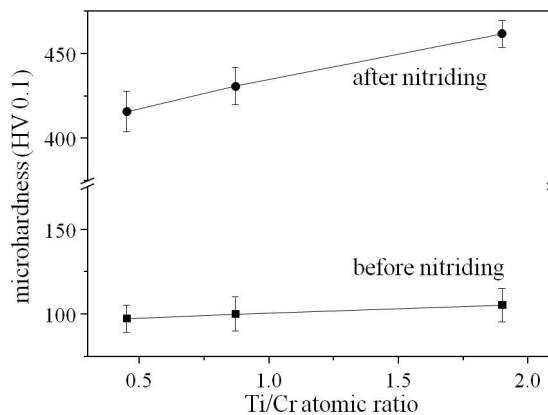

Fig. 2.9: Microhardness of the Fe-Ti-Cr alloys (Ti/Cr = 0.45, 0.87 and 1.90) before and after nitriding as a function of their Ti/Cr atomic ratio. The error ranges indicated were taken equal to the maximal deviation from the average value (10 measurements) for each data point.

The total amount of excess nitrogen is given by the sum of $[N]_{strain}$ (dependent on r_N) and $[N]_{interface}$ (independent of r_N): $[N]_{excess} = [N]_{strain} + [N]_{interface}$. Evidently, as $[N]_{strain}$, $[N]_{interface}$ also increases with increasing Ti/Cr atomic ratio (cf. Fig. 2.8).

2.4 General discussion; the role of the Ti/Cr atomic ratio

During nitriding of ferritic ternary Fe-Ti-Cr alloys cubic, rock-salt type crystal structure, mixed $Ti_{1-x}Cr_xN$ nitride platelets precipitate. The chemical affinity of Ti for N to precipitate as TiN is much larger than that of Cr for N to precipitate as CrN [31]. This suggests a much larger driving force for Ti than for Cr to precipitate as nitride upon nitriding. There is no difficulty for the mixed nitride to form the cubic, rock-salt type crystal structure: both TiN and CrN have this crystal structure. In particularly considering the misfit-strain development upon formation of nitride precipitates in the ferrite matrix, it follows that uptake of Cr in TiN can be favoured because it leads to reduction of the misfit-strain with the surrounding ferrite matrix (see below). On this basis it can be suggested that the Cr atoms are "dragged" into the developing cubic, rock-salt structure type TiN precipitates, thereby forming mixed $Ti_{1-x}Cr_xN$ nitride.

The mixed $Ti_{1-x}Cr_xN$ nitride platelets exhibit a Bain orientation relationship with the ferrite matrix with $\{001\}_{\alpha-Fe}$ habit planes parallel to the platelet faces. The platelet morphology is a consequence of the strongly anisotropic misfit-strain with the surrounding ferrite matrix: the linear misfits of the mixed $Ti_{1-x}Cr_xN$ nitride platelet (Ti/Cr = 0.45) along and perpendicular to the $\{001\}_{\alpha-Fe}$ habit planes are about 3.8% and 47%, respectively. This anisotropic nature of the misfit-strain field together with the coherent nature of the interface between nitride platelets and ferrite matrix, induces the tetragonal distortion of the ferrite matrix adjacent to the nitride platelets (Fig. 2.4).

The lattice parameter of mixed $Ti_{1-x}Cr_xN$ nitride increases with increasing Ti/Cr atomic ratio (cf. Fig. 2.5). In view of the Bain orientation relationship and the lattice parameter of pure α-Fe this implies that the misfit-strain field surrounding the precipitates becomes more pronounced with increasing atomic Ti/Cr ratio. Indeed, the diffraction-line broadening observed for the ferrite matrix and the tetragonal distortion of the ferrite matrix as revealed by the intensity hump at the high-angle side of the $200_{\alpha\text{-}Fe}$ reflection increase with increasing Ti/Cr atomic ratio (cf. Fig. 2.1d).

The coherent nature of the nitride platelet/matrix interface makes adsorption of nitrogen at the octahedral interstices in the ferrite matrix *adjacent to* the platelet faces likely as in this way bonding to Ti and/or Cr in the platelet is realized, i.e. $[N]_{interface}$. Because the affinity of Ti for N is much higher than that of Cr for N, $[N]_{interface}$ increases with Ti/Cr, as observed (Fig. 2.8a). A similar observation was made for nitrided Fe-Cr-Al alloys where $[N]_{interface}$ increases with increasing Al/Cr atomic ratio [42]. Moreover, for increasing Ti/Cr atomic ratio the nitride-platelet thickness decreases (Table 2.4) implying that the amount of interfacial area between nitride precipitates and the matrix increases with increasing Ti/Cr atomic ratio. Obviously this effect contributes to an increase of $[N]_{interface}$ with increasing Ti/Cr atomic ratio, as well.

The presence of dissolved excess nitrogen in the ferrite matrix upon nitriding of Fe-Ti-Cr alloys is a consequence of elastic accommodation of the misfit between nitride platelet and ferrite matrix: such elastic accommodation of misfit induces a tensile hydrostatic stress component in the ferrite matrix [31]. As a consequence, as compared to the unstrained state, more nitrogen can be dissolved (on octahedral interstices) in the ferrite matrix; i.e. $[N]_{strain}$. Because the misfit increases with increasing Ti/Cr atomic ratio (see above), $[N]_{strain}$ increases with increasing Ti/Cr atomic ratio, as observed (Fig. 2.8b).

2.5 Conclusions

1. Upon nitriding of ternary iron-based Fe-Ti-Cr alloys highly coherent cubic, rock-salt crystal-structure type, mixed $Ti_{1-x}Cr_xN$ nitrides develop in the ferrite matrix. Separate TiN and CrN nitrides do not develop. Uptake of Cr in TiN is favored as it reduces the misfit-strain field in the ferrite matrix.

2. The misfit of the largely coherent nitride precipitates with the surrounding ferrite matrix is strongly anisotropic. As a consequence the nitride precipitates develop as platelets (length ≤ 30 nm and thickness ≤ 3 nm) obeying a Bain orientation relationship with the ferrite matrix with $\{100\}_{\alpha\text{-Fe}}$ habit planes, and are surrounded by a tetragonally distorted ferrite matrix. As a result cubic and tetragonal ferrite reflections can be discerned in both X-ray diffraction and selected area electron diffraction patterns.

3. The lattice parameter of the mixed $Ti_{1-x}Cr_xN$ nitride increases with increasing Ti/Cr atomic ratio. Consequently the misfit-strain field is most pronounced for the highest relative Ti content of the alloy, which corresponds with a microhardness increasing with increasing Ti/Cr atomic ratio.

4. The amount of excess nitrogen dissolved in the ferrite matrix, $[N]_{strain}$, increases with increasing Ti/Cr atomic ratio as a consequence of a tensile hydrostatic component of misfit stress increasing with increasing Ti/Cr atomic ratio.

5. The amount of excess nitrogen adsorbed at the nitride-platelet faces, $[N]_{interface}$, increases with increasing Ti/Cr atomic ratio because (i) Ti has a much larger affinity for

N than Cr and (ii) the relative amount of interfacial (nitride/matrix) area increases with

increasing Ti/Cr atomic ratio.

References

[1] S. Lampman, Introduction to surface hardening of steel. ASM Handbook: Heat Treating. Metals Park, Ohio, ASM International. 4 (1991) 259.

[2] E.J. Mittemeijer and J.T. Slycke, Surf. Eng. 12 (1996) 152.

[3] E.J. Mittemeijer and M.A.J. Somers, Surf. Eng. 13 (1997) 483.

[4] E.J. Mittemeijer, J. Metal. 37 (1985) 16.

[5] E.J. Mittemeijer, Mat. Sci. Forum 102-104 (1992) 223.

[6] P.M. Hekker, H.C.F. Rozendaal and E.J. Mittemeijer, J. Mater. Sci. 20 (1985) 718.

[7] R.E. Schacherl, P.C.J. Graat and E.J. Mittemeijer, Z. Metallkd. 93 (2002) 468.

[8] R.E. Schacherl, P.C.J. Graat and E.J. Mittemeijer, Metall. Mater. Trans. A, 35A (2004) 3387.

[9] B. Mortimer, P. Grieveson and K.H. Jack, Scand. J. Metals 1 (1972) 203.

[10] S.S. Hosmani, R.E. Schacherl and E.J. Mittemeijer, Mater. Sci. Technol. 21 (2005) 113.

[11] S.S. Hosmani, R.E. Schacherl and E.J. Mittemeijer, J. Mater. Sci. 43 (2008) 2618.

[12] M.H. Biglari, C.M. Brakman, E.J. Mittemeijer and S. Van Der Zwaag, Phil. Mag. A, 72 (1995) 931.

[13] M.H. Biglari, C.M. Brakman, M.A.J. Somers, W.G. Sloof, E.J. Mittemeijer and S. Van Der Zwaag, Z. Metallkd. 84 (1993) 124.

[14] M.H. Biglari, C.M. Brakman, E.J. Mittemeijer and S. Van Der Zwaag, Phil. Mag. A, 72 (1995) 1281.

[15] M.H. Biglari, C.M. Brakman, E.J. Mittemeijer and S. Van Der Zwaag, Metal. Mater. Trans. A 26A (1995) 765.

[16] W.D. Welch and S.H.Carpenter, Acta Metall. 21 (1973) 1169.

[17] A. Krawitz, Scripta Metall. 11 (1977) 117.

[18] S.S. Hosmani, R.E. Schacherl and E.J. Mittemeijer, Acta Mater. 53 (2005) 2069.

[19] S.S. Hosmani, R.E. Schacherl and E.J. Mittemeijer, Acta Mater. 54 (2006) 2783.

[20] D.H. Kirkwood, O.E. Atasoy and S. R. Keown, Metals. Sci. 8 (1974) 49.

[21] H.H. Podgurski and F.N. Davis, Acta Metall. 29 (1981) 1.

[22] D.S. Rickerby, S. Henderson, A. Hendry and K.H. Jack, Acta Metall. 34 (1986) 1687.

[23] D.H. Jack, Acta Metall. 24 (1976) 137.

[24] H. Hasegawa, A. Kimura and T. Suzuki, J. Vac. Sci. Technol. 18A (2000) 1038.

[25] S.M. Aouadi, J.A. Chladek, F. Namavar, N. Finnegan and S.L. Rohde, J. Vac. Sci. Technol. 20B (2002) 1967.

[26] M.A. Baker, T.P. Mollart, P.N. Gibson and W. Gissler, J. Vac. Sci. Technol. 15A (1997) 284.

[27] J. Vetter, H.J. Scholl and O. Knotek, Surf. Coat. Technol. 74-75 (1995) 286.

[28] T. Suzuki, D. Huang and Y. Ikuhara, Surf. Coat. Technol. 107 (1998) 41.

[29] E.C. Bain, Trans. AIME 70 (1924) 25.

[30] V.A. Phillips and A.U. Seybolt, Trans. TMS-AIME 242 (1968) 2415.

[31] M.A.J. Somers, R.M. Lankreijer and E.J. Mittemeijer, Phil. Mag. A, 59 (1989) 353.

[32] E. Lehrer, Z. Elektrochem. 36 (1930) 383.

[33] R. Hoffmann, E. J. Mittemeijer and M. A. J. Somers, HTM 51 (1996) 162.

[34] R. Delhez and E.J. Mittemeijer, J. Appl. Cryst. 8 (1975) 609.

[35] J.L. Pouchou and F. Pichoir, Rech. Aerosp. (1984) 167.

[36] A. Armigliato, L. Dori, A. Garulli and P. Venturi, J. Microsc. Spectrosc. Electron. 7 (1982) 593.

[37] N.E. Vives Diaz, S.S. Hosmani, R.E. Schacherl and E.J. Mittemeijer, Acta Mater. 56 (2008) 4137.

[38] A.R. Clauss, E. Bischoff, R.E. Schacherl and E.J. Mittemeijer, Metall. Mater. Trans. 40A (2009) 1923.

[39] Y. Massiani, P. Gravier, L. Fedrizzi and F. Marchetti, Thin Solid Films 261 (1995) 202.

[40] P. Hones, R. Sanjinés and F. Lévy, Thin Solid Films 332 (1998) 240.

[41] H.H. Podgurski and H.H. Knechtel, Trans. TMS-AIME 245 (1969) 1595.

[42] K.S. Jung, R.E. Schacherl, E. Bischoff and E.J. Mittemeijer, Surf. Coat. Technol. 204 (2010) 1942.

Chapter 3

Normal and excess nitrogen uptake by iron-based Fe-Cr-Al alloys; the role of the Cr/Al atomic ratio

K. S. Jung, R. E. Schacherl, E. Bischoff and E. J. Mittemeijer

Abstract

Upon nitriding ferritic iron-based Fe-Cr-Al alloys, containing a total of 1.50at.% (Cr + Al) alloying elements, with varying Cr/Al atomic ratio (0.21 - 2.00), excess nitrogen uptake occurred, i.e. more nitrogen was incorporated in the specimens than compatible with only inner nitride formation and equilibrium nitrogen solubility of the unstrained ferrite matrix. The amount of excess nitrogen increased with decreasing Cr/Al atomic ratio. The microstructure of the nitrided zone was investigated by X-ray diffraction (XRD), electron probe microanalysis (EPMA), transmission electron microscopy (TEM) and electron energy loss spectroscopy (EELS). Metastable, fine platelet-type, mixed $Cr_{1-x}Al_xN$ nitride precipitates developed in the nitrided zone for all of the investigated specimens. The degree of coherency of the nitride precipitates with the surrounding ferrite matrix was discussed in view of the anisotropy of the misfit. Analysis of nitrogen-absorption isotherms, recorded after subsequent pre- and de-nitriding treatments allowed to differentiate quantitatively different types of nitrogen taken up. The amounts of the different types of excess nitrogen as function of the Cr/Al atomic ratio were discussed in terms of the nitride/matrix misfit and the different chemical affinities of Cr and Al for N. The strikingly different nitriding behaviors of Fe-Cr-Al and Fe-Cr-Ti alloys could be explained on this basis.

3.1 Introduction

Nitriding is a thermochemical surface-treatment process of ferritic steel components in order to improve properties such as the resistances against fatigue, corrosion and wear [1-7]. In order to introduce nitrogen into the component, gaseous nitriding, employing NH_3-based atmospheres, is widely adopted. The application of a NH_3/H_2 gas mixture, instead of pure N_2 gas, makes it possible to impose, at 1atm and in a temperature range of 500 - 580°C, at the surface of the specimen to be nitrided, a chemical potential of nitrogen equivalent to that of thousands of atmospheres of N_2 gas. To this end the slow thermal dissociation of NH_3 under these conditions is crucial [8, 9].

Upon nitriding of iron-based binary alloys containing alloying elements with a strong affinity for nitrogen, such as Cr [10-21], Al [22-27], V [28-33] and Ti [34-37], alloying element nitride precipitates can develop in the diffusion zone.

Chromium and aluminum are often used together as alloying elements (Me) in commercial nitriding steels. Only very recently a few studies were devoted to the nitriding of such ternary iron-based Fe-Me_1-Me_2 alloys. Whereas, upon nitriding, in binary Fe-Cr alloys rapid precipitation of highly coherent, cubic rock-salt crystal-structure type CrN nitrides takes place [12, 13, 16], in binary Fe-Al alloys hexagonal, wurtzite, crystal-structure type AlN nitrides precipitate with difficulty, i.e. only slowly [23-26]. It was shown that the total amount of nitrogen taken up per atom alloying element Me was rather different for Fe-Cr and Fe-Al alloys.

Recent research on a ternary iron-based Fe-Cr-Al alloy has shown that nitriding of such an alloy leads to the precipitation of metastable, mixed $Cr_{1-x}Al_xN$ nitride precipitates of cubic, rock-salt crystal-structure type [38]. Then, in view of the above discussed different nitriding effects of Cr and Al in binary Fe-Me alloys, it is of interest

to quantitatively investigate the uptake of nitrogen by Fe-Cr-Al alloys, in particular as function of the Cr/Al atomic ratio, which is the purpose of the present project.

Using homogeneously nitrided foils of Fe-Cr-Al alloys with different Cr/Al atomic ratios ($0.21 \leq$ Cr/Al ≤ 2.00), while keeping the total amount of the alloying element at about 1.50at.%, so-called nitrogen-absorption isotherms (cf. section 3.3.4) were determined and discussed in terms of various types of absorbed nitrogen. The microstructure of the nitride zone and the morphology and composition of the nitride precipitates were investigated by means of X-ray diffraction (XRD), electron probe microanalysis (EPMA), transmission electron microscopy (TEM) and electron energy loss spectroscopy (EELS).

3.2 Experimental

3.2.1 Specimen preparation

Ingots of Fe-Cr-Al alloys, containing about 1.50at.% (Cr + Al), with the Cr/Al atomic ratio varying from 0.21 to 2.00 were prepared from pure Fe (99.98 wt.%, Alfa Aesar), pure Cr (99.999 wt.%, Alfa Aesar) and pure Al (99.999 wt.%, Alfa Aesar) using an inductive furnace. The alloys were cast into rods with a diameter of 10 mm and length of 100 mm. The precise composition of the Fe-Cr-Al alloys was analyzed, applying (i) inductive coupled plasma-optic emission spectroscopy (ICP-OES) to determine the content of the alloying elements Cr and Al, (ii) a combustion method to determine the light elements C and S and (iii) hot-extraction to determine the light elements O and N. The thus determined chemical compositions of the alloys are shown in Table 3.1.

The cast rods were cold-rolled to foils with a thickness about 0.2 mm in several steps and were cut into rectangular specimens (16×16 mm^2). After being polished, the foils were encapsulated in a quartz tube with an argon atmosphere and annealed at

700°C for 2h followed by air-cooling to obtain a recrystallized grain structure (grain size of about 20 - 50 μm). Before nitriding the specimens were ground and polished (last step: 1 μm diamond paste) and then cleaned in ethanol with ultrasonic agitation.

Table 3.1: The amounts of Cr and Al and light element impurities in the alloy specimens before nitriding.

element alloy	Cr	Al	N	O	S	C
	(at.%)		(μg/g)			
Fe-Cr-Al (Cr/Al = 0.21)	0.26 (±0.007)	1.22 (±0.008)	2 ± 1	12 ± 6	12	14
Fe-Cr-Al (Cr/Al = 0.52)	0.51 (±0.005)	0.99 (±0.009)	2 ± 1	12 ± 6	17	15
Fe-Cr-Al (Cr/Al = 1.04)	0.75 (±0.009)	0.72 (±0.006)	3 ± 1	12 ± 6	12	13
Fe-Cr-Al (Cr/Al = 2.00)	1.00 (±0.005)	0.50 (±0.005)	2 ± 1	12 ± 6	14	12

3.2.2 Nitriding; determination of nitrogen-absorption isotherms

The foils were suspended at a quartz fiber and placed in the middle of a vertical quartz tube furnace. The composition of the ammonia/hydrogen gas mixture (purity: $NH_3 >$ 99.998 vol.% and $H_2 >$ 99.999 vol.%) within the furnace was precisely controlled by fixing the ratio of the gas flows of both gases, using mass flow controllers. A linear gas velocity of 13.5 mm/s (at room temperature) was established by keeping the gas flow rate at 500 ml/min in view of the inner diameter of 28 mm of the quartz tube furnace. This linear gas flow is sufficient to avoid any significant (thermal) decomposition of ammonia in the nitriding atmosphere (cf. section 3.1 and Ref. 9).

In order to maintain a homogeneous precipitation morphology within the entire specimen during the determination of the nitrogen-absorption isotherms, pre- and de-nitriding experiments were carried out prior to the absorption-isotherm experiments. The pre-nitriding was performed at 580°C for 48h with a nitriding potential of r_N

($\equiv \dfrac{p_{NH_3}}{p_{H_2}^{3/2}}$, with p_i as partial pressure of component i [8]) = 0.104 atm$^{-1/2}$. This treatment

ensures through nitriding of the specimen, without iron-nitride formation at the surfaces

of the specimen. The specimen was quenched into water at room temperature after the

pre-nitriding, and subsequently de-nitrided in a H_2 atmosphere at 470°C for 72h. By de-

nitriding part of the nitrogen taken up by the specimen was removed (for this, see

section 3.3.4).

Nitrogen-absorption isotherms were then determined at a temperature of 560°C.

At this temperature (below the pre-nitriding temperature), the precipitation morphology

of the samples does not change. The determination of the absorption isotherms was

performed by determining the nitrogen uptake of foils after nitriding at 560°C for 72h

at each of the following nitriding potentials: r_N = 0.140, 0.117, 0.091 and 0.054 atm$^{-1/2}$

(under these nitriding conditions no iron nitrides can be formed at the surfaces of the

specimen). The nitriding and de-nitriding conditions for the different alloys have been

gathered in Table 3.2.

Table 3.2: Summary of the nitriding parameters for the Fe-Cr-Al alloys.

	temp. (°C)	time (h)	NH$_3$ (ml/min)	H$_2$ (ml/min)	r_N (atm$^{-1/2}$)
pre-nitriding	580	48	45	455	0.104
de-nitriding	470	72	·	500	·
absorption isotherms	560	72	58 50 40 25	442 450 460 475	0.140 0.117 0.091 0.054

The amount of nitrogen taken up was determined by weight measurements

before and after nitriding using a Mettler microbalance with an accuracy of 0.1 µg. In

order to obtain an accurate weight, the average value of ten measurements was taken.

The error bars and ranges indicated in Figs. 3.2b, 3.5-3.7 and Tables 3.3-3.7, respectively, represent the maximal deviation from the average value calculated on the basis of the ten weight measurements.

3.2.3 X-ray diffraction

X-ray diffractograms were recorded from the surface of all specimens before and after nitriding using a PANalytical (formerly Philips) X'Pert Multi–Purpose Diffractometer (MPD) in Bragg–Brentano geometry equipped with a graphite-diffracted beam monochromator set to Co–K_α (λ=1.7889Å) radiation. The specimens were rotated on a spinner around their vertical axis during each measurement, to improve crystal statistics. The diffraction angle 2θ was scanned over a range from 40° until 120° in steps of 0.05°. Detected phases were identified by the 2θ positions of their diffraction peaks in comparison with data from the ICDD data base [39]. The diffractograms were evaluated by fitting a Pearson VII profile-shape function, using Profile Fit 1.0c software, for the determination of peak position and full width at half maximum (FWHM) in the diffractograms.

3.2.4 Transmission electron microscopy and electron energy loss spectroscopy

Specimens for transmission electron microscopy (TEM) were prepared from the middle of the specimen as follows.

Discs (Φ = 3 mm) were punched out from sheets produced by removing material mechanically from both sides (faces) of a nitrided specimen. These discs were thinned by applying jet-electropolishing technique using a Struers Tenupol-3 apparatus (bath composition: 85vol.% acetic acid and 15vol.% perchloric acid, current: 26 mA $\leq$ I $\leq$ 41 mA, voltage: 15V $\leq$ U $\leq$ 20.5V, temperature: 278K $\leq$ T $\leq$ 280K, flow rate setting

"20" at a Struers Tenupol-3 apparatus and treatment time $160s \leq t \leq 275s$). After jet-electropolishing, the specimens were subsequently rinsed in ethanol, acetone and isopropanol. To generate a hole in the middle of the sample, the discs were fixed during the jet-electropolishing treatment between two platinum rings.

TEM analysis was performed using a Philips CM 200 transmission electron microscope operating at 200 kV. Bright field (BF) images and selected area diffraction patterns (SADPs) were taken by a CCD camera attached to the TEM apparatus.

Electron energy loss spectroscopy (EELS) was performed in a Zeiss 912 Omega TEM operating at 120 kV equipped with an in-column omega-type electron spectrometer. For the elemental mappings the "three-window method" was used: Two pre-edge images are recorded, which enables the background to be fitted according to an inverse power law ($I = AE^{-r}$, where I is the intensity, E is the energy loss and A and r are two fitting parameters) at each pixel in the image. The extrapolated background image is then subtracted from the post-edge image (i.e. at the ionization edge of the element of interest) to get the elemental map of interest which is weak as compared to the background contribution [40].

3.2.5 Electron probe microanalysis

The homogeneity of the distribution of the alloying elements Cr and Al and of nitrogen in the specimens was confirmed by electron probe microanalysis (EPMA) using a Cameca SX100 instrument. Pieces of the specimen were cut to prepare cross-sections by subsequently embedding of these pieces with Polyfast (Struers; a conductive bakelite resin with carbon filler embedding material), followed by grinding and polishing (last step: 1 μm diamond paste). A focused electron beam at an accelerating voltage of 15 kV and a current of 100 nA was applied. The concentrations of Fe, Cr, Al

and N in the specimen were determined by measuring the intensities of the characteristic $Fe\text{-}K_{\beta}$, $Cr\text{-}K_{\alpha}$, $Al\text{-}K_{\alpha}$ and $N\text{-}K_{\alpha}$ X-ray emission peaks at points 2 µm apart along lines traversing the entire specimen cross-sections. The concentration of each element was obtained by applying the $\Phi(\rho z)$-correction to the ratio of characteristic X-ray emission peak intensities of the specimen and that of a standard specimen (i.e. pure Fe, pure Cr, pure Al and γ'-Fe_4N). [41].

3.3 Results and evaluation

3.3.1 Pre-nitriding

To maintain a homogeneous precipitation morphology in the diffusion zone of the specimen during the nitrogen-absorption isotherm measurements a pre-nitriding treatment has been applied at an elevated temperature, i.e. a temperature higher than that applied for nitrogen-absorption isotherm determination. Further the (pre-)nitriding time should be long enough to establish homogeneity by through nitriding of the specimen. Thus the pre-nitriding treatment was performed for each alloy specimen (i.e. Cr/Al = 0.21, 0.52, 1.04 and 2.00) at 580°C for 48h with $r_N = 0.104$ $atm^{-1/2}$.

X-ray diffractograms recorded before and after pre-nitriding of Fe-Cr-Al (Cr/Al = 2.00) alloy are shown in Fig. 3.1a. Only α-Fe reflections can be observed before and after pre-nitriding. However, pronounced broadening of the α-Fe reflections after pre-nitriding occurs. The absence of separate nitride reflections and the strong broadening of the ferrite reflections are indicative of development of fine and coherent inner nitride precipitates within the ferrite matrix: the nitrides diffract coherently with the surrounding matrix (cf. the extensive discussion for nitrided Fe-V alloys in Ref. 42). The diffraction-line broadening is relatively most pronounced for the $200_{\alpha\text{-Fe}}$ reflection which is caused by the anisotropic nature of the (tetragonal) misfit-strain field around

the nitride precipitate and the consequence of a Bain-type orientation relationship [42, 43] between the $Cr_{1-x}Al_xN$ nitride precipitates and the ferrite matrix [38]. The diffraction-line broadening (as represented by the full width at half maximum, FWHM) increases with increasing Cr/Al ratio (Figs. 3.1b and c). In addition to the diffraction-line broadening, a shift of the intensity maximum of the $200_{\alpha\text{-Fe}}$ reflection towards lower diffraction angle, 2θ, occurs upon nitriding. This shift of the $200_{\alpha\text{-Fe}}$ intensity maximum also increases with increasing Cr/Al ratio (Figs. 3.1b and c).
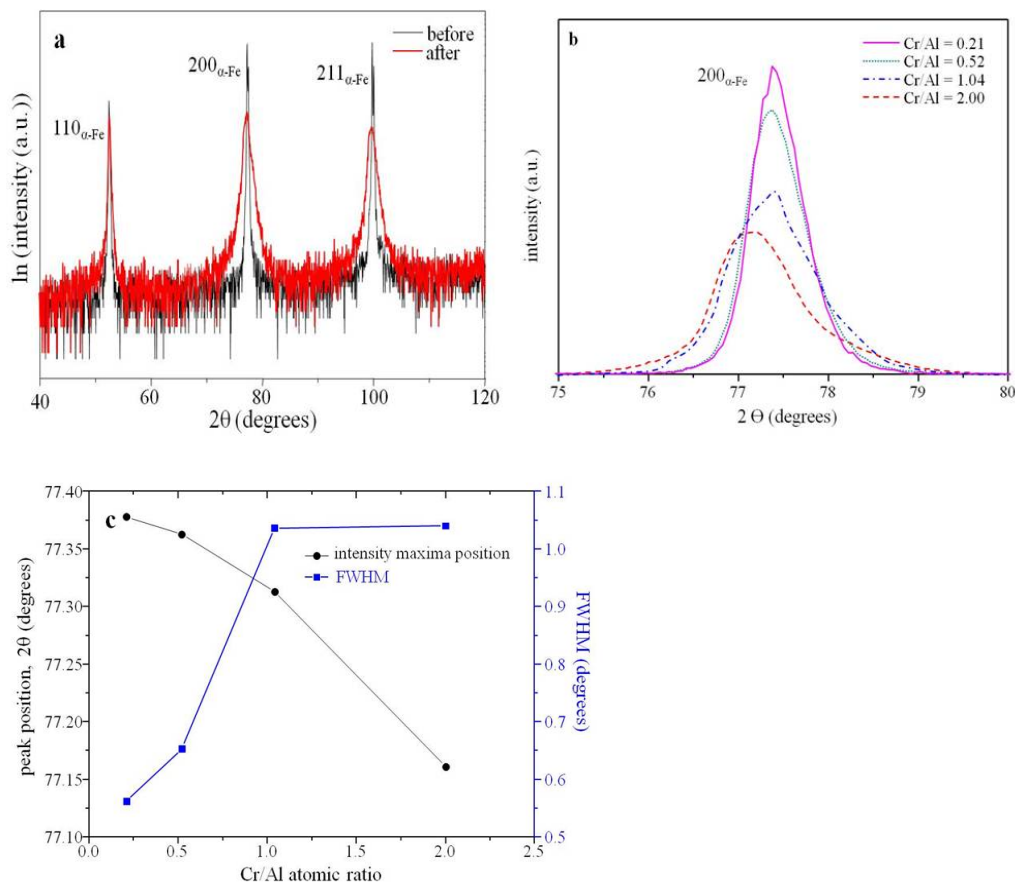
Fig. 3.1: (a) X-ray diffractograms ($40° < 2\theta < 120°$; Co-K_α radiation) before and after pre-nitriding of Fe-Cr-Al (Cr/Al = 2.00) alloy (note the logarithmic intensity scale). The nitriding experiment was performed at 580°C for 48h with nitriding potential $r_N = 0.104$ atm$^{-1/2}$. (b) X-ray diffractograms of the $200_{\alpha\text{-Fe}}$ reflection ($75° < 2\theta < 80°$, normalized with respect to integrated intensity; Co-K_α radiation) after prenitriding of Fe-Cr-Al (Cr/Al = 0.21, 0.52, 1.04 and 2.00) alloys. (c) The full width at half maximum (FWHM) and the position of the intensity maximum of the $200_{\alpha\text{-Fe}}$ reflection evaluated by fitting a Pearson VII profile-shape function as function of the Cr/Al atomic ratio.

The EPMA elemental-concentration depth profiles presented in Fig. 3.2a show that the concentrations of both alloying elements and of nitrogen are constant over the cross section of the specimen; distinct segregation at grain boundaries was not observed. For all (pre-) nitrided alloys/specimens the total amount of nitrogen, $[N]_{tot}$, taken up after pre-nitriding, as determined by EPMA measurements, matches within experimental accuracy the value as obtained by weight-change measurement.
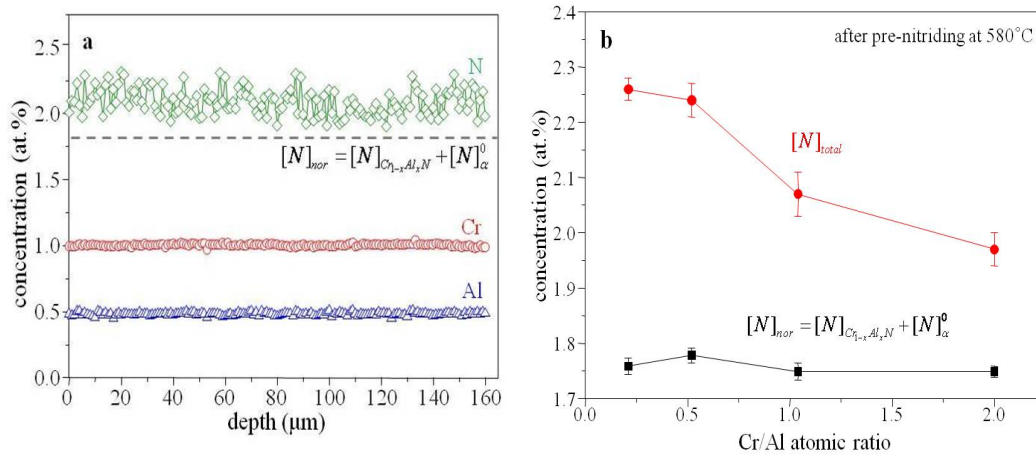
Fig. 3.2: (a) Concentration-depth profiles for N, Cr and Al as determined by EPMA after pre-nitriding (48h at 580°C with $r_N = 0.104$ atm$^{-1/2}$) of the Fe-Cr-Al (Cr/Al = 2.00) specimen. The horizontal line denotes the amount of "normal" nitrogen, $[N]_{nor}$: sum of the amounts of nitrogen necessary to precipitate all alloying elements as alloying element nitrides, $[N]_{Cr_{1-x}Al_xN}$, and of nitrogen dissolved interstitially in the unstrained ferrite matrix, $[N]_\alpha^0$. (b) The total amount of nitrogen taken up by the specimen, $[N]_{total}$, which can be compared with the amount of normal nitrogen, $[N]_{nor}$ (see also Fig. 3.2a), as function of the Cr/Al atomic ratio (after pre-nitriding of the Fe-Cr-Al alloys).

Evidently, after the homogeneous nitriding, the nitrogen uptake is larger than the amount of nitrogen required for the precipitation of all alloying element as nitride, $[N]_{(Me_1,Me_2)N}$, plus the amount of nitrogen necessary to establish the equilibrium solubility in an unstrained ferrite matrix, $[N]_\alpha^0$. This so called amount of "normal" nitrogen, $[N]_{nor} \equiv [N]_{(Me_1,Me_2)N} + [N]_\alpha^0$, has been indicated by the horizontal, dashed

line in Fig. 3.2a. The difference between the experimentally obtained total amount of nitrogen, $[N]_{tot}$, and the amount of "normal" nitrogen, $[N]_{nor}$, is defined as excess nitrogen, $[N]_{ex}$. Comparing the amounts of nitrogen taken up by the various alloys, it follows that the value of $[N]_{tot}$, and thus the value of $[N]_{ex}$, after pre-nitriding increases with decreasing Cr/Al ratio (Fig. 3.2b).

3.3.2 De-nitriding

Subsequent to the pre-nitriding, and also after the determination of each nitrogen-absorption isotherm, each alloy specimen was de-nitrided at 470°C in pure H_2 (500 ml/min) for 72h (see section 3.2.2). For each alloy, the remaining amounts of nitrogen after de-nitriding in both cases (after pre-nitriding and after nitrogen-absorption isotherm determination) are the same. This demonstrates that no significant aging effects (i.e. agglomeration and/or coarsening of nitride precipitates) occurred during the nitrogen-absorption isotherm measurements.

3.3.3 Morphology and crystallography of nitride precipitates

TEM bright field (BF) images obtained from pre-nitrided Fe-Cr-Al (Cr/Al = 2.00, 1.04 and 0.52) alloys showed that the nitrides precipitate as fine platelets surrounded by distinct strain-field contrast caused by the elastic distortion of the matrix around the misfitting precipitates (see Figs. 3.3a-c). From the micrographs it follows that the length of the nitride platelets increases (and the platelet density decreases) with decreasing Cr/Al atomic ratio.
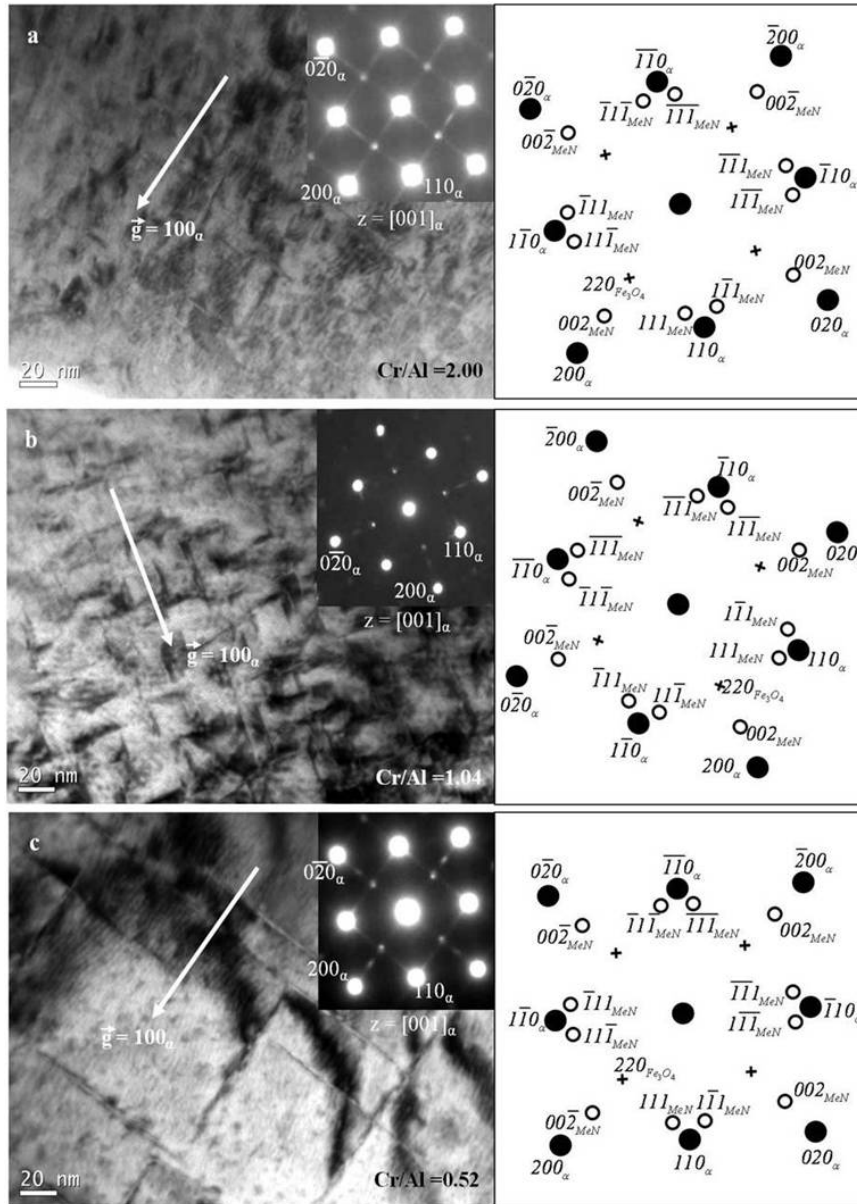
Fig. 3.3: TEM bright field images (left; electron-beam direction $[001]_{\alpha\text{-Fe}}$) showing platelet-type nitride precipitation in the ferrite matrix. (a) Fe-Cr-Al (Cr/Al = 2.00), (b) Fe-Cr-Al (Cr/Al = 1.04) and (c) Fe-Cr-Al (Cr/Al = 0.52). The corresponding SADPs are shown in the insets. Streaks passing through 200 and 020 type ferrite diffraction spots become less pronounced with decreasing Cr/Al atomic ratio and even intensity maxima at the position expected for 002 type diffraction spots of cubic, rock-salt crystal-structure type nitride become observable for the lowest Cr/Al atomic ratio (further, see text). Schematic diffraction patterns (right), corresponding with the SADPs shown, comply with a Bain orientation relationship of the nitride platelets with the α-Fe matrix (black dots: diffraction spots of the ferrite matrix; open circles: diffraction spots of the cubic, rock-salt crystal-structure type nitride precipitates). The spots in the SADPs at the position of forbidden $100_{\alpha\text{-Fe}}$ reflections, denoted by "x" in the schematic SADPs, are 220_{Fe3O4} spots caused by an iron oxide (Fe_3O_4) layer developed on the surface of the foil during TEM sample preparation.

Selected area diffraction patterns (SADPs) recorded from all specimens show diffraction spots at locations corresponding to the ferrite matrix. Further, streaks through the 200 and 020 type diffraction spots of the ferrite matrix can be observed. Intensity maxima on these streaks occur (see upper-right insets of Figs. 3.3a-c), at positions expected for 002 type spots of a cubic, rock-salt crystal-structure type nitride precipitate (see what follows).

The SADPs, with their streaks and diffraction spots, are compatible with the presence of nitride precipitates of cubic, rock-salt crystal-structure type in the ferrite matrix (bcc) satisfying a Bain orientation relationship:

$$(001)_{\alpha\text{-Fe}} // (001)_{\text{MeN}}, [100]_{\alpha\text{-Fe}} // [110]_{\text{MeN}} : \text{Me} = \text{Cr, Al}$$

The composition of the nitride platelets was investigated by electron energy loss spectroscopy (EELS). Comparing a TEM BF image comprising a part of the ferrite matrix containing precipitate platelets with correspondingly recorded elemental maps for N, Cr and Al (using N-K, Cr-$L_{2,3}$ (+ O-K) and Al-$L_{2,3}$- ionization edges) shows that N, Cr and Al enrichment occurs at the same locations, there where the precipitate platelets are observed in the TEM BF image (see arrows in Figs. 3.4a-d). Evidently the nitride precipitates developed as a mixed nitride: $Cr_{1-x}Al_xN$.
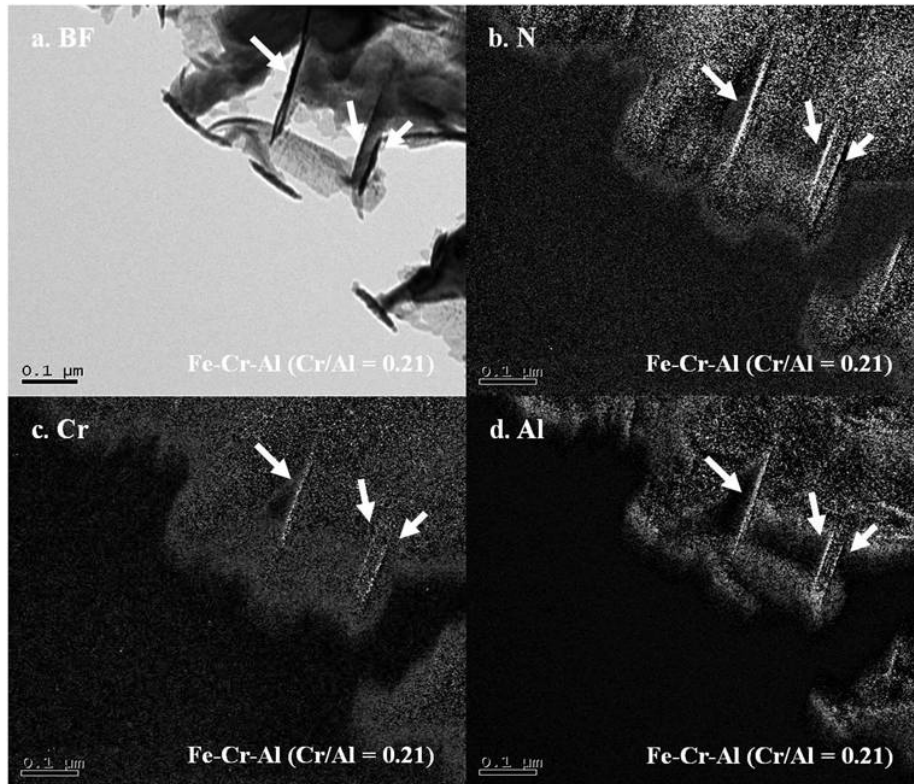
Fig. 3.4: (a) TEM bright field image (taken near to the hole in the jet-electropolished foil) of the nitrided Fe-Cr-Al (Cr/Al = 0.21) specimen and the corresponding elemental maps for (b) N, (c) Cr (+O) and (d) Al, as determined by EELS. The arrows indicate the (same) nitride platelet positions in (a)-(d). In case of Cr mapping, the background was determined in front of the O-K edge because of the overlapping O-K and Cr-L_{2-3} edges. Therefore the Cr mapping contains oxygen signal caused by surface oxidation which cannot be avoided.

Streaks through the 200 and 020 type spots of the ferrite matrix occur in particular for high Cr/Al atomic ratio; in that case the intensity maxima at the 002 type nitride spot positions on the streaks are less pronounced or even absent (cf. Fig. 3.3a). The reverse holds for low Cr/Al atomic ratio: less pronounced steaks and clearer intensity maxima (cf. Fig. 3.3c). Streaks, through 200 and 020 type ferrite-matrix diffraction spots, instead of separate nitride diffraction spots, are indicative of a highly coherent nature of the nitride/matrix interface and anisotropic misfit-strain in the ferrite matrix (in particular perpendicular to (001) ferrite-matrix lattice planes) due to the ultra-fine nitride precipitates, which can diffract coherently with the matrix (cf. Fig. 3.1

and its discussion in section 3.3.1). The decrease of the extent of streaking with decreasing Cr/Al atomic ratio in the specimen, indicates that the degree of coherency of the nitride precipitates with the ferrite matrix decreases, which development culminates with the emergence of 002 type diffraction spots of nitride precipitates of cubic, rock-salt crystal-structure type (Fig. 3.3c). Hence, the degree of coherency at the nitride-platelet/matrix interface increases with increasing Cr/Al atomic ratio.

3.3.4 Nitrogen-absorption isotherms

A nitrogen-absorption isotherm shows the dependence of the amount of nitrogen taken up by a (homogeneously) nitrided specimen as function of the nitriding potential, r_N (directly related to the chemical potential of nitrogen absorbed in the ferrite matrix at the ferrite/gas interface as imposed by a given nitriding atmosphere [8]). The analysis of nitrogen-absorption isotherms allows distinction of the various kinds of differently (chemically) bonded nitrogen in the specimen.

The amount of nitrogen dissolved in the ferrite matrix upon nitriding by means of an NH_3/H_2 gas mixture can be described by the equilibrium:

$$NH_3 \Leftrightarrow [N]_\alpha + \frac{3}{2}H_2 \tag{3.1}$$

where $[N]_\alpha$ denotes the amount of interstitially dissolved nitrogen in the octahedral interstices of the ferrite matrix. If K denotes the equilibrium constant of the above reaction it is immediately obtained for the concentration of dissolved nitrogen, $[N]_\alpha$

$$[N]_\alpha = K \cdot r_N \tag{3.2}$$

In view of the relatively small amount of dissolved nitrogen, Henrian behavior can be assumed and thus the equilibrium constant, K, is supposed to incorporate the constant

activity coefficient of dissolved nitrogen and thus is adopted as an effective equilibrium constant.

The nitrogen-absorption isotherms, as recorded after subsequent pre- and de-nitriding treatments (see sections 3.3.1 and 3.3.2), are shown for Fe-Cr-Al, with Cr/Al = 0.21, 0.52, 1.04 and 2.00, in Figs. 3.5a-d, respectively (see also Table 3.3).

Table 3.3: $[N]_{tot}$ for the Fe-Cr-Al alloys (nitrogen-absorption-isotherm measurements at 560°C for 72h).

r_N (atm$^{-1/2}$) alloy	0.054	0.091	0.117	0.140
Fe-Cr-Al (Cr/Al = 0.21): $[N]_{tot}$ (at.%)	2.13 (±0.02)	2.27 (±0.03)	2.34 (±0.02)	2.41 (±0.04)
Fe-Cr-Al (Cr/Al = 0.52): $[N]_{tot}$ (at.%)	2.12 (±0.01)	2.23 (±0.01)	2.32 (±0.01)	2.38 (±0.03)
Fe-Cr-Al (Cr/Al = 1.04): $[N]_{tot}$ (at.%)	1.90 (±0.01)	2.03 (±0.03)	2.11 (±0.02)	2.20 (±0.03)
Fe-Cr-Al (Cr/Al = 2.00): $[N]_{tot}$ (at.%)	1.88 (±0.03)	2.02 (±0.02)	2.10 (±0.01)	2.18 (±0.02)

At constant temperature the amount of interstitially dissolved nitrogen in the ferrite matrix should depend linearly on the nitriding potential, r_N (cf. Eq. (3.2)). Indeed, a straight line can be fitted well (using the least-squares method) to the data points of the total nitrogen content as function of the nitriding potential (dashed lines in Figs. 3.5). The extrapolation of such straight lines to nitriding potential $r_N = 0$ yields the nitrogen level indicated with 'C' on the ordinates as shown in Figs. 3.5a-d. The total nitrogen content minus nitrogen level C represents the nitrogen dissolved interstitially in the ferrite matrix.

The amounts of dissolved nitrogen are considerably larger than the amounts expected for pure ferrite in unstrained state (indicated with $[N]_\alpha^0$ in Figs. 3.5a-d, using literature data for pure ferrite [33]). The dissolved nitrogen in excess of $[N]_\alpha^0$ is

ascribed to the effect of a hydrostatic tensile stress component induced in the matrix by elastic accommodation of the misfit between nitride precipitate and surrounding matrix (see further below). This type of excess nitrogen is denoted as $[N]_{strain}$.
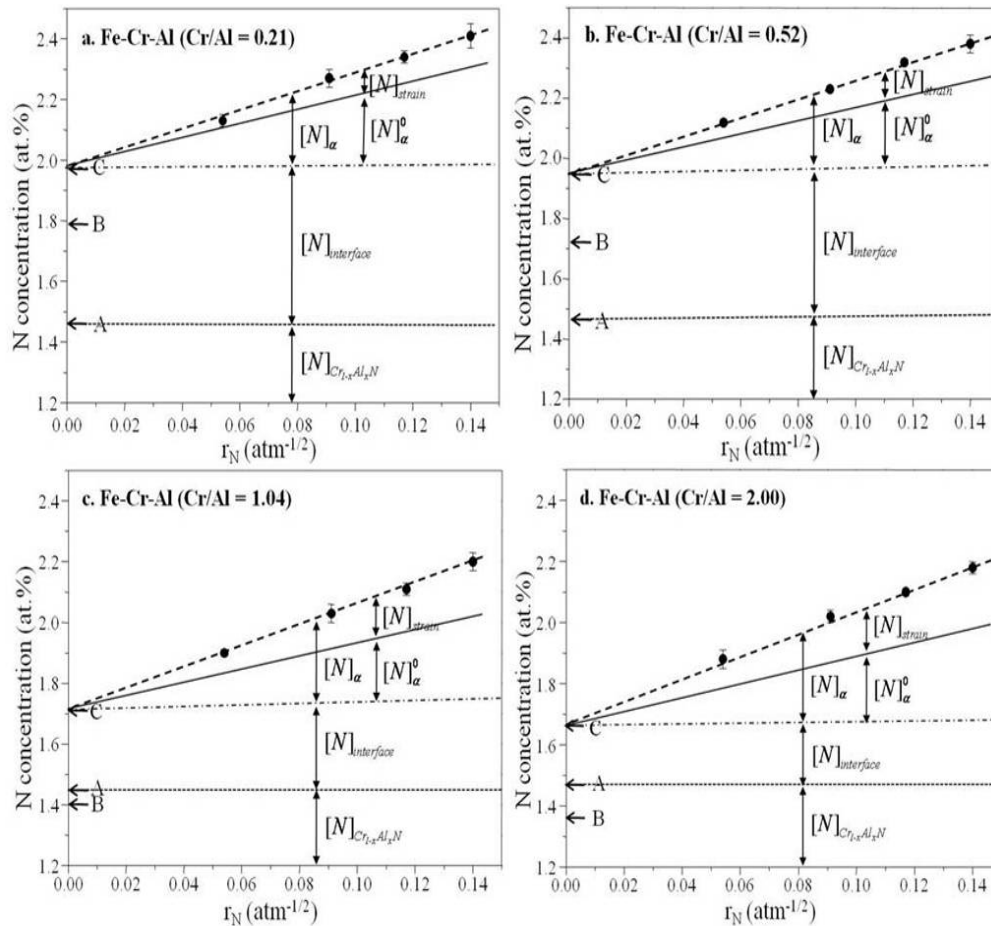
Fig. 3.5: Nitrogen absorption isotherms for (a) Fe-Cr-Al (Cr/Al = 0.21), (b) Fe-Cr-Al (Cr/Al = 0.52), (c) Fe-Cr-Al (Cr/Al = 1.04) and (d) Fe-Cr-Al (Cr/Al = 2.00) specimens measured at 560°C after subsequent pre- and de-nitriding (cf. section 3.2.2). The level 'A', represents the amount of nitrogen required for complete precipitation of Cr and Al to $Cr_{1-x}Al_xN$; the level 'B' is the amount of nitrogen left after de-nitriding and the level 'C' indicates the intersection of the linear portion of the absorption isotherm with the ordinate at $r_N = 0$ (further, see text).

The nitrogen level 'B' on the ordinates in Figs. 3.5a-d represents the amount of nitrogen left in the specimen after de-nitriding. The nitrogen level indicated with 'A' on the ordinates in Figs. 3.5a-d represents the amount of nitrogen required for the formation of the stoichiometric, mixed $Cr_{1-x}Al_xN$ nitride precipitates (i.e. $[N]_{Cr_{1-x}Al_xN}$),

according to the contents of alloying elements in the specimen (cf. Table 3.1). Values

for the nitrogen levels A, B and C for the specimens of different Cr/Al atomic ratio

have been gathered in Table 3.4.

Table 3.4: Nitrogen levels 'A', 'B' and 'C' (see Fig. 3.5), for the Fe-Cr-Al alloys.

N content (at.%) alloy	level A	level B	level C
Fe-Cr-Al (Cr/Al = 0.21)	1.46 (±0.015)	1.78 (±0.007)	1.99
Fe-Cr-Al (Cr/Al = 0.52)	1.48 (±0.014)	1.72 (±0.005)	1.95
Fe-Cr-Al (Cr/Al = 1.04)	1.45 (±0.015)	1.40 (±0.006)	1.71
Fe-Cr-Al (Cr/Al = 2.00)	1.48 (±0.010)	1.37 (±0.005)	1.67

The difference between the nitrogen levels C and A is interpreted as nitrogen

taken up (hypothetically at $r_N = 0$) in excess of the amount of nitrogen necessary to

precipitate all Cr and Al as $Cr_{1-x}Al_xN$. It has been proposed that this excess nitrogen is

located in *adsorbed* fashion at the faces of the (highly coherent) nitride platelets (in

octahedral interstices on top of Me atoms in the nitride-platelet surface; see also Ref.

33). Therefore the type of excess nitrogen represented by the difference C − A is

denoted as $[N]_{interface}$. The values determined for $[N]_{interface}$ have been gathered in Table

3.5 and Fig. 3.6. Evidently, $[N]_{interface}$ pronouncedly increases with decreasing Cr/Al

atomic ratio.

Table 3.5: The values of the $[N]_{interface}$ for the Fe-Cr-Al alloys (after prenitriding at 580°C).

N content (at.%) alloy	$[N]_{interface}$
Fe-Cr-Al (Cr/Al = 0.21)	0.53 (±0.015)
Fe-Cr-Al (Cr/Al = 0.52)	0.47 (±0.014)
Fe-Cr-Al (Cr/Al = 1.04)	0.26 (±0.015)
Fe-Cr-Al (Cr/Al = 2.00)	0.06 (±0.010)
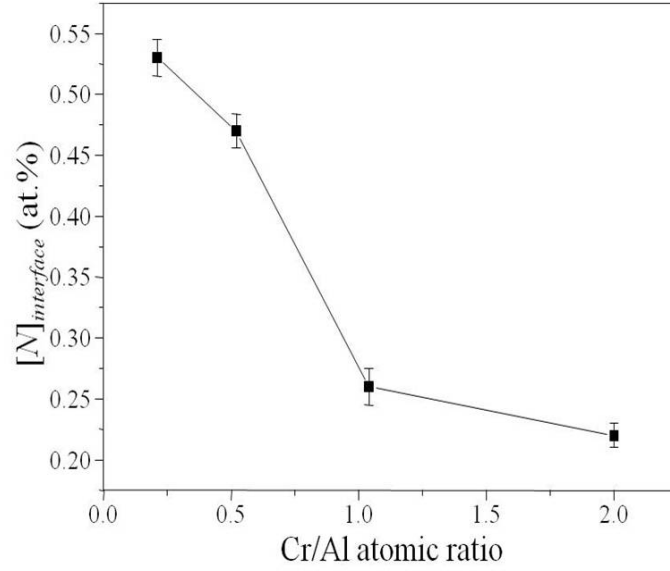
Fig. 3.6: $[N]_{interface}$ as function of the Cr/Al atomic ratio.

The composition of a $Cr_{1-x}Al_xN$ precipitate, incorporating the interfacial adsorbed excess nitrogen, $[N]_{interface}$, can be described as $Cr_{1-x}Al_xN_y$, where

$$y = \frac{[N]_{Cr_{1-x}Al_xN} + [N]_{interface}}{[N]_{Cr_{1-x}Al_xN}} = \frac{level\ C}{level\ A} \tag{3.3}$$

The value of y thus obtained contains indirect information on the average thickness of the precipitate platelet. As shown above (see section 3.3.3), $Cr_{1-x}Al_xN$ precipitates develop as platelets of cubic, rock-salt crystal-structure type obeying a Bain orientation relationship with the ferrite matrix. With $\{001\}_{Cr_{1-x}Al_xN}$ as habit plane, the thickness of a monolayer of $Cr_{1-x}Al_xN$ is one half of the lattice parameter of the rock-salt crystal structure (i.e. $\frac{a_{Cr_{1-x}Al_xN}}{2}$). If at every octahedral interstice in the ferrite matrix *at* the nitride/matrix interface one excess nitrogen atom is trapped (i.e. on top of a Me atom), it follows

$$y = \frac{n+2}{n} \tag{3.4}$$

where n is the number of $Cr_{1-x}Al_xN$ monolayers comprising the platelet. Thus the thickness t of a $Cr_{1-x}Al_xN$ platelet follows from

$$t = n \cdot \frac{a_{Cr_{1-x}Al_xN}}{2} = \frac{a_{Cr_{1-x}Al_xN}}{y-1} \qquad (3.5)$$

The lattice parameter of mixed $Cr_{1-x}Al_xN$ nitride can be calculated, for the Cr/Al atomic ratio concerned, by assuming that the lattice constant of mixed $Cr_{1-x}Al_xN$ nitride complies with Vegard's law and taking the lattice parameters of CrN (rock-salt crystal structure) and AlN (rock-salt crystal structure) as 4.14Å [44] and 3.94Å [45], respectively. Then the nitride-platelet thicknesses can be calculated using Eq. (3.5) from the now known values of y (cf. Eq. (3.3)) and $a_{Cr_{1-x}Al_xN}$. The results are presented in Table 3.6. It follows that the thickness of the nitride platelets increases with increasing Cr/Al atomic ratio.

Table 3.6: The mixed $Cr_{1-x}Al_xN_y$ nitride platelet thickness and corresponding y values (cf. Eq. (3.3)) for the Fe-Cr-Al alloys.

alloy	thickness (nm)	y
Fe-Cr-Al (Cr/Al = 0.21)	1.09 (±0.03)	1.36 (±0.010)
Fe-Cr-Al (Cr/Al = 0.52)	1.25 (±0.05)	1.32 (±0.012)
Fe-Cr-Al (Cr/Al = 1.04)	2.24 (±0.14)	1.18 (±0.012)
Fe-Cr-Al (Cr/Al = 2.00)	2.66 (±0.13)	1.15 (±0.008)

The values obtained for $[N]_{strain} (= [N]_{tot} - [N]_\alpha^0 - C)$ are shown as function of nitriding potential, r_N, in Fig. 3.7. Clearly, at constant r_N, $[N]_{strain}$ increases with increasing Cr/Al atomic ratio.
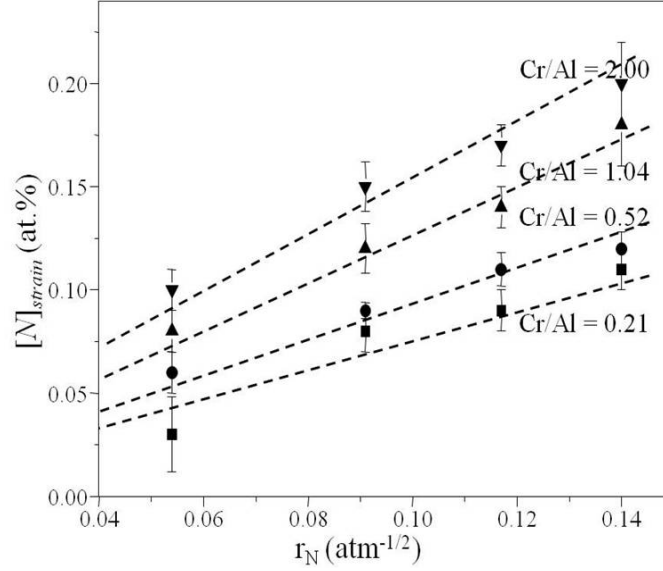
Fig. 3.7: $[N]_{strain}$ as function of the Cr/Al atomic ratio. The dashed-lines in the figure are least-squares fits of straight lines forced to pass through $r_N = 0$.

The presence of misfitting second phase particles in a matrix can lead to elastic distortions of the surrounding matrix. The corresponding stress field (characterized by a tensile hydrostatic component [46, 47]) influences the thermodynamics of nitrogen dissolution in the ferrite matrix. The enhancement of the lattice solubility, i.e. $[N]_{strain}$, with respect to that of the reference state (i.e. $[N]^0_\alpha$ for unstrained ferrite) can be given by [48]:

$$\frac{[N]_\alpha}{[N]^0_\alpha} = \exp\left[\frac{V_N}{RT}\left(\frac{4\varepsilon G_\alpha}{(1+\varepsilon)^3}CY^0_{(Me_1,Me_2)N_y}\right)\right] \qquad (3.6)$$

where $[N]_\alpha = [N]^0_\alpha + [N]_{strain}$ and with

misfit parameter: $\qquad \varepsilon = \dfrac{[V_{(Me_1,Me_2)N} + (y-1)fV_{(Me_1,Me_2)N}]^{1/3} - V_\alpha^{1/3}}{V_\alpha^{1/3}} \qquad (3.7)$

constant: $\qquad C = \dfrac{3K_{(Me_1,Me_2)N}}{(3K_{(Me_1,Me_2)N} + 4G_\alpha)} \qquad (3.8)$

volume fraction of $(Me_1, Me_2)N_y$:

$$Y^0_{(Me_1, Me_2)N_y} = \frac{[Me](V_{(Me_1, Me_2)N} + (y-1)fV_{(Me_1, Me_2)N})}{(1-[Me])V_\alpha + [Me](V_{(Me_1, Me_2)N} + (y-1)fV_{(Me_1, Me_2)N})} \qquad (3.9)$$

where V_N is the partial molar volume of nitrogen dissolved in the ferrite matrix, V_α and

$V_{(Me_1, Me_2)N}$ are the molar volumes of ferrite and the $(Me_1, Me_2)N$ precipitates, y is defined

by Eq. (3.3), G_α is the shear modulus of the ferrite matrix, $K_{(Me_1, Me_2)N}$ is the bulk

modulus of the $(Me_1, Me_2)N$ precipitate and $[Me]$ (= $[Cr + Al]/100$) is the atomic

fraction of alloying elements in the specimen. The parameter f describes the extent to

which the full misfit due to building out of the lattice of the $(Me_1, Me_2)N$ precipitates by

the adsorbed nitrogen atoms, which act as an entity with the particle, is experienced ($0 \leq$

$f \leq 1$). The following values have been adopted for some of the parameters mentioned

above (see Refs. 33 and 48):

V_N = 5.12 cm^3/mol; V_α = 7.092 cm^3/mol; G_α = 81.6 GPa; $V_{(Me_1, Me_2)N}$ = 9.44, 9.67, 9.90 and 10.12 cm^3/mol for Cr/Al atomic ratios of 0.21, 0.52, 1.04 and 2.00, respectively (using the procedure described below Eq. (3.5)); $K_{(Me_1, Me_2)N}$ = 285.98, 300.94, 316.43 and 330.67 GPa for Cr/Al atomic ratios of 0.21, 0.52, 1.04 and 2.00, respectively (derived from the bulk modulus data of K_{CrN} = 361 GPa [49] and K_{AlN} = 270 GPa [45] as linear function of the Cr/Al atomic ratio).

An experimental value for $[N]_\alpha / [N]^0_\alpha$, at a given nitriding temperature, follows

from the ratio of the slopes of the linear parts of the nitrogen-absorption isotherms

recorded for Fe-Cr-Al and pure α-Fe:

$$\frac{[N]_\alpha}{[N]^0_\alpha} = \frac{(\Delta[N]_\alpha / \Delta r_N)}{(\Delta[N]^0_\alpha / \Delta r_N)} = \frac{S_{Fe-Cr-Al}}{S^0_\alpha} \qquad (3.10)$$

where $S_{Fe-Cr-Al}$ and S^0_α denote the slope of the linear part of the absorption isotherms

for Fe-Cr-Al alloys and pure α-Fe, respectively (cf. Fig. 3.5; the absorption-isotherms

for pure α-Fe have been drawn as straight lines passing through the points C on the ordinates, using data from Ref. 33).

The values of all constants at the right-hand side of Eq. (3.6), except f (cf. Eqs. (3.7) and (3.9)), are known and thus by comparing Eqs. (3.6) and (3.10), values for f can be straightforwardly calculated from $\dfrac{S_{Fe-Cr-Al}}{S_\alpha^0}$. The thus obtained values for f, at r_N = 0.140 atm$^{-1/2}$, have been presented in Table 3.7 as function of the Cr/Al atomic ratio. It follows that the values obtained for f increase with increasing Cr/Al atomic ratio.

Table 3.7: The values for $\dfrac{S_{Fe-Cr-Al}}{S_\alpha^0}$ and f (cf. Eqs. (3.6-3.9)) at the nitriding potential, r_N = 0.140 atm$^{-1/2}$ for the Fe-Cr-Al alloys.

alloy	$\dfrac{S_{Fe-Cr-Al}}{S_\alpha^0}$	f
Fe-Cr-Al (Cr/Al = 0.21)	1.35 (±0.009)	0.10 (±0.04)
Fe-Cr-Al (Cr/Al = 0.52)	1.39 (±0.012)	0.12 (±0.01)
Fe-Cr-Al (Cr/Al = 1.04)	1.58 (±0.009)	0.84 (±0.04)
Fe-Cr-Al (Cr/Al = 2.00)	1.65 (±0.009)	0.96 (±0.04)

3.4 General discussion

The equilibrium crystal structures of the nitride precipitates occurring in (recrystallized and subsequently) nitrided Fe-Cr and Fe-Al alloys are the cubic, rock-salt structure for CrN [12, 13, 16] and the hexagonal, wurtzite structure for AlN [23-26]; a metastable rock-salt structure is possible for AlN [50, 51]. The formation of the cubic CrN upon nitriding is relatively fast, whereas the formation of the hexagonal AlN, due to the relatively large volume misfit between this nitride and the ferrite matrix, is relatively very slow [24]. At the nitriding temperature, diffusion of Cr and Al is that slow, as compared to diffusion of N, that the Al atoms are "dragged" into the developing cubic,

rock-salt type CrN precipitates: Upon nitriding the system accepts the gain of a smaller than maximal amount of energy, released by nitride precipitation, as an intermediate solution: metastable, mixed $Cr_{1-x}Al_xN$ precipitates develop (see Fig. 3.4). This has been shown recently to occur for a Cr/Al atomic ratio of 0.52 in Ref. 38. On the basis of this discussion it is likely that a more copious nucleation, i.e. a higher nucleus density of the cubic, rock-salt type, mixed $Cr_{1-x}Al_xN$ nitride, occurs for increasing Cr/Al atomic ratio of the alloy. The results obtained in the present work are in agreement with this prediction (cf. section 3.3.3).

The distinct dependence of $(Me_1,Me_2)N$ nucleus density (and nitride-platelet length and thickness) on Me_1/Me_2 atomic ratio, as observed here for nitrided Fe-Cr-Al alloys, has not been observed for nitrided Fe-Cr-Ti alloys, where mixed $Cr_{1-x}Ti_xN$ nitride platelets of rock-salt crystal structure occur as well for a similar range of the Me_1/Me_2 atomic ratio [52]. Indeed, in the latter case both equilibrium nitrides (CrN and TiN) have the rock-salt crystal structure, suggesting that the ease of nucleation of mixed $(Me_1,Me_2)N$ nitrides is less dependent on Me_1/Me_2 atomic ratio for Fe-Cr-Ti alloys than for Fe-Cr-Al alloys.

The coherent nature of the interface between nitride platelet and ferrite matrix allows adsorption of nitrogen atoms at the octahedral interstices in the ferrite matrix *adjacent to* the platelet faces, as in this way bonding to Cr and/or Al in the platelet faces is realized, i.e. $[N]_{interface}$. Now consider: (i) The chemical affinity of Al for N is much larger than that of Cr for N. Further, (ii) the thickness of the mixed $Cr_{1-x}Al_xN$ nitride platelets decreases with increasing relative Al concentration (i.e. with decreasing Cr/Al atomic ratio; see Table 3.6). Both effects (the chemical one (i) and the geometrical one (ii)) explain, that for a constant total atomic alloying element content (Cr + Al), $[N]_{interface}$ increases with decreasing Cr/Al atomic ratio, as observed (Fig. 3.6).

As follows from the position of level B, relative to the positions of levels C and A (cf. Figs. 3.5a-d), part (or all) of $[N]_{interface}$, and (for the atomic ratio Cr/Al > 1; cf. Fig. 3.5) a part of $[N]_{Cr_{1-x}Al_xN}$, can be removed (reversibly!) upon denitriding. These removable amounts of nitrogen increase relatively (i.e. with respect to $[N]_{interface}$) with increasing Cr/Al atomic ratio. This suggests that the larger the relative amount of Al, the smaller the relative amount of such removable nitrogen. Indeed the chemical affinity of Al for N is much larger than that of Cr for N. Thus N adsorbed at the nitride platelet faces can be overall stronger bonded at smaller Cr/Al ratios. A similar discussion may be given for the nitrogen incorporated in a metastable $Cr_{1-x}Al_xN$ platelet: at high Cr/Al atomic ratio this nitrogen is less strongly bonded, may be partly removed by denitriding during which Cr and Al atoms in the nitride platelet remain immobile (note the low temperature of denitriding), so that upon renitriding the nitrogen deficiency of the platelet becomes repaired, as observed.

A similar effect was not observed upon nitriding Fe-Cr-Ti alloys: Nitriding leads to the development of $Cr_{1-x}Ti_xN$ mixed nitrides of rock-salt crystal structure in a nitrogen saturated ferrite matrix. Upon denitriding all dissolved nitrogen from the ferrite matrix and all nitrogen adsorbed at the nitride-platelet faces is removed. But, in contrast with the $Cr_{1-x}Al_xN$ platelets, no nitrogen is removed from the $Cr_{1-x}Ti_xN$ platelets (for Cr/Ti atomic ratio in the range 0.53 to 2.22) [52]. This may be understood as a consequence of the $Cr_{1-x}Ti_xN$ platelets being relatively more stable (i.e. less metastable) than the $Cr_{1-x}Al_xN$ platelets (note that the equilibrium CrN and TiN nitrides both have a rock-salt crystal structure, whereas the equilibrium AlN nitride has a hexagonal, wurtzite crystal structure).

The presence of dissolved excess nitrogen in the ferrite matrix upon nitriding of Fe-Cr-Al alloys is a consequence of elastic accommodation of the misfit between nitride

platelet and ferrite matrix: such elastic accommodation of misfit induces a tensile hydrostatic stress component in the ferrite matrix [53, 46, 47]. As a consequence, as compared to the unstrained state, more nitrogen can be dissolved (on octahedral interstices) in the ferrite matrix; i.e. $[N]_{strain}$ [48]. Again comparing recent results obtained upon nitriding Fe-Cr-Ti alloys with the present data obtained for Fe-Cr-Al alloys, it strikes that $[N]_{strain}$ increases with increasing Cr/Me_2 atomic ratio if Me_2 = Al (Fig. 3.7) and decreases with increasing Cr/Me_2 atomic ration if Me_2 = Ti [52]. This can be understood as a consequence of the dependence of the nitride/matrix misfit on Cr/Me_2 atomic ratio, as follows.

The parameter ε (cf. Eq. (3.7)) describes the overall misfit between a "free", undeformed "inclusion" and an empty, undeformed "cavity" in a matrix. Upon insertion of the "inclusion" (here: the nitride particle) into the "cavity" in the matrix (here: the ferrite matrix) of finite size a hydrostatic stress is introduced in the matrix (of tensile nature if ε > 0). For the following comparative discussion, the effect of nitrogen adsorbed at the surface of the nitride particle can be ignored and thus ε can be taken as

$$\varepsilon = \left(\frac{V_{(Me_1,Me_2)N}^{1/3} - V_\alpha^{1/3}}{V_\alpha^{1/3}} \right) \tag{3.11}$$

Using the values of the lattice parameter of each nitride (4.14Å for rock-salt crystal-structure type CrN [44], 3.94Å for rock-salt crystal-structure type AlN [45] and 4.24Å for rock-salt crystal-structure type TiN [54]) and assuming that the lattice parameters of the mixed $Cr_{1-x}Al_xN$ and $Cr_{1-x}Ti_xN$ nitrides comply with Vegard's law, ε can be calculated as function of the Cr/Me_2 (Me_2 = Al or Ti) atomic ratio. The results are shown in Fig. 3.8a. Evidently, ε increases with increasing atomic ratio Cr/Al and decreases with increasing atomic ratio Cr/Ti. It thus is predicted that $[N]_{strain}$ increases with increasing Cr/Al atomic

ratio and with decreasing Cr/Ti atomic ratio, as observed (cf. Fig. 3.7 for Fe-Cr-Al alloys and Ref. 52 for Fe-Cr-Ti alloys).

In view of the observed Bain orientation relationship and the occurring $\{001\}_{\alpha\text{-}Fe}$-type habit plane (cf. section 3.3.3), the linear misfit along the habit plane (i.e. parallel to the faces of the nitride platelet), $\delta_{//}$ is given by

$$\delta_{//} = \left(\frac{a_{(Me_1,Me_2)N} - a_{\alpha-Fe}\sqrt{2}}{a_{\alpha-Fe}\sqrt{2}} \right) \times 100 \ (\%) \tag{3.12a}$$

and the linear misfit perpendicular to this habit plane (i.e. perpendicular to the faces of the nitride platelet) , $\delta_{\perp}$, obeys

$$\delta_{\perp} = \left(\frac{a_{(Me_1,Me_2)N} - a_{\alpha-Fe}}{a_{\alpha-Fe}} \right) \times 100 \ (\%) \tag{3.12b}$$

Using the same lattice-parameter data as indicated above, $\delta_{//}$ and $\delta_{\perp}$ can be calculated as function of the atomic ratio Cr/Me$_2$. The results are shown in Fig. 3.8b.
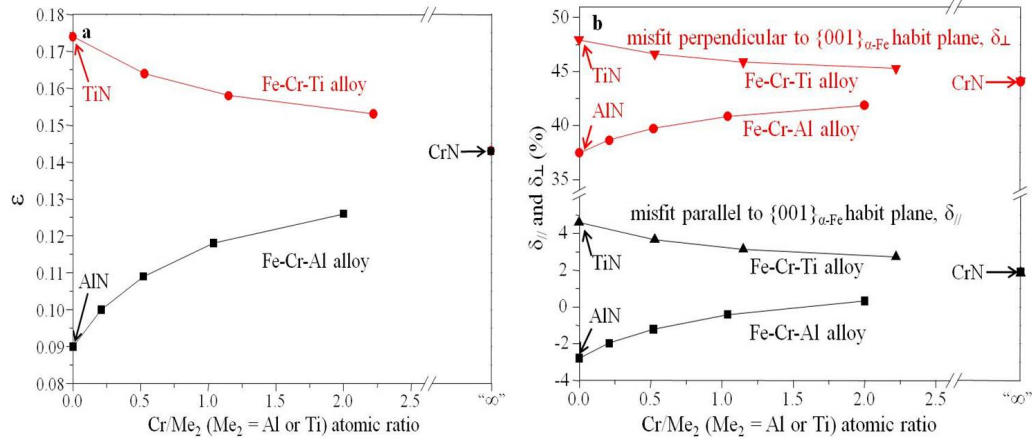

Fig. 3.8: (a) The overall misfit, ε (see Eq. (11)), between mixed nitride and ferrite matrix as function of Cr/Me$_2$ (Me$_2$ = Al or Ti). (b) The misfit perpendicular ($\delta_{\perp}$) and parallel ($\delta_{//}$) to the $\{001\}_{\alpha\text{-}Fe}$ habit plane for mixed $Cr_{1-x}Al_xN$ and $Cr_{1-x}Ti_xN$ nitrides as function of Cr/Me$_2$ (Me$_2$ = Al or Ti) atomic ratio.

For Fe-Cr-Ti alloys both $\delta_{/\!/}$ and $\delta_{\perp}$ are positive and decrease with increasing Cr/Ti atomic ratio. For Fe-Cr-Al alloys an antagonistic behaviour occurs: $\left|\delta_{\perp}\right|$ increases with increasing Cr/Al atomic ratio, whereas $\left|\delta_{/\!/}\right|$ decreases with increasing Cr/Al atomic ratio (for the alloys investigated within the range 0.21-2.00). Although the change of $\delta_{\perp}$ dominates the change of the overall misfit parameter ε (cf. Eq. (3.11) and thus is responsible for the increase of $[N]_{strain}$ with increasing Cr/Al atomic ratio (see above)), the decrease of $\left|\delta_{/\!/}\right|$ with increasing Cr/Al atomic ratio suggests that the nitride/matrix coherency at the faces of the nitride platelets increases with increasing Cr/Al atomic ratio and thus explains the observation of the more pronounced streaking through the 200 and 020 type ferrite-matrix diffraction-spots and the disappearing 200 type nitride diffraction spots with increasing Cr/Al atomic ratio (Fig. 3.3; section 3.3.3).

The value of f describes the extent to which the volume misfit due to the nitrogen, adsorbed at the interface is experienced (cf. section 3.3.3). Obviously, given a constant microstructure during the nitrogen absorption-isotherm measurements, the values of f determined in this work as function of the Cr/Al atomic ratio are characteristic for the pre-nitriding temperature (here 580°C). Of course, f will not depend in a direct way on the value of $[N]_{interface}$ (note that with increasing Cr/Al atomic ratio f increases (cf. Table 3.7) and $[N]_{interface}$ decreases (cf. Table 3.5)). Evidently, f will depend on the degree of coherency at the nitride-platelet/matrix interface and thus the increase of f with increasing Cr/Al atomic ratio can be conceived as a direct consequence of $\left|\delta_{/\!/}\right|$ decreasing with increasing Cr/Al atomic ratio (cf. the discussion in the previous paragraph).

3.5 Conclusions

1. Upon nitriding of Fe-Cr-Al alloys, metastable, mixed $Cr_{1-x}Al_xN$ nitrides of cubic, rock-salt crystal-structure type precipitate in the ferrite matrix; the system thus avoids the difficult nucleation of stable AlN (hexagonal, wurtzite structure type) precipitates in the ferrite matrix. The ease of mixed nitride nucleation and thus the nucleation density increases with increasing Cr/Al atomic ratio. Such an effect does not occur for nitrided Fe-Cr-Ti alloys as both equilibrium nitrides, CrN and TiN, have the same (rock-salt type) crystal structure as the corresponding metastable mixed $Cr_{1-x}Ti_xN$ precipitate.

2. The amount of excess nitrogen adsorbed at the faces of the nitride platelets, $[N]_{interface}$, increases with decreasing Cr/Me_2 (Me_2 = Al or Ti) atomic ratio because the chemical affinity of Me_2 for N is much larger than that of Cr for N and because the thickness of the nitride platelets decreases with decreasing Cr/Me_2 atomic ratio.

3. The amount of excess nitrogen dissolved in the ferrite matrix, $[N]_{strain}$, *increases* with increasing Cr/Me_2 atomic ratio for Me_2 = Al and *decreases* with increasing Cr/Me_2 atomic ratio for Me_2 = Ti. These antagonistic behaviours can be understood as consequences of the overall nitride/matrix misfit increasing with increasing Cr/Al atomic ratio and decreasing with increasing Cr/Ti atomic ratio.

4. The degree of coherency at the $Cr_{1-x}Al_xN$-platelet faces increases with increasing Cr/Al atomic ratio (TEM analysis), which reflects the decrease of the absolute value of the linear misfit parameter parallel to the interface, $|\delta_{//}|$, with increasing Cr/Al atomic ratio (for the alloys investigated within the range 0.21-2.00), opposite to the trend for the overall misfit parameter, ε.

Acknowledgements

References

[1] S. Lampman, Introduction to surface hardening of steel. ASM Handbook: Heat Treating. Metals Park, Ohio, ASM International. 4 (1991) 259.

[2] H. Ferkel, M. Glatzer, Y. Estrin, R.Z. Valiev, C. Blawert and B.L. Mordike, Mat. Sci. Eng. A 348 (2003) 100.

[3] M. Pellizzari, A. Molinari and G. Straffelini, Mat. Sci. Eng. A 352 (2003) 186.

[4] N. Limodin and Y. Verreman, Mat. Sci. Eng. A 435-436 (2006) 460.

[5] A. Basu, J. Dutta Majumdar, S. Ghosh Chowdhury, P.K. Ajikumar, P. Shankar, A.K. Tyagi, Baldev Raj and I. Manna, Surf. Coat. Technol. 201 (2007) 6985.

[6] T. Hirsch, T.G.R. Clarke and A. da Silva Rocha, Surf. Coat. Technol. 201 (2007) 6380.

[7] S. Jegou, L. Barrallier and R. Kubler, Acta Mater. 58 (2010) 2666.

[8] E.J. Mittemeijer and J.T. Slycke, Surf. Eng. 12 (1996) 152.

[9] E.J. Mittemeijer and M.A.J. Somers, Surf. Eng. 13 (1997) 483.

[10] G. Miyamoto, A. Yonemoto, Y. Tanaka, T. Furuhara and T. Maki, Acta Mater. 54 (2006) 4771.

[11] G. Miyamoto, A. Yonemoto, Y. Tanaka, T. Maki and T. Furuhara, ISIJ International 49 (2009) 1796.

[12] B. Mortimer, P. Grieveson and K.H. Jack, Scand. J. Metals 1 (1972) 203.

[13] K.H. Jack, Proc. Heat Treatment Conf. London 1973, The Metals Society, London (1975) 39.

[14] B.J. Lightfoot and D.H. Jack, Proc. Heat Treatment Conf. London 1973, The Metals Society, London (1975) 59.

[15] R.E.E. Pulkkinen, Scan. J. Metall. 12 (1983) 87.

[16] P.M. Hekker, H.C.F. Rozendaal and E.J. Mittemeijer, J. Mater. Sci. 20 (1985) 718.

[17] R.E. Schacherl, P.C.J. Graat and E.J. Mittemeijer, Z. Metallkd. 93 (2002) 468.

[18] R.E. Schacherl, P.C.J. Graat and E.J. Mittemeijer, Metall. Mater. Trans. A 35 (2004) 3387.

[19] S.S. Hosmani, R.E. Schacherl and E.J. Mittemeijer, Mater. Sci. Technol. 21 (2005) 113.

[20] S.S. Hosmani, R.E. Schacherl and E.J. Mittemeijer, J. Mater. Sci. 43 (2008) 2618.

[21] S.S. Hosmani, R.E. Schacherl, L.L. Dobrzyńska and E.J. Mittemeijer, Phil. Mag. A 88 (2008) 2411.

[22] H.H. Podgurski, R.A. Oriani and F.N. Davis, Trans. Metall. Soc. AIME 245 (1969) 1603.

[23] H.H. Podgurski and H.E. Knechtel, Trans. Metall. Soc. AIME 245 (1969) 1595.

[24] M.H. Biglari, C.M. Brakman, W.G. Sloof, E.J. Mittemeijer and S. Van Der Zwaag, Z. Metallkd. 84 (1993) 124.

[25] M.H. Biglari, C.M. Brakman, E.J. Mittemeijer and S. Van Der Zwaag, Phil. Mag. A 72 (1995) 1281.

[26] M.H. Biglari, C.M. Brakman, E.J. Mittemeijer and S. Van Der Zwaag, Phil. Mag. A 72 (1995) 931.

[27] H.J. Spies, H. Biermann and A. Fischer, Z. Metallkd. 96 (2005) 781.

[28] W.D. Welch and S.H. Carpenter, Acta Metall. 21 (1973) 1169.

[29] M. Pope, P. Grieveson and K.H. Jack, Scand. J. Metall. 2 (1973) 29.

[30] A.D. Krawitz, Scripta Metall. 11 (1977) 117.

[31] M.M. Yang and A.D. Krawitz, Metall. Trans. A 15 (1984) 1545.

[32] S.S. Hosmani, R.E. Schacherl and E.J. Mittemeijer, Acta Mater. 53 (2005) 2069.

[33] S.S. Hosmani, R.E. Schacherl and E.J. Mittemeijer, Acta Mater. 54 (2006) 2783.

[34] D.H. Kirkwood, O.E. Atasoy and S.R. Keown, Metals. Sci. 8 (1974) 49.

[35] D.H. Jack, Acta Metall. 24 (1976) 137.

[36] D.S. Rickerby, S. Henderson, A. Hendry and K.H. Jack, Acta Metall. 34 (1986) 1687.

[37] H.H. Podgurski and F.N. Davis, Acta Metall. 29 (1981) 1.

[38] A.R. Clauss, E. Bischoff, R.E. Schacherl and E.J. Mittemeijer, Metall. Mater. Trans. A 40 (2009) 1923.

[39] JCPDS-International Center for Diffraction Data (2002), PCPDFWIN, Version 2.3

[40] P. Crozier, Ultramicroscopy 58 (1995) 157.

[41] J.L. Pouchou and F. Pichoir, Rech. Aerosp. (1984) 167.

[42] N.E. Vives Diaz, S.S. Hosmani, R.E. Schacherl and E.J. Mittemeijer, Acta Mater. 56 (2008) 4137.

[43] E.C. Bain, Trans. AIME 70 (1924) 25.

[44] M. Nasr Eddine, E.F. Bertaut and M. Maunaye, Acta Crystallogr. B 33 (1977) 2696.

[45] N.E. Christensen and I. Gorczyca, Phys. Rev. B 47 (1993) 4307.

[46] E.J. Mittemeijer, P. Van Mourik and Th. D. De Keijser, Phil. Mag. A 43 (1981) 1157.

[47] E.J. Mittemeijer and A. Van Gent, Scripta Metall. 18 (1984) 825.

[48] M.A.J. Somers, R.M. Lankreijer and E.J. Mittemeijer, Phil. Mag. A 59 (1989) 353.

[49] F. Rivadulla, M. Banobre-Lopez, C.X. Quintela, A. Pineiro, V. Pardo, D. Baldomir, M.A. Lopez-Quintela, J. Rivas, C.A. Ramos, H. Salva, J.S. Zhou and J.B. Goodenough, Nature Mater. 8 (2009) 947.

[50] W.T. Lin, L.C. Meng, G.J. Chen, H.S. Liu, Appl. Phys. Lett. 66 (1995) 2066.

[51] Z.M. Ren, Y.F. Lu, H.Q. Ni, T.Y.F. Liew, B.A. Cheong, S. Chow, M.L. Ng and J.P. Wang, J. Appl. Phys. 88 (2000) 7346.

[52] K.S. Jung, R.E. Schacherl, E. Bischoff and E.J. Mittemeijer, HTM J. Heat Treatm. Mat. 65 (2010) 237.

[53] J.D. Eshelby, Solid St. Phys. 3 (1956) 79.

[54] W. , S. Binder, K. Aigner, P. Ettmayer, A. Guillou, J. Debuigne and G. Groboth, J. Alloys. Compd. 217 (1995) 137.

Chapter 4

The kinetics of the nitriding of ternary Fe-2at.%Cr-2at.%Ti alloy

K.S. Jung, R.E. Schacherl, E. Bischoff and E.J. Mittemeijer

Abstract

The mechanism and the kinetics of growth of the nitrided zone of ternary Fe-2at.%Cr-2at.%Ti alloy was investigated by performing gaseous nitriding experiments at temperatures 560°C and 580°C and at nitriding potentials $r_N = 0.004$ atm$^{-1/2}$ and 0.054 atm$^{-1/2}$. The microstructure of the nitrided zone was investigated by transmission electron microscopy (TEM) and the elemental compositional variation with depth was determined employing electron probe microanalysis (EPMA). Fine platelet-type, mixed $Cr_{1-x}Ti_xN$ nitride precipitates developed in the nitrided zone. To describe the evolution of the nitrogen-concentration depth profile, a numerical model was developed that has as important parameters: the surface nitrogen content, the solubility product(s) of the alloying elements and dissolved nitrogen in the ferrite matrix, and a parameter defining the composition of the inner nitride precipitates. These parameters were determined by fitting model-calculated nitrogen-depth profiles to the corresponding experimental data. The results obtained demonstrate that the type of nitride formation (i.e. whether Cr and Ti precipitate separately, as CrN and TiN, or jointly, as mixed $Cr_{1-x}Ti_xN$) as well as the amounts of mobile and immobile excess nitrogen, taken up by the specimen considerably influence the shape and extent of the nitrogen-concentration profiles.

4.1 Introduction

Nitriding is a thermochemical surface treatment which has been applied successfully in industry in order to improve properties of iron-based steel components, such as the resistances against fatigue, wear and corrosion [1-7]. It would be of great advantage to be able to describe the kinetics of the nitriding process quantitatively in order to tune the resulting microstructure and thus to optimize the properties of the components. Unfortunately, present-day knowledge does not allow such model-based nitriding:

So-called nitriding steels, as used in technology, usually contain more than one alloying element exhibiting a large affinity for nitrogen. As compared to a vast body of literature on the nitriding behaviour of binary iron-based alloys [8-30], only recently fundamental research on the nitriding behaviour of ternary iron-based $Fe-Me_1-Me_2$ alloys has been initiated. Questions to be addressed are: do Me_1 and Me_2 precipitate as separate nitrides (simultaneously or sequentially) or, as mixed nitride (jointly)? Recent research on Fe-Cr-Al alloys has demonstrated that mixed nitrides can develop, metastably, of a crystal structure (even) incompatible with the equilibrium crystal structure of the separate nitrides [31]. It was further shown that the ternary alloys can absorb amounts of nitrogen considerably larger than necessary for precipitation of all alloying elements as nitride and equilibrium saturation of the unstrained ferrite matrix: excess nitrogen [32, 33]. Against this background it is deemed necessary to investigate if the kinetics of the nitriding process for such alloys (i) sensitively reflects the operating mechanism of nitriding and (ii) allows determination of physically meaningful parameters which provide a quantitative description of the nitride-precipitation process. Thus not only understanding of the nitride precipitation is obtained, but also the avenue to model-based optimization of the nitrided microstructure of a multicomponent alloy becomes opened.

A quantitative description of the nitriding kinetics, as exhibited by the (shape) evolution of the nitrogen-concentration depth profile, should (at least) express the roles of the diffusion of nitrogen through the matrix and the rate of precipitation of the alloying element nitrides. The shape of the nitrogen-concentration depth profile depends strongly on the strength of the interaction of the alloying elements with nitrogen and thus can be categorized as follows

i)   Strong interaction: a surface-adjacent case develops, where *all* Me atoms have precipitated. A sharp nitrided case/unnitrided core boundary occurs.

ii) Weak interaction: nitride precipitation progresses with the same rate at each depth below the surface. A nitrogen gradient is virtually absent.

iii) Intermediate interaction: depending on temperature and alloying element concentration, nitriding behavior varying between weak and strong interaction can occur, characterized by a diffuse nitrided case/unnitrided core boundary.

Only for the extreme case of strong Me-N interaction in a binary Fe-Me alloy a simple analytical formulation of process kinetics is possible [34]:

$$z^2 = \left(\frac{2 \cdot c_{N_\alpha}^s \cdot D_N}{n \cdot c_{Me}} \right) \cdot t \qquad (4.1)$$

where z denotes the extent of the diffusion zone (depth range below the specimen surface), $c_{N_\alpha}^s$ is the nitrogen concentration at the specimen surface, D_N is the diffusivity of the nitrogen at a given temperature, n denotes the stoichiometry of the MeN$_n$ precipitates, c_{Me} is the Me concentration, and t denotes the nitriding time.

Considering the common case of intermediate interaction, the nitriding of ternary Fe-Me$_1$-Me$_2$ alloys and the kinetic effects of excess nitrogen uptake, a much more general approach, leading to a numerical model, is required. A first attempt was presented in Ref. 35; however the calculated model results did not match the

experimental data obtained. This is most likely due to the not considered but possibly occurring mixed nitride formation as well as ignorance of the role of mobile excess nitrogen. A completely different approach was presented in Refs. 36 and 37 where trapping of nitrogen in Fe-Me-N configurations was proposed. This approach is in conflict with the physical reality of precipitation of genuine nitride particles. The (numerical) model proposed in the present paper provides a quantitative description of the nitriding kinetics of ternary Fe-Me$_1$-Me$_2$ alloys where, for the first time, the consequences of (i) precipitation of either separate or mixed alloying element nitrides and (ii) mobile and immobile excess nitrogen (see section 4.2 for these notions) taken up in the nitrided zone, can be modeled and thus investigated. The model has been applied to the nitriding of Fe-2at.%Cr-2at.%Ti alloy; both Cr and Ti have a strong affinity for nitrogen. The (crystal) structure of the nitride precipitates and the microstructure of the nitrided zone were investigated by transmission electron microscopy (TEM). The nitrogen concentration-depth profiles in the diffusion zone were determined by electron probe microanalysis (EPMA). The experimentally obtained nitrogen-concentration depth profiles were compared with those calculated by the proposed model.

4.2 Theoretical background

4.2.1 Basis

In the following the nitride to be precipitated is denoted as "MeN$_n$", which stands for either one of the separate nitrides Me$_1$N$_n$ and Me$_2$N$_n$ or the mixed nitride (Me$_1$,Me$_2$)N$_n$ developing upon nitriding the ternary Fe-Me$_1$-Me$_2$ alloy. Previous work has shown that the total amount of nitrogen taken up by the specimen in equilibrium with the nitriding gas atmosphere, $[N]_{tot}^0$, can be subdivided in three contributions [30-32]: (i) nitrogen

incorporated in the nitride precipitates, $[N]^0_{MeN_n}$; (ii) nitrogen adsorbed at the nitride/matrix interfaces, the so-called immobile excess nitrogen, $[N]^0_{imm, exc}$ and (iii) nitrogen dissolved in the matrix which is the sum of the amount of dissolved nitrogen in pure, unstrained ferrite, $[N]^0_\alpha$, and the amount of excess dissolved nitrogen due to the nitride/matrix misfit-strain field, the so-called mobile excess nitrogen, $[N]^0_{mob, exc}$. Thus:

$$[N]^0_{tot} = [N]^0_{MeN_n} + [N]^0_{imm, exc} + ([N]^0_\alpha + [N]^0_{mob, exc}) \tag{4.2}$$

In case of an inhomogeneously nitrided specimen, the total amount of nitrogen at depth z, $[N]_{tot}$, is given by an equation like Eq. (4.2), albeit with $[N]^0_{MeN_n}$ and $[N]^0_\alpha$ replaced by $[N]_{MeN_n}$ and $[N]_\alpha$; moreover the amounts of immobile and mobile excess nitrogen depend on the degree of precipitation (i.e. on $[N]_{MeN_n}$) and thus depend on depth as well and accordingly $[N]^0_{imm, exc}$ and $[N]^0_{mob, exc}$ have to be replaced by $[N]_{imm, exc}$ and $[N]_{mob, exc}$.

Obviously, the dissolved excess nitrogen takes part in the diffusion of nitrogen through the matrix and therefore is called mobile excess nitrogen, whereas the adsorbed excess nitrogen is bonded to the nitride particles and therefore is called immobile excess nitrogen. Both types of excess nitrogen considerably influence the nitriding kinetics (see what follows).

The inward diffusion of (dissolved) nitrogen in the ferrite matrix can be expressed by Fick's second law:

$$\frac{\partial c_{N_\alpha}(z,t)}{\partial t} = D_N \cdot \frac{\partial^2 c_{N_\alpha}(z,t)}{\partial z^2} \tag{4.3}$$

where $c_{N_\alpha}(z,t)$ is the (fractional) concentration of nitrogen dissolved in the ferrite matrix at depth z and time t and at a given temperature, T. D_N is the diffusion

coefficient of nitrogen in the ferrite matrix, taken to be independent of nitrogen concentration (note that the values of c_{N_α} are low: < 1 at.%) .

The formation of nitride Me_1N_n or nitride Me_2N_n in the ferrite matrix can be expressed as:

$$Me_i + nN \Leftrightarrow Me_iN_n \tag{4.4a}$$

with Me_i and N as the Me_1 or Me_2 and nitrogen dissolved in the ferrite matrix. Similarly for the formation of mixed $(Me_{1,\,1-x}Me_{2,\,x})N_n$ (x < 1) nitride can be written as:

$$(1-x)Me_1 + xMe_2 + nN \Leftrightarrow (Me_{1,\,1-x}Me_{2,\,x})N_n \tag{4.4b}$$
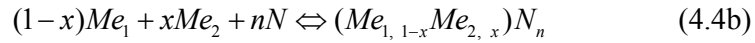
The equilibrium constants of the above reactions, K_e, are given by:

$$K_e = \frac{1}{[Me_i] \cdot [N]^n} = \frac{1}{K_{Me_iN_n}} \tag{4.5a}$$

$$K_e = \frac{1}{[Me_1]^{1-x} \cdot [Me_2]^x \cdot [N]^n} = \frac{1}{K_{(Me_{1,\,1-x}Me_{2,\,x})N_n}} \tag{4.5b}$$

where $[A]$ denotes the concentration of component A dissolved in the ferrite matrix, with $K_{Me_iN_n}$ and $K_{(Me_{1,\,1-x}Me_{2,\,x})N_n}$ as the solubility products, $K_{Me_iN_n} = [Me_i] \cdot [N]^n$ and $K_{(Me_{1,\,1-x}Me_{2,\,x})N_n} = [Me_1]^{1-x} \cdot [Me_2]^x \cdot [N]^n$, respectively. Upon nitriding, precipitation of either separate Me_iN_n nitrides or mixed $(Me_{1,\,1-x}Me_{2,\,x})N_n$ nitride will take place at a certain location in the diffusion zone when it holds

$$[Me_i] \cdot [N]^n > K_{Me_iN_n} \tag{4.6a}$$

$$[Me_1]^{1-x} \cdot [Me_2]^x \cdot [N]^n > K_{(Me_{1,\,1-x}Me_{2,\,x})N_n} \tag{4.6b}$$

4.2.2 Numerical modeling of nitrogen-concentration depth profile

The presence of immobile excess nitrogen adsorbed at the nitride/matrix interface in the present work can be taken into account by replacing the stoichiometric parameter n in the separate Me_iN_n nitrides or the mixed $(Me_{1,\,1-x}Me_{2,\,x})N_n$ nitride by $n' = n + y$ with y as the contribution of the immobile excess nitrogen (For the nitrides occurring in the nitrided Fe-based Fe-Cr-Ti alloys it holds $n = 1$ (cf. section 4.4.2)).

Precipitation of alloying element nitride, at a certain location in the alloy, occurs if the inequality (4.6) is satisfied for the nitride considered. This can be expressed as that the ratio, u

$$u_{Me_iN} = \frac{[Me_i] \cdot [N]^n}{K_{Me_iN_n}} \tag{4.7a}$$

$$u_{Me_{1,\,1-x}Me_{2,\,x}N} = \frac{[Me_1]^{1-x} \cdot [Me_2]^x \cdot [N]^n}{K_{(Me_{1,\,1-x}Me_{2,\,x})N_n}} \tag{4.7b}$$

takes a value larger than one. For the ternary Fe-Me$_1$-Me$_2$ alloy, two precipitation sequences can be discerned:

Firstly, it can be supposed that the alloying elements precipitate as separate nitrides, i.e. as Me_1N_n and Me_2N_n. If one of the u values according to Eq. (4.7a) (i.e. either u_{CrN} or u_{TiN} in the present work) is larger than one, then in the time step and at the location/depth considered, an amount of corresponding nitride is allowed to precipitate until the u value of this nitride equals one. If the u values according to Eq. (4.7a) for both alloying element nitrides (i.e. u_{CrN} and u_{TiN} in the present work) are larger than one, then, for the time step and at the location/depth considered, an amount of the nitride with the highest u value is allowed to precipitate until the u value of this nitride has become smaller than the u value of the other nitride. Then, still in the same time step, and at the same location/depth, the other nitride is allowed to precipitate, etc.

This approach is followed, in the time step and at the location/depth considered, until both u values have become equal to one.

Secondly, it can be supposed that the alloying elements precipitate as a mixed $(Me_{1,\,1-x}Me_{2,\,x})N_n$ nitride. In this case, precipitation of the mixed nitride, in the time step and at the location/depth considered, occurs if $u_{(Me_{1,\,1-x}Me_{2,\,x})N_n}$ is larger than one, and with an amount leading to reduction of $u_{(Me_{1,\,1-x}Me_{2,\,x})N_n}$ to one.

For each time step, j ($j = 0, 1, 2 \ldots$), at each location/depth considered, the amounts of Me_1, Me_2 and N remaining in solid solution, after completion of precipitations in time step j as described above, comply with:

for precipitation of separate nitrides $Me_iN_{n'}$:

$$([Me_i]^{j-1} - \frac{\Delta[N]^j}{n'}) \cdot ([N]^{j-1} - \Delta[N]^j) = K_{Me_iN_n} \quad (j \geq 1) \qquad (4.8a)$$

and for precipitation of mixed nitride $(Me_{1,\,1-x}Me_{2,\,x})N_{n'}$:

$$([Me_1]^{j-1} - (1-x) \cdot \frac{\Delta[N]^j}{n'})^{1-x} \cdot ([Me_2]^{j-1} - x \cdot \frac{\Delta[N]^j}{n'})^x \cdot ([N]^{j-1} - \Delta[N]^j) = K_{Me_{1,\,1-x}Me_{2,\,x}N_n} \quad (j \geq 1) \qquad (4.8b)$$

with $[Me_i]^{j-1}$ and $[N]^{j-1}$ as the amounts of dissolved Me_i and N after time step $j-1$ and $\Delta[N]^j$ as the amount of nitrogen taken up in $Me_iN_{n'}$ or $(Me_{1,\,1-x}Me_{2,\,x})N_{n'}$ in time step j.

The nitrogen concentration can be calculated as function of depth and time applying a numerical finite-difference (explicit) solution method for Eq. (4.3) as described in [15, 38-40]. Upon executing this recursive method, at every depth for every time step, the possible precipitation of alloying element nitrides is verified and executed as described above.

The nitrogen-concentration depth profile can thus be numerically calculated on the basis of Eqs. (4.3), (4.7) and (4.8) adopting values for the following three (four) parameters:

- the amount of mobile nitrogen dissolved in the ferrite matrix at the surface of the specimen, in equilibrium with the nitriding gas atmosphere: $c_{N_\alpha}^s = [N]_\alpha^0 + [N]_{mob,\,exc}^0$;

- the solubility products, $K_{Me_i N_n}$, or the solubility product $K_{Me_{1,\,1-x} Me_{2,\,x} N_n}$;

- the composition parameter: $n' = n + y$ (here with $n = 1$)

4.3 Experimental procedures

4.3.1 Specimen preparation

Ingots of Fe-2at.%Cr-2at.%Ti were prepared from pure Fe (99.98 wt.%, Alfa Aesar), pure Cr (99.999 wt.%, Alfa Aesar) and pure Ti (99.999 wt.%, Alfa Aesar) using a light-arc furnace. The molten alloys were cast as buttons, with a shape given by a diameter of 40 mm and a height of 15 mm. The precise composition of the Fe-Ti-Cr alloys was analyzed, applying (i) inductive coupled plasma-optic emission spectroscopy (ICP-OES) to determine the content of the alloying elements Ti and Cr, (ii) a combustion method to determine the light elements C and S and (iii) a hot-extraction to determine the light elements O and N. The thus determined composition of the alloys is shown in Table 4.1.

Table 4.1: The contents of Cr, Ti and light element impurities in the alloy specimens before nitriding.

element / alloy	Cr	Ti	N	O	S	C
	(at.%)		(µg/g)			
Fe-2at.%Cr-2at.%Ti	2.07 ± 0.01	2.00 ± 0.02	< 10	11 ± 3	< 10	10 ± 2

The cast buttons were cold-rolled to foils with a thickness of about 1.0 mm. In order to reduce the rolling induced texture of the specimen, the buttons were rolled in different directions. The foils thus obtained were cut into rectangular specimens (15 × 15 mm^2) and subsequently ground and polished (final stage: 1 µm diamond paste). The polished specimens were encapsulated in a quartz tube filled with Ar and annealed at 800°C for 2h to establish a recrystallized grain structure (grain size of about 40 µm). Before nitriding the specimens were ground and polished (last step: 1 µm diamond paste) and cleaned ultrasonically with ethanol.

4.3.2 Nitriding

For nitriding the specimen were suspended at a quartz fiber and placed in the middle of a vertical tube furnace. The gaseous nitriding experiments were performed in a flux of an ammonia/hydrogen gas mixture (NH$_3$: >99.998 vol% and H$_2$: 99.999 vol%). The fluxes of both gases were precisely adjusted with mass flow controllers. The gas flow rate was kept at 500 ml/min, which, because the inner diameter of the tube furnace is 28 mm, corresponds to a linear gas velocity at room temperature of 13.5 mm/s in the furnace, which is sufficient to avoid any significant (thermal) decomposition of ammonia in the nitriding atmosphere [41, 42].

Different sets of nitriding experiments were performed: at temperatures 560°C and 580°C and at nitriding potentials r_N = 0.004 atm$^{-1/2}$ and 0.054 atm$^{-1/2}$ ($r_N \equiv p_{NH_3} / p_{H_2}^{3/2}$, with p_i as partial pressure of component i [41]), with varying the nitriding time in the range 1-24h. The different nitriding conditions have been gathered in Table 4.2. Under the applied nitriding conditions no compound layer (iron nitrides: ε-Fe$_{2-3}$N and γ'-Fe$_4$N) formation occurred at the specimen surface. In the following the different sets of nitriding conditions applied to the Fe-2at.%Cr-2at.%Ti specimens, (i) at

560°C with $r_N = 0.054$ atm$^{-1/2}$, (ii) at 560°C with $r_N = 0.004$ atm$^{-1/2}$ and (iii) at 580°C with $r_N = 0.004$ atm$^{-1/2}$, will be denoted as LTHP, LTLP and HTLP, respectively (where L and H stand for "relatively low" and "relatively high", respectively, and T and P denote nitriding temperature and nitriding potential, respectively).

Table 4.2: Summary of applied nitriding parameters for the Fe-2at.%Cr-2at.%Ti alloy.

alloy	temp. (°C)	NH$_3$ (ml/min)	H$_2$ (ml/min)	r_N (atm$^{-1/2}$)	time (h)	specimen code
Fe-2at%Cr-2at.%Ti	560	25	475	0.054	1, 3, 12, 20, 24	LTHP
	560	2	498	0.004	6, 12, 24	LTLP
	580	2	498	0.004	6, 12, 18, 24	HTLP

4.3.3 EPMA analysis

The homogeneity of the distribution of the alloying elements Ti and Cr and of nitrogen in the specimens was verified by electron probe microanalysis (EPMA) using a Cameca SX100 instrument. Pieces of the specimen were cut to prepare cross-sections by subsequently embedding of these pieces with a Polyfast (Struers; a conductive bakelite resin with carbon filler embedding material), followed by grinding and polishing (last step: 1 µm diamond paste). A focused electron beam at an accelerating voltage of 15 kV and a current of 100 nA was applied. To obtain the element contents as function of depth in the specimens, the intensities of the characteristic Ti-K$_\alpha$, Cr-K$_\alpha$, Fe-K$_\beta$ and N-K$_\alpha$ X-ray emission peaks were determined at points separated at distances of 2 µm along lines perpendicular to the surface of the specimen in the specimen cross section. The concentrations of Ti, Cr and Fe were determined on the basis of the ratio of the concerned characteristic X-ray emission peak intensity of the specimen and that of a corresponding standard specimen (i.e. pure Ti, pure Cr and pure Fe) by applying the $\Phi(\rho z)$-correction [43].

For the determination of the characteristic X-ray emission peak of nitrogen a correction procedure had to be applied, because of severe overlap of the $N-K_{\alpha}$ and $Ti-L_l$ X-ray emission peaks. The correction procedure known as *ratio method* [44] was applied.

4.3.4 Transmission electron microscopy

Specimens for transmission electron microscopy (TEM) were prepared from a depth 60 - 70 μm below the specimen surface in the nitrided zone as follows.

Discs ($\Phi = 3$ mm) were stamped with a mechanical punch from sheets produced by removing material mechanically from both sides (faces) of a nitrided specimen. These discs were thinned, to obtain an electron-transparent area, applying the jet-electropolishing technique employing a Struers Tenupol-3 apparatus (bath composition: 85 vol.% acetic acid and 15 vol.% perchloric acid, current: 24 mA $\leq I \leq$ 42 mA, voltage: 19.5V, temperature: 5°C, flow rate setting: "20", and treatment time: 174s $\leq$ t $\leq$ 242s) and subsequently rinsed in ethanol, acetone and isopropanol. To generate a hole in the middle of the sample, the discs were fixed during the jet-electropolishing treatment between two platinum rings.

TEM analysis was performed using a Philips CM 200 transmission electron microscope operated at 200 kV. Bright field (BF), dark field (DF) images and selected area diffraction patterns (SADPs) were taken employing a Gatan CCD camera.

4.4 Results and evaluation

4.4.1 Nitrogen-concentration depth profiles

The nitrogen-concentration depth profiles of the Fe-2at.%Cr-2at.%Ti specimens nitrided for LTHP, LTLP and HTLP are presented in Figs 4.1a-c, respectively. An almost constant nitrogen level in the nitrided zone is obtained for all specimens, except for the cases of relatively short nitriding time of low nitriding temperature, where in particular the nitrogen concentration at the surface has not reached the "saturation" value observed upon prolonged nitriding. This can be ascribed to the finite time needed to establish (near) local equilibrium (or a stationary state) at the specimen surface with the gas atmosphere (see further discussion in section 4.5).

The dashed line in Fig. 4.1 denotes the normal nitrogen content, $[N]_{nor} = [N]_{MeN_n} + [N]_\alpha^0$. It follows that, a large amount of excess nitrogen (the difference of $[N]_{tot}$ and $[N]_{nor}$) has been taken up (cf. section 4.2.1).

Evidently, the higher the nitriding potential (at the same nitriding temperature and for the same nitriding time), the larger the amount of (dissolved) nitrogen (including mobile excess nitrogen) and the larger the extent of the nitrided zone.
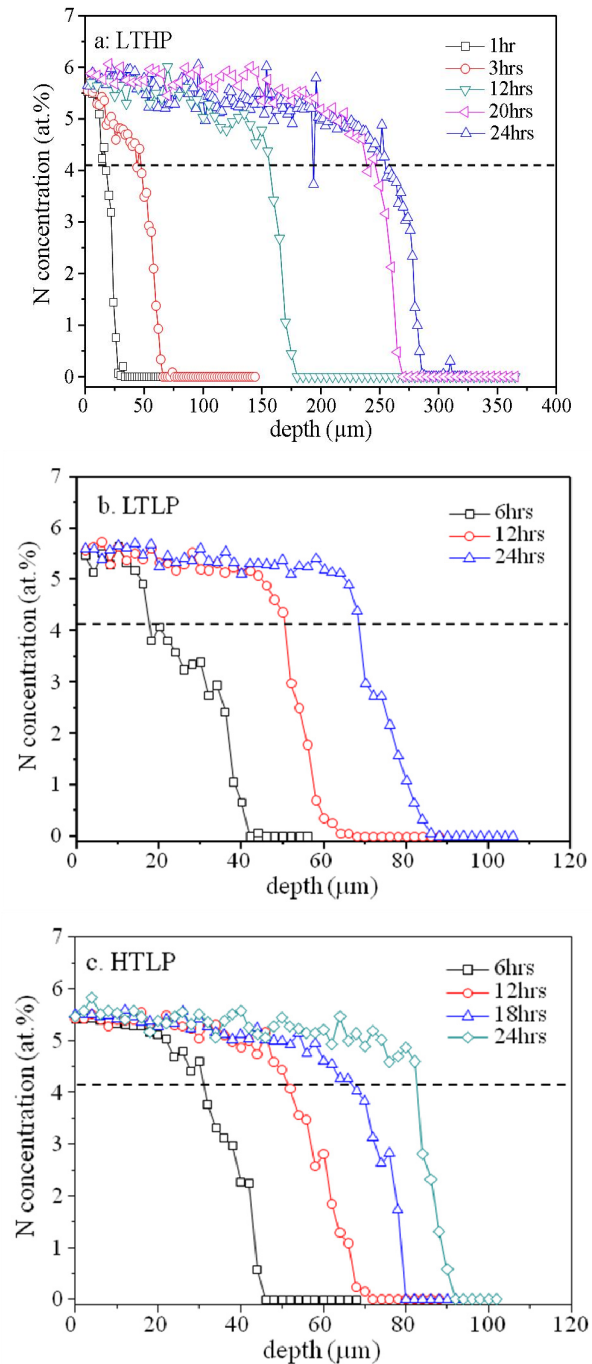
Fig. 4.1: Nitrogen-concentration depth profiles of Fe-2at.%Cr-2at.%Ti alloy specimens (a) LTHP, (b) LTLP and (c) HTLP, nitrided for various times. The dashed line indicates the so-called "normal nitrogen" content which is sum of the nitrogen incorporated in the stoichiometric nitrides and the equilibrium solubility of nitrogen in pure, unstrained ferrite matrix (see text).

4.4.2 Microstructural analysis

TEM bright field (BF, top) and dark field (DF, middle) images and corresponding selected area diffraction patterns (SADPs, insets) of nitrided Fe-2at.%Cr-2at.%Ti alloy specimens (LTLP and HTLP) are shown in Figs. 4.2a and b. The electron-beam direction in both SADPs is close to (i.e. does not coincide exactly with) the [001] zone axis of the ferrite, in order to avoid strong diffraction by the matrix and to reveal the presence of the precipitates by their diffraction contrast.

In particular for the LTLP specimen (Fig. 4.2a) extremely fine nitride precipitates of hardly resolvable morphology can be discerned. In case of the HTLP specimen (Fig. 4.2b) a relatively clear platelet-type morphology (length $\leq$ 20 nm and thickness $\leq$ 2 nm) of the nitride precipitates is observed. It follows that the size of the nitride platelets increases (and the density of platelets decreases) with increasing nitriding temperature at constant nitriding potential.

The selected area diffraction patterns (SADPs) recorded from all specimens show diffraction spots at locations corresponding to the ferrite matrix (see the schematic diffraction patterns shown at the bottom in Fig. 4.2). Additionally, streaks through the 200 and 020 type diffraction spots of the ferrite matrix can be observed. Further, at higher nitriding temperature, intensity maxima on these streaks occur, at positions expected for 002 type spots of a cubic, rock-salt crystal-structure type nitride precipitate (see inset of Fig. 4.2b).
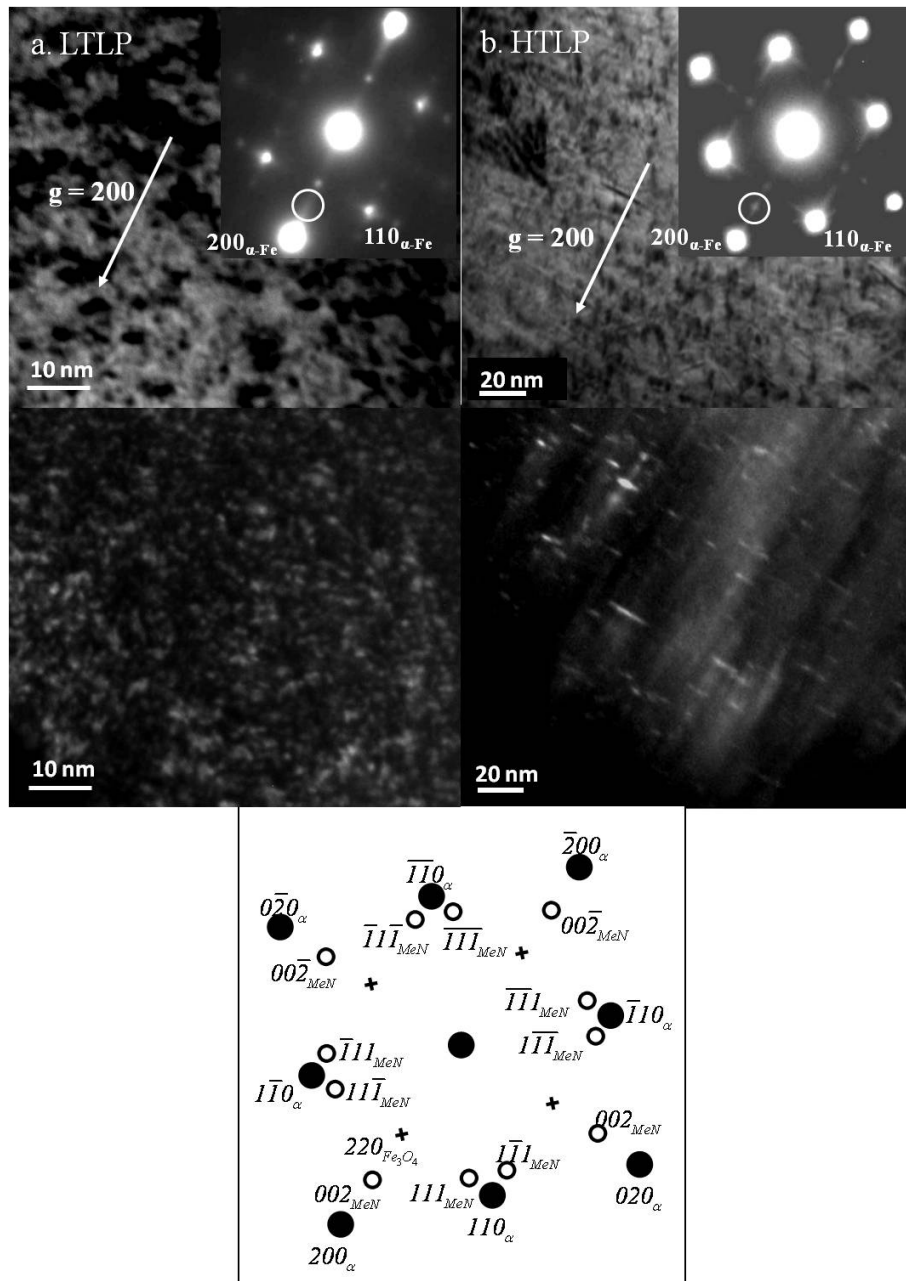
Fig. 4.2: TEM BF images (top), corresponding SADPs (insets), DF images (middle; as obtained from the streak and/or intensity maximum area selected by positioning the objective lens aperture at the position indicated by the open circle in the SADPs) and schematic diffraction pattern (bottom), corresponding with both SADPs shown, for the concerned electron-beam, $[001]_{\alpha\text{-Fe}}$ direction and nitride precipitates complying with a Bain orientation relationship with the α-Fe matrix (black dots: diffraction spots of the ferrite matrix; unfilled circles: diffraction spots of the nitride precipitates). Fe-2at.%Cr-2at.%Ti alloys nitrided for 24h with nitriding potential, $r_N = 0.004$ atm$^{-1/2}$ (TEM specimens are obtained about $60 - 70$ μm below the specimen surface) for (a) LTLP and (b) HTLP.

The $200_{\alpha\text{-Fe}}$ diffraction spots in Fig. 4.2a have split into two: one can be ascribed to cubic ferrite and the other one to tetragonally distorted ferrite. The tetragonal distortion is a consequence of the development of misfit strain between nitride precipitates and ferrite matrix. Similar observations have been made for nitrided binary Fe-V [45] where nitrides of rock-salt crystal-structure type precipitate as platelets with $\{001\}_{\alpha\text{-Fe}}$ lattice planes as habit planes. The mismatch of the nitride platelets with the ferrite matrix is such that, in order to maintain coherency, the ferrite matrix in the immediate surroundings of the nitride platelets is anisotropically, tetragonally deformed: A compressive misfit stress develops in directions normal to the platelet (i.e. in a $<001>_{\alpha\text{-Fe}}$ direction), whereas a tensile misfit stress develops parallel to the platelet faces (i.e. in $<100/010>_{\alpha\text{-Fe}}$ directions). The surrounding ferrite matrix of the nitride platelet can thus be considered as a bct phase [33, 45].

If precipitates of CrN and TiN would have developed separately in the ferrite matrix during nitriding, the diffraction spots of both nitrides should be distinguishable (in the SADPs). However, the SADPs show only singular 111 reflections of a cubic, rock-salt crystal-structure type MeN nitride (note that the possible 002 spots lie on a streak (see above) and cannot be distinguished, if separate spots would occur). This strongly suggests that Ti and Cr have precipitated together as a cubic, rock-salt type mixed $Cr_{1-x}Ti_xN$ nitride (for extensive discussion of electron diffraction patterns recorded from nitrided alloys as investigated here, see Ref. 33).

4.4.3 Numerical modeling of nitrogen-concentration depth profiles

Numerically calculated nitrogen-concentration depth profiles, as described in section 4.2.2, were fitted to experimental data obtained by EPMA. The diffusion coefficient of nitrogen in the ferrite matrix, D_N is adopted as 8.7 μm^2/s and 11.3 μm^2/s at 560°C and

580°C, respectively [46]. The fitting parameters are (i) the solubility products, $K_{Me_i N_n}$ or the solubility product, $K_{Me_{1, 1-x} Me_{2, x} N_n}$, (ii) the composition parameter, $n' = n + y$ and (iii) the surface nitrogen concentration, $c_{N_\alpha}^s$ (cf. section 4.2).

A two-step fitting procedure for each of the two possible types of precipitation (separate nitrides or mixed nitride) has been applied:

For the precipitation of (two) separate nitrides, initial values of K_{CrN} and K_{TiN} have been adopted from Ref. 35. After fitting of the nitrogen-concentration depth profiles for all times at constant temperature separately, average values for K_{CrN} and K_{TiN} were obtained as (i) at 560°C, K_{CrN} = 0.03 (atoms)^{2}nm^{-6} and K_{TiN} = 0.29 × 10^{-15} (atoms)^{2}nm^{-6} and (ii) at 580°C, K_{CrN} = 0.05 (atoms)^{2}nm^{-6} and K_{TiN} = 0.94 × 10^{-15} (atoms)^{2}nm^{-6}, respectively. Note that, at constant temperature, the solubility products should not depend on nitriding potential and nitriding time. Further, the composition parameters, n'_{CrN} or n'_{TiN} should also be independent of nitriding time, but they may depend on nitriding temperature and nitriding potential. From previous studies on nitrided iron-based binary Fe-Cr [15, 34] and Fe-Ti [47, 48] alloys it follows that the amount of nitrogen adsorbed at the interface between the coherent CrN platelets and the ferrite matrix is very small as compared to that of TiN in the ferrite matrix (i.e. $[N]_{imm, exc}^{CrN} < [N]_{imm, exc}^{TiN}$). Therefore, it can be assumed that the total amount of adsorbed nitrogen at the nitride platelet faces of the present nitrided Fe-Cr-Ti alloy, is largely determined by n'_{TiN}. Therefore, in the fit procedure adopted here the composition parameter of CrN, n'_{CrN}, was not considered as a fit parameter; its value was set equal to that determined in Ref. 15: n'_{CrN} = 1.12. Thus, the above mentioned values of K_{CrN},

K_{TiN} and n'_{CrN} were used as constants in the second, definitive fitting, where only $c^s_{N_\alpha}$ and n'_{TiN} were considered as fit parameters.

For the precipitation of the mixed $Cr_{1-x}Ti_xN$ nitride, the nitrogen-concentration depth profiles have been first fitted individually at each temperature (with $n'_{Cr_{1-x}Ti_xN}$, $c^s_{N_\alpha}$ and $K_{Cr_xTi_{1-x}N}$ as fit parameters). The averages of thus determined values of $K_{Cr_xTi_{1-x}N}$ are $K_{Cr_xTi_{1-x}N} = 0.68 \times 10^{-3}$ (atoms)^{2}nm^{-6} and 1.10×10^{-3} (atoms)^{2}nm^{-6} at 560°C and 580°C, respectively. These values have then been used as constants in the second, definitive fitting where only $c^s_{N_\alpha}$ and $n'_{Cr_{1-x}Ti_xN}$ were considered as fit parameters.

Firstly, the case of separate precipitation of CrN and TiN is considered. Using the procedure described above, the accordingly obtained best fit results for the measured nitrogen concentration-depth profiles of the LTHP specimens nitrided for 12h and 20h are shown in Figs. 4.3a and 4.3b, respectively.
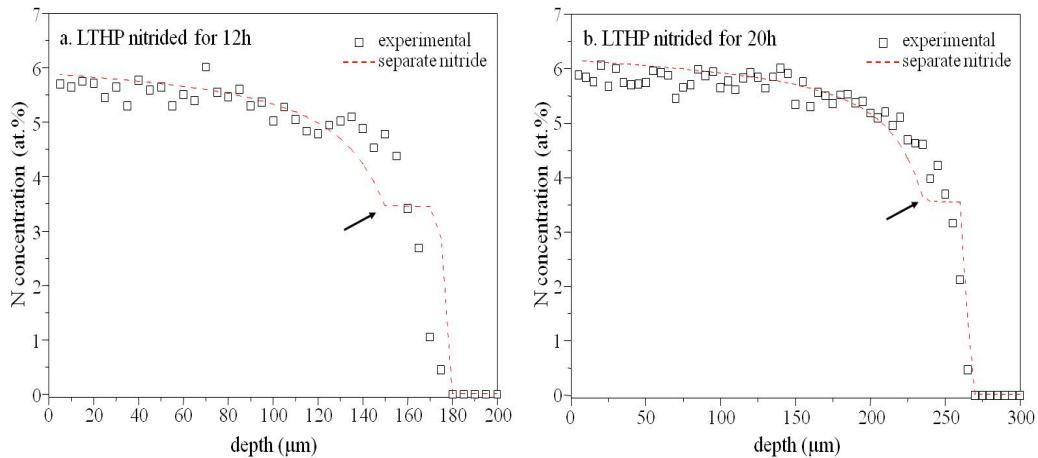

Fig. 4.3: Nitrogen-concentration depth profiles determined by EPMA measurement (data points) and as determined by fitting to these data of the numerical kinetic model (dashed lines) for the case of precipitation of separate nitrides (TiN and CrN) for the LTHP specimens nitrided for (a) 12h and (b) 20h.

A clear plateau region (denoted by arrows in Fig. 4.3) can be discerned in the calculated nitrogen-depth profiles (dashed lines). This can be interpreted as a direct consequence of a very low value of K_{TiN} as compared the value of K_{CrN} (see above): upon arrival of dissolved nitrogen by diffusion, at a certain depth, it is consumed immediately by Ti to precipitate as TiN until total local depletion of Ti has been realized. Only thereafter the still dissolved Cr can precipitate upon continued inward diffusion of nitrogen. As a consequence, only TiN precipitates develop at the nitriding front (i.e. the plateau region), whereas CrN precipitates develop in the zone closer to the surface where precipitation of TiN has been completed practically. Clearly, plateau regions in the nitrided zone adjacent to the case/core boundary do not occur in the experimental nitrogen-concentration depth profiles. It is concluded that separate precipitation of CrN and TiN is incompatible with the experimental data.

Secondly, the case of precipitation of a mixed nitrided, $Cr_{1-x}Ti_xN$ is considered. Using the corresponding fit procedure described above, the obtained best fit results for all specimens are shown in Fig. 4.4 together with the experimental data. The fitted and experimental nitrogen concentration-depth profiles agree fairly well. The values obtained for the fit parameters; surface nitrogen concentration, $c_{N_\alpha}^s$, solubility product, $K_{Cr_xTi_{1-x}N}$ and the composition parameter, $n'_{Cr_{1-x}Ti_xN}$ have been gathered in Table 4.3. The dependence of $c_{N_\alpha}^s$ as function of nitriding time is shown in Fig. 4.5, at constant temperature and at constant nitriding potential.
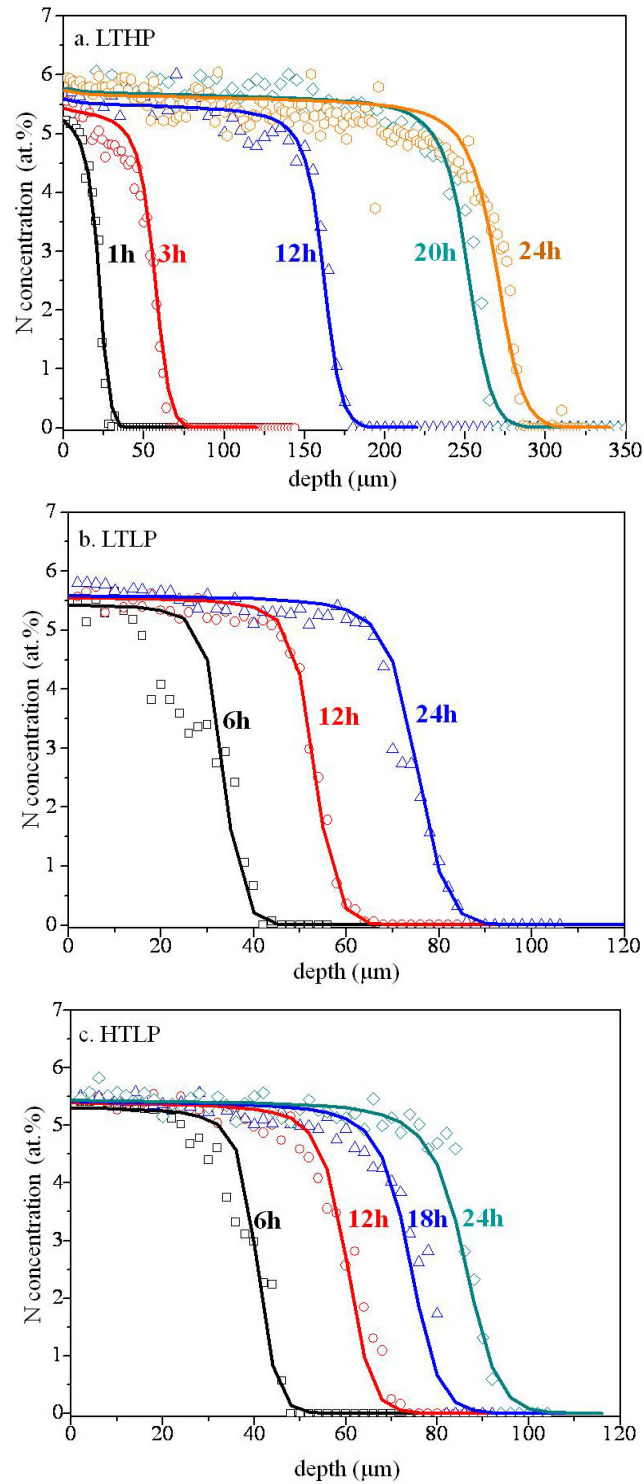
Fig. 4.4: Nitrogen-concentration depth profiles determined by EPMA measurement (data points) and as determined by fitting of the numerical kinetic model for the case of mixed $Cr_{1-x}Ti_xN$ nitride precipitation. (a) LTHP, (b) LTLP and (c) HTLP. The values obtained for the fit parameters have been gathered in Table 4.3.

Table 4.3: Values obtained for the fit parameters: $K_{Cr_xTi_{1-x}N}$, $c_{N_\alpha}^s$ and $n'_{Cr_{1-x}Ti_xN}$.

nitriding time (h) / specimen		1	3	6	12	18	20	24
LTHP	$K_{Cr_xTi_{1-x}N}$ ((atoms)^{2}nm^{-6})	0.68×10^{-3}						
	$c_{N_\alpha}^s$ (at.%)	0.021	0.045	·	0.128	·	0.141	0.140
	$n'_{Cr_{1-x}Ti_xN}$	1.57	1.56	·	1.59	·	1.62	1.62
LTLP	$K_{Cr_xTi_{1-x}N}$ ((atoms)^{2}nm^{-6})	0.68×10^{-3}						
	$c_{N_\alpha}^s$ (at.%)	·	·	0.008	0.011	·	·	0.011
	$n'_{Cr_{1-x}Ti_xN}$	·	·	1.57	1.60	·	·	1.61
HTLP	$K_{Cr_xTi_{1-x}N}$ ((atoms)^{2}nm^{-6})	1.10×10^{-3}						
	$c_{N_\alpha}^s$ (at.%)	·	·	0.014	0.016	0.016	·	0.016
	$n'_{Cr_{1-x}Ti_xN}$	·	·	1.53	1.55	1.56	·	1.56
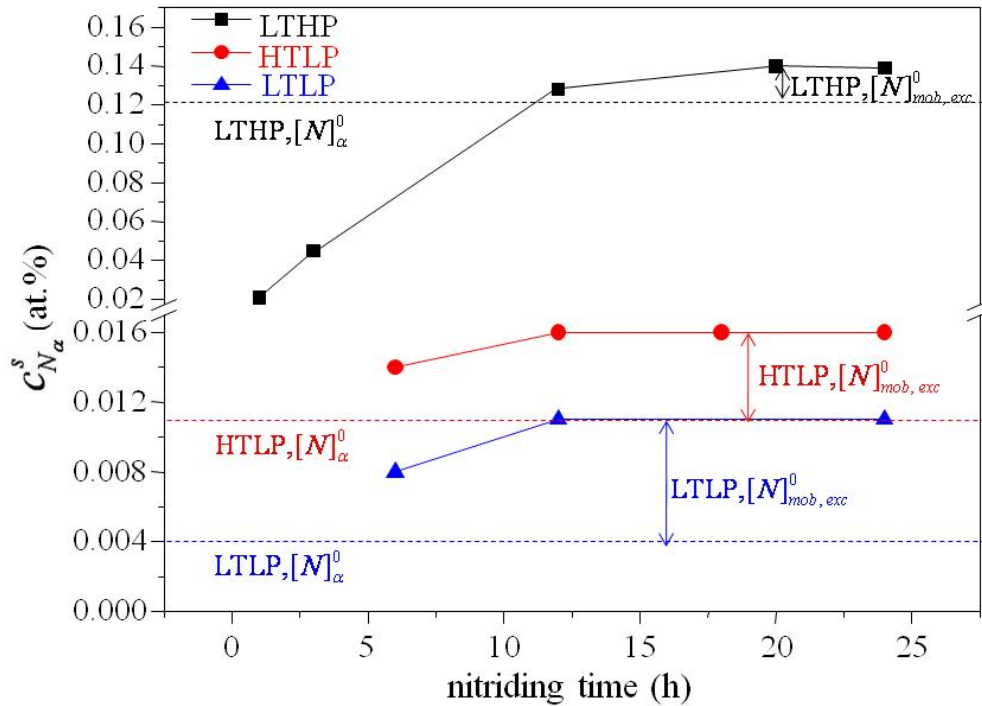
Fig. 4.5: The concentration of dissolved nitrogen at the surface of the specimen, $c_{N_\alpha}^s$, as function of nitriding time. Results of fitting of the numerical kinetic model for the case of mixed $Cr_{1-x}Ti_xN$ nitride precipitation (dashed lines indicate the equilibrium solubility of nitrogen in a pure, unstrained ferrite matrix, $[N]_\alpha^0$) for LTHP, LTLP and HTLP specimens. The difference between $c_{N_\alpha}^s$ and $[N]_\alpha^0$ equals $[N]_{mob,exc}^0$.

The experimentally determined values for $[N]_{tot}$ have an inaccuracy leading to their presentation in at% with only one decimal (see the EPMA data in Table 4.4). The fitting of the nitrogen-concentration depth profiles is highly sensitive to the values of $c_{N_\alpha}^s$: for example, the extent of the diffusion zone for a specimen nitrided under LTLP conditions increases about 8 μm by an increase of $c_{N_\alpha}^s$ of only 0.002 at.% N (see Fig. 4.6). Therefore the results in at.% for $c_{N_\alpha}^s$ and $[N]_{mob, exc}^0$ have been given with three decimals in Table 4.3 and 4.4.

Table 4.4: The total amount of nitrogen at the specimen surface determined by EPMA, $[N]_{tot, EPMA}^0$ (taken as the average value of five data points near the surface), and the amounts $[N]_{tot, cal}^0$, $[N]_{mob, exc}^0$ and $[N]_{imm, exc}^0$ at the specimen surface as derived from the fitted kinetic model for 24h nitrided LTHP, LTLP and HTLP specimens.

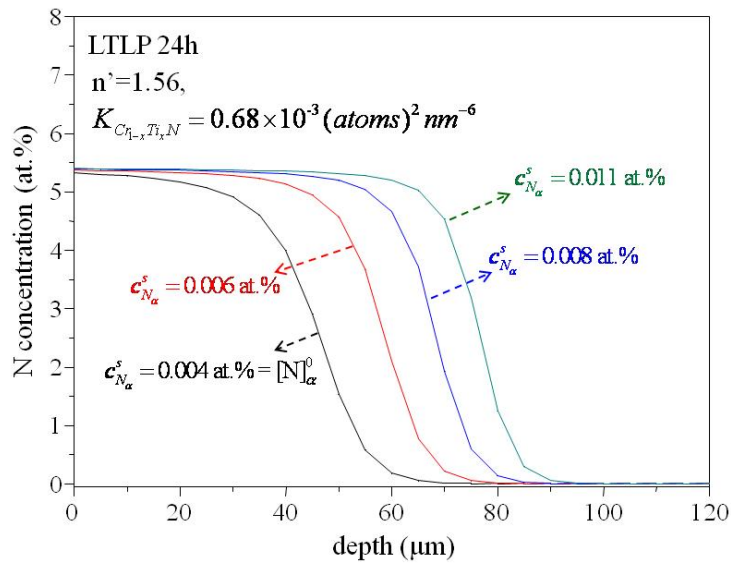| specimen	$[N]_{tot, EPMA}^0$ (at.%)	$[N]_{tot, cal}^0$ (at.%)	$[N]_{mob, exc}^0$ (at.%)	$[N]_{imm, exc}^0$ (at.%)
LTHP	5.9 ± 0.1	6.09	0.019	2.16
LTLP	5.8 ± 0.1	6.06	0.007	2.14
HTLP	5.6 ± 0.2	5.89	0.005	1.97

Fig. 4.6: Calculated nitrogen-concentration depth profiles for a LTLP specimen as function of $c_{N_\alpha}^s$. A slight change of $c_{N_\alpha}^s$ (0.002 at.%) results in a significant nitrided depth difference (about 8 μm), which is experimentally well discernable.

4.5 General discussion

During nitriding of ferritic Fe-2at.%Cr-2at.%Ti alloys cubic, rock-salt crystal-structure type mixed $Cr_{1-x}Ti_xN$ nitride platelets precipitate (section 4.4.2). There appears to be even less obstacle for the formation of a mixed nitride in the case of nitriding Fe-Cr-Ti alloy than in the case of nitriding Fe-Cr-Al alloy [31]: both CrN [49] and TiN [50] have a cubic, rock-salt type equilibrium crystal structure, whereas, AlN has an hexagonal, wurtzite-type equilibrium crystal structure [20-23]. Further, uptake of Cr in TiN can be favoured because it leads to reduction of the misfit strain with the surrounding ferrite matrix [33].

The surface concentration of dissolved nitrogen, $c_{N_\alpha}^s$, increases with nitriding time until a saturation level has been reached (Fig. 4.5). The initial increase of $c_{N_\alpha}^s$ is a consequence of the finite period of time necessary to establish local equilibrium (or a stationary state), at the specimen surface, of the gas atmosphere with the solid substrate. This phenomenon has been observed for the nitriding of pure iron and is due to the competition of reactions of finite rate at the specimen surface, such as the dissociation of NH_3, the association of N atoms adsorbed at the specimen surface and their subsequent desorption as N_2 gas, and the diffusion of initially adsorbed and then dissolved nitrogen into the specimen; occurrence of local equilibrium (instead of a stationary state) at the surface requires that the desorption rate of nitrogen gas, formed by association of nitrogen atoms adsorbed at the surface, can be neglected [42, 51, 52]. The effect can be particularly relatively strong in the presence of alloying elements which form nitrides, because much more nitrogen has to be taken up before saturation, at the surface, has been attained. Note that at the shortest applied nitriding times the values of $c_{N_\alpha}^s$ are even smaller than the equilibrium solubility of nitrogen in pure, unstrained ferrite (cf. dashed horizontal lines in

Fig. 4.5, which have been calculated according to Ref. 42). After saturation, the amount of dissolved nitrogen at the surface has surpassed the equilibrium solubility in pure, unstrained ferrite, indicating the presence of mobile (i.e. dissolved) excess nitrogen. The values of $[N]^0_{mob, exc}$ can be calculated as $[N]^0_{mob, exc} = c^s_{N_\alpha} - [N]^0_\alpha$ (cf. Eq. (4.2)).

The presence of dissolved excess nitrogen in the ferrite matrix upon nitriding of Fe-Cr-Ti alloys is a consequence of elastic accommodation of the misfit between nitride platelet and ferrite matrix: such elastic accommodation of misfit induces a tensile hydrostatic stress component in the ferrite matrix [53]. As a consequence, as compared to unstrained ferrite, more nitrogen can be dissolved (on octahedral interstices) in the ferrite matrix. The amount of dissolved nitrogen and thus also $[N]^0_{mob, exc}$ in the ferrite matrix depends linearly on the nitriding potential [53]. Indeed, $[N]^0_{mob, exc}$ (LTHP) / $[N]^0_{mob, exc}$ (LTLP) = 13.1, which compares very well with r_N (LTHP) / r_N (LTLP) = 13.1. The size of the nitride precipitates increases with increasing nitriding temperature (cf. results shown in section 4.4.2). In general, upon coarsening less misfit strain is accommodated elastically (beginning coherent → incoherent transition). As a consequence, the amount of $[N]^0_{mob, exc}$ decreases with increasing temperature, as observed (cf. results for LTLP and HTLP in Fig. 4.5).

The largely coherent nature of the nitride platelet/matrix interface makes adsorption of nitrogen at the octahedral interstices in the ferrite matrix *adjacent to* the platelet faces likely [53], as in this way chemical bonding to Cr and/or Ti atoms in the platelet is realized (albeit this chemical bonding is of lesser strength than for the nitrogen atoms within the nitride platelets). The presence of such immobile excess nitrogen (cf. section 4.2.1) is revealed by the values obtained for the nitride composition parameter, $n'_{Cr_{1-x}Ti_xN}$ which are distinctly larger than one (cf. Table 4.3). The amount of immobile

excess nitrogen in the surface region (i.e. for a fully precipitated stage and where equilibrium with the gas atmosphere has been realized), $[N]^0_{imm,\,exc}$, can be deduced straightforwardly from the value of the composition parameter, $n'_{Cr_{1-x}Ti_xN}$ and the amounts of alloying elements (cf. Table 4.4). Evidently, for the present nitriding conditions, $[N]^0_{imm,\,exc} >> [N]^0_{mob,\,exc}$.

It should be recognized that, although the amounts of mobile excess nitrogen are rather small, as compared to the amounts of immobile excess nitrogen, yet these small amounts of mobile excess nitrogen have great influence on the nitriding kinetics: the extent of the diffusion zone is significantly enhanced by these small amounts of nitride excess nitrogen (see Fig. 4.6). Indeed, $[N]^0_{mob,\,exc}$ is not small compared to $[N]^0_\alpha$ (cf. Fig. 4.5).

As compared to the LTLP results, the somewhat lower amount of $[N]^0_{imm,\,exc}$ of HTLP (cf. Table 4.4) is compatible with the larger platelet thickness, and thus lesser amount of nitride/matrix interface, as observed by TEM (cf. section 4.4.2). Accordingly, the thickness of the precipitates can be estimated by using the following equation [30];

$$thickness = \frac{2}{(n'_{Cr_{1-x}Ti_xN}-1)} \cdot \frac{a_{Cr_{1-x}Ti_xN}}{2} \qquad (4.9)$$

where $a_{Cr_{1-x}Ti_xN}$ denotes the lattice parameter of the mixed nitride. Assuming that the lattice parameter of the mixed $Cr_{1-x}Ti_xN$ nitride complies with Vegard's law and using literature values for the lattice parameters of CrN and TiN (0.414 nm for rock-salt crystal-structure type CrN [49] and 0.424 nm for rock-salt crystal-structure type TiN [50]) the lattice parameter of mixed $Cr_{1-x}Ti_xN$ nitride with x = 0.49, equals $a_{Cr_{1-x}Ti_xN} =$ 0.419 nm. Using this value of the lattice parameter and the experimental values of

$n'_{Cr_{1-x}Ti_xN}$ (1.62, 1.61 and 1.56 for LTHP, LTLP and HTLP, respectively), the thickness of the nitride platelet is obtained as 0.68, 0.69 and 0.75 nm for LTHP, LTLP, and HTLP, respectively. The larger value for the nitride platelet thickness of the HTLP specimens is compatible with the TEM analysis presented in section 4.4.2.

4.6 Conclusions

1. Upon nitriding of ternary iron-based ferritic Fe-Cr-Ti alloys highly coherent cubic, rock-salt crystal-structure type, mixed $Cr_{1-x}Ti_xN$ nitrides develop as platelets (thickness < 2 nm) in the ferrite matrix obeying a Bain orientation relationship with the ferrite matrix with $\{100\}_{\alpha\text{-Fe}}$ habit planes. The platelets are surrounded by a tetragonally distorted ferrite matrix.

2. A numerical model developed for describing the nitriding kinetics of ternary iron-based $Fe\text{-}Me_1\text{-}Me_2$ alloys leads to agreement with the experimentally determined nitrogen-concentration depth profiles provided the separate roles of mobile excess nitrogen (dissolved in the ferrite matrix) and immobile excess nitrogen (adsorbed at the nitride-platelet/matrix interface) are recognized. The results obtained are compatible with the precipitation of mixed $Cr_{1-x}Ti_xN$ nitride, and not of separate CrN and TiN nitrides, in agreement with the TEM data.

3. The surface concentration of dissolved nitrogen increases with nitriding time until a saturation level is attained, as a consequence of the strong affinity of, in particular, Ti for N, the finite diffusion rate of dissolved nitrogen and the finite rate of ammonia dissociation at the surface.

4. For a given degree of nitride-platelet/matrix coherency, the amount of mobile excess nitrogen is primarily dependent on the nitriding potential, whereas the amount of immobile excess nitrogen is primarily dependent on the size of the precipitates (i.e. the interface density).

5. The amount of immobile (adsorbed) excess nitrogen is very much larger than the amount of mobile (dissolved) excess nitrogen. Yet, the relatively tiny amount of mobile excess nitrogen is responsible for a district increase of the depth of the nitrided zone. The immobile excess nitrogen enhances appreciably the nitrogen level of the nitrided zone.

Acknowledgements

References

[1] S. Lampman, Introduction to surface hardening of steel ASM Handbook, vol. 4, Heat Treating, ASM International, Metals Park, Ohio, 1991.

[2] H. Ferkel, M. Glatzer, Y. Estrin, R.Z. Valiev, C. Blawert and B.L. Mordike, Mat. Sci. Eng. A 348 (2003) 100.

[3] M. Pellizzari, A. Molinari and G. Straffelini, Mat. Sci. Eng. A 352 (2003) 186.

[4] N. Limodin and Y. Verreman, Mat. Sci. Eng. A 435-436 (2006) 460.

[5] A. Basu, J. Dutta Majumdar, S. Ghosh Chowdhury, P.K. Ajikumar, P. Shankar, A.K. Tyagi, Baldev Raj and I. Manna, Surf. Coat. Technol. 201 (2007) 6985.

[6] T. Hirsch, T.G.R. Clarke and A. da Silva Rocha, Surf. Coat. Technol. 201 (2007) 6380.

[7] S. Jegou, L. Barrallier and R. Kubler, Acta Mater. 58 (2010) 2666.

[8] G. Miyamoto, A. Yonemoto, Y. Tanaka, T. Furuhara and T. Maki, Acta Mater. 54 (2006) 4771.

[9] G. Miyamoto, A. Yonemoto, Y. Tanaka, T. Maki and T. Furuhara, ISIJ International 49 (2009) 1796.

[10] B. Mortimer, P. Grieveson and K.H. Jack, Scand. J. Metals 1 (1972) 203.

[11] K.H. Jack, Proc. Heat Treatment Conf. London 1973, The Metals Society, London (1975) 39.

[12] B.J. Lightfoot and D.H. Jack, Proc. Heat Treatment Conf. London 1973, The Metals Society, London (1975) 59.

[13] R.E.E. Pulkkinen, Scan. J. Metall. 12 (1983) 87.

[14] R.E. Schacherl, P.C.J. Graat and E.J. Mittemeijer, Z. Metallkd. 93 (2002) 468.

[15] R.E. Schacherl, P.C.J. Graat and E.J. Mittemeijer, Metall. Mater. Trans. A 35 (2004) 3387.

[16] S.S. Hosmani, R.E. Schacherl and E.J. Mittemeijer, Mater. Sci. Technol. 21 (2005) 113.

[17] S.S. Hosmani, R.E. Schacherl and E.J. Mittemeijer, J. Mater. Sci. 43 (2008) 2618.

[18] S.S. Hosmani, R.E. Schacherl, L.L. Dobrzyńska and E.J. Mittemeijer, Phil. Mag. A 88 (2008) 2411.

[19] H.H. Podgurski, R.A. Oriani and F.N. Davis, Trans. Metall. Soc. AIME 245 (1969) 1603.

[20] H.H. Podgurski and H.E. Knechtel, Trans. Metall. Soc. AIME 245 (1969) 1595.

[21] M.H. Biglari, C.M. Brakman, W.G. Sloof, E.J. Mittemeijer and S. Van Der Zwaag, Z. Metallkd. 84 (1993) 124.

[22] M.H. Biglari, C.M. Brakman, E.J. Mittemeijer and S. Van Der Zwaag, Phil. Mag. A 72 (1995) 1281.

[23] M.H. Biglari, C.M. Brakman, E.J. Mittemeijer and S. Van Der Zwaag, Phil. Mag. A 72 (1995) 931.

[24] H.J. Spies, H. Biermann and A. Fischer, Z. Metallkd. 96 (2005) 781.

[25] W.D. Welch and S.H. Carpenter, Acta Metall. 21 (1973) 1169.

[26] M. Pope, P. Grieveson and K.H. Jack, Scand. J. Metall. 2 (1973) 29.

[27] A.D. Krawitz, Scripta Metall. 11 (1977) 117.

[28] M.M. Yang and A.D. Krawitz, Metall. Trans. A 15 (1984) 1545.

[29] S.S. Hosmani, R.E. Schacherl and E.J. Mittemeijer, Acta Mater. 53 (2005) 2069.

[30] S.S. Hosmani, R.E. Schacherl and E.J. Mittemeijer, Acta Mater. 54 (2006) 2783.

[31] A.R. Clauss, E. Bischoff, R.E. Schacherl and E.J. Mittemeijer, Metall. Mater. Trans. A 40 (2009) 1923.

[32] K.S. Jung, R.E. Schacherl, E. Bischoff and E.J. Mittemeijer, Surf. Coat. Technol. 204 (2010) 1942.

[33] K.S. Jung, R.E. Schacherl, E. Bischoff and E.J. Mittemeijer, HTM J. Heat Treatm. Mat. 65 (2010) 237.

[34] P.M. Hekker, H.C.F. Rozendaal and E.J. Mittemeijer, J. Mater, Sci. 20 (1985) 718.

[35] Y. Sun and T. Bell, Mater. Sci. Eng. 224A (1997) 36.

[36] J.D. Kamminga and G.C.A.M. Janssen, Surf. Coat. Technol. 200 (2005) 909.

[37] J.D. Kamminga and G.C.A.M. Janssen, Surf. Coat. Technol. 200 (2006) 5896.

[38] K. Bongartz, D.F. Lupton and H. Schuster, Metall. Trans. 11A (1980) 1883.

[39] K. Bongartz, W.J. Quadakkers, R. Schulten and H. Nickel, Meall. Trans. 20A (1989) 1021.

[40] J. Crank, The Mathematics of Diffusion, Clarendon Press, Oxford, 1970.

[41] E.J. Mittemeijer and J.T. Slycke, Surf. Eng. 12 (1996) 152.

[42] E.J. Mittemeijer and M.A.J. Somers, Surf. Eng. 13 (1997) 483.

[43] J.L. Pouchou and F. Pichoir, Rech. Aerosp. (1984) 167.

[44] A. Armigliato, L. Dori, A. Garulli and P. Venturi, J. Microsc. Spectrosc. Electron. 7 (1982) 593.

[45] N.E. Vives Diaz, S.S. Hosmani, R.E. Schacherl, E.J. Mittemeijer, Acta Mater. 56 (2008) 4137.

[46] J.D. Fast and M.B. Verrijp, J. Iron Steel Inst. 126 (1954) 24.

[47] D.S. Rickerby, S. Henderson, A. Hendry, K.H. Jack, Acta Metall. 34 (1986) 1687.

[48] D.H. Kirkwood, O.E. Atasoy, S. R. Keown, Metals. Sci. 8 (1974) 49.

[49] M. Nasr Eddine, E.F. Bertaut and M. Maunaye, Acta Crystallogr. B 33 (1977) 2696.

[50] W. Lengauer, S. Binder, K. Aigner, P. Ettmayer, A. Guillou, J. Debuigne and G. Groboth, J. Alloys. Compd. 217 (1995) 137.

[51] H.C.F. Rozendaal, E.J. Mittemeijer, P.F. Colijn and P.J. Van Der Schaaf, Metall.

Trans. 14 (1983) 395.

[52] P.B. Friehling, F.W. Poulsen and M.A.J. Somers, Z. Metallkd. 92 (2001) 589.

[53] M.A.J. Somers, R.M. Lankreijer and E.J. Mittemeijer, Phil. Mag. 59A (1989) 353.

Chapter 5

Summary

5.1 Introduction

Gaseous nitriding is an important thermochemical surface treatment of ferritic steel components to improve technical properties like fatigue, wear and corrosion resistance. It is usually performed in an ammonia/hydrogen gas mixture at temperatures between about 500°C and 580°C (i.e. 773K and 853K) at 1atm which is equivalent to that of thousand atmospheres of pure nitrogen gas.

The ammonia introduced to the nitriding furnace dissociates at the specimen surface and thus released nitrogen atoms can diffuse into the ferrite matrix. Depending on the nitriding conditions (i.e. nitriding temperature, pressure and chemical potential of nitrogen in the gas atmosphere), different phases can be formed at the specimen surface. According to the Fe–N phase diagram, following phases can be formed for increasing chemical potential of nitrogen of the gas atmosphere: α-Fe (ferrite with dissolved nitrogen), γ'-Fe$_4$N and ε-Fe$_{2-3}$N. When nitriding is applied to form iron nitrides at the specimen surface (i.e. external nitriding), so called compound layer (also called "white layer" due to its appearance in light-optical micrographs) develops which improves the wear and corrosion resistance. Underneath the compound layer, if nitriding of iron-based alloys was performed in the α-region of the Lehrer diagram (i.e. internal nitriding, cf. section 1.1), nitrides of alloying elements precipitate within the

diffusion zone (i.e. nitrided zone) and this improves the fatigue properties of the steel components.

During gaseous nitriding, the chemical activity of nitrogen dissolved in the specimen at its surface can be controlled accurately by adjusting the partial pressure ratio of ammonia and hydrogen as expressed by the so-called nitriding potential, r_N $(= \dfrac{p_{NH_3}}{p_{H_2}^{3/2}})$. By adjusting the nitriding potential (and also the nitriding temperature), the phases occurring at the specimen surface can be controlled. Although nitriding treatments are widely adopted in industry, the application practice is still largely based on phenomenology, in particular concerning the nitriding of multicomponent systems. Therefore fundamental research of nitriding processes is needed.

Until now research on nitriding focused on relatively simple binary iron-based alloys. In practice, however, more than one alloying element occurs in conventional alloys. Typical alloying elements of steels to be nitrided are Ti, Cr and Al. The nitriding behaviour of *binary* Fe-Ti, Fe-Cr and Fe-Al alloys has been investigated extensively. However, there is sparse and ambiguous information about the nitriding behaviour of ferritic iron-based alloys which contain more than two alloying elements i.e. *ternary alloy systems* such as, Fe-Cr-Ti or Fe-Cr-Al. The present thesis focuses on the nitriding behaviour of such ternary iron-based alloys, in particular Fe-Cr-Me_2 (with Me_2 = Al or Ti), as function of the Cr/Me_2 atomic ratio.

5.2 Experimental

5.2.1 Specimen preparation

Ingots of Fe-Ti-Cr (cf. section 2 and 4) and Fe-Cr-Al (cf. section 3) alloys were prepared from pure Fe, pure Cr, pure Ti and pure Al using a light-arc furnace and inductive furnace, respectively. The molten alloys were cast as buttons (for Fe-Ti-Cr alloys) with a shape given by a diameter of 40 mm and a height of 15 mm, and rods (for Fe-Cr-Al alloys) with a diameter of 10 mm and length of 100 mm, respectively. The precise composition of the Fe-Me$_1$-Me$_2$ alloys was analyzed, applying (i) inductive coupled plasma-optic emission spectroscopy (ICP-OES) to determine the content of the alloying elements Cr and Ti (or Al), (ii) a combustion method to determine the light elements C and S and (iii) a hot-extraction to determine the light elements O and N. The cast buttons (or rods) were cold-rolled to foils. In order to reduce the rolling induced texture of the specimen, specimens of the as cast buttons (or rods) were rolled in different directions. The foils thus obtained were cut into rectangular specimens and subsequently ground and polished (last step: 1 µm diamond paste). The polished specimens were encapsulated in a quartz tube filled with Ar and annealed at 800°C (for Fe-Ti-Cr alloys) and 700°C (for Fe-Cr-Al alloys) for 2h to establish a recrystallized grain structure (grain size of about 30-50 µm). Before nitriding the specimens were again ground and polished (last step: 1 µm diamond paste) and cleaned ultrasonically with ethanol.

5.2.2 Nitriding

Nitriding was performed in a multizone quartz-tube furnace with an ammonia/hydrogen gas mixture flux at a given nitriding temperature of (560 or 580 ± 1)°C. The gas fluxes were precisely adjusted by mass-flow controllers. A linear gas velocity of 13.5 mm/s (at

room temperature) was established by keeping the gas flow rate at 500 ml/min in view of the inner diameter of 28 mm of the quartz tube furnace. This linear gas flow is sufficient to avoid any significant thermal decomposition of ammonia in the nitriding atmosphere.

5.2.3 Specimen characterization

Phase analysis was performed by means of X-ray diffraction (XRD) applied to the specimen surface of all specimens before and after nitriding. Detected phases were identified by the 2θ positions of their diffraction peaks.

Microhardness values before and after nitriding were performed by carrying out hardness measurements across the cross-section of specimens employing a Vickers microhardness tester.

The structure and morphology of the nitride precipitates were investigated by transmission electron microscopy (TEM) techniques. TEM samples taken at selected depths of the nitrided zone were produced by the jet-electropolishing technique. Bright field images (BF), dark field images (DF) and selected area diffraction patterns (SADPs) were used to determine the (crystal) structure and the morphology of the nitride precipitates. In order to reveal the elemental distribution of the nitride precipitates, electron energy loss spectroscopy (EELS) was performed.

Elemental concentration depth profiles were determined by electron probe microanalysis (EPMA) performed on cross-sections perpendicular to the surface of nitrided specimens, starting from the surface across the cross-section towards the unnitrided core of the specimen.

5.3 Results

5.3.1 Nitride formation and excess nitrogen uptake upon nitriding ferritic Fe-Ti-Cr alloys

Nitriding of ternary iron-based Fe-Ti-Cr alloys leads to the precipitation of highly coherent cubic, rock-salt crystal-structure type, mixed $Ti_{1-x}Cr_xN$ nitrides in the ferrite matrix. Separate TiN and CrN nitrides do not develop. Uptake of Cr in TiN is favored as it reduces the misfit-strain field in the ferrite matrix. The misfit of the largely coherent nitride precipitates with the surrounding ferrite matrix is strongly anisotropic. As a consequence the nitride precipitates develop as platelets (length $\leq$ 30 nm and thickness $\leq$ 3 nm) obeying a Bain orientation relationship with the ferrite matrix with $\{100\}_{\alpha\text{-Fe}}$ habit planes, and are surrounded by a tetragonally distorted ferrite matrix. As a result cubic and tetragonal ferrite reflections can be discerned in both X-ray diffraction and selected area electron diffraction patterns. The lattice parameter of the mixed $Ti_{1-x}Cr_xN$ nitride increases with increasing Ti/Cr atomic ratio. Consequently the misfit-strain field is most pronounced for the highest relative Ti content of the alloy, which corresponds with a microhardness increasing with increasing Ti/Cr atomic ratio.

The amount of excess nitrogen dissolved in the ferrite matrix, $[N]_{strain}$, increases with increasing Ti/Cr atomic ratio as a consequence of a tensile hydrostatic component of misfit stress increasing with increasing Ti/Cr atomic ratio. The amount of excess nitrogen adsorbed at the nitride-platelet faces, $[N]_{interface}$, increases with increasing Ti/Cr atomic ratio because (i) Ti has a much larger affinity for N than Cr and (ii) the relative amount of interfacial (nitride/matrix) area increases with increasing Ti/Cr atomic ratio.

5.3.2 Normal and excess nitrogen uptake by iron-based Fe-Cr-Al alloys

Upon nitriding of Fe-Cr-Al alloys, metastable, mixed $Cr_{1-x}Al_xN$ nitrides of cubic, rock-salt crystal-structure type precipitate in the ferrite matrix; the system thus avoids the difficult nucleation of stable AlN (hexagonal, wurtzite structure type) precipitates in the ferrite matrix. The ease of mixed nitride nucleation and thus the nucleation density increase with increasing Cr/Al atomic ratio. Such an effect does not occur for nitrided Fe-Cr-Ti alloys as both equilibrium nitrides, CrN and TiN, have the same (rock-salt type) crystal structure as the corresponding metastable mixed $Cr_{1-x}Ti_xN$ precipitate. The degree of coherency at the $Cr_{1-x}Al_xN$-platelet faces increases with increasing Cr/Al atomic ratio (TEM analysis), which reflects the decrease of the absolute value of the linear misfit parameter parallel to the interface, $\left|\delta_{//}\right|$, with increasing Cr/Al atomic ratio (for the alloys investigated within the range 0.21-2.00), opposite to the trend for the overall misfit parameter, ε.

The amount of excess nitrogen adsorbed at the faces of the nitride platelets, $[N]_{interface}$, increases with decreasing Cr/Me_2 (Me_2 = Al or Ti) atomic ratio because the chemical affinity of Me_2 for N is much larger than that of Cr for N and because the thickness of the nitride platelets decreases with decreasing Cr/Me_2 atomic ratio. The amount of excess nitrogen dissolved in the ferrite matrix, $[N]_{strain}$, *increases* with increasing Cr/Me_2 atomic ratio for Me_2 = Al and *decreases* with increasing Cr/Me_2 atomic ratio for Me_2 = Ti. These antagonistic behaviours can be understood as consequences of the overall nitride/matrix misfit increasing with increasing Cr/Al atomic ratio and decreasing with increasing Cr/Ti atomic ratio.

5.3.3 The kinetics of the nitriding of ternary iron-based Fe-2at.%Cr-2at.%Ti alloy

The development of the nitrogen-concentration depth profile is well described by a numerical diffusion model, developed and applied in this work, which defines the role of *mobile excess nitrogen* (dissolved in the ferrite matrix), and *immobile excess nitrogen* (adsorbed at the matrix/nitride precipitates interface). The results obtained are compatible with the precipitation of *mixed $Cr_{1-x}Ti_xN$ nitride*, in agreement with the TEM data.

The mobile excess nitrogen has a pronounced influence on the increase of the diffusion-zone depth, whereas the immobile excess nitrogen influences the content (i.e. height) of nitrogen of the nitrided zone.

Chapter 6

Zusammenfassung

6.1 Einführung

Gasnitrieren ist eine bedeutende thermochemische Oberflächenbehandlungsmethode von ferritischen Stahlkomponenten. Sie dient zur Verbesserung von technischen Eigenschaften wie Ermüdung, Abrieb und Korrosionsbeständigkeit. Das Gasnitrieren wird üblicherweise in einer Ammoniak/Wasserstoffatmosphäre bei Temperaturen zwischen 500 und 580°C (dies entspricht 773 bis 853K) und 1atm Druck durchgeführt. In Abhängigkeit der Nitrieratmosphäre und der Nitriertemperatur kann dies einigen 1000 atm einer reinen Stickstoffatmosphäre entsprechen.

Der in den Ofen eingeleitete Ammoniak dissoziiert an der Probenoberfläche. Die dabei frei werdenden Stickstoffatome können in die Ferritmatrix eindiffundieren. In Abhängigkeit der Nitrierbedingungen (Nittiertemperatur, Druck und chemisches Potential des Stickstoffs in der Gasatmosphäre) können unterschiedliche Phasen an der Probenoberfläche erzeugt werden. Gemäß dem Fe-N Phasendiagramm können die folgenden Phasen bei Erhöhung des chemischen Potentials von Stickstoff gebildet werden: γ'-Fe$_4$N, ε-Fe$_{2-3}$N. Falls die Nitrierparameter so gewählt werden, dass Eisennitride an der Probenoberfläche entstehen bildet sich eine Verbindungsschicht aus. Die Verbindungsschicht weist gute Abriebs- und Korrosionseigenschaften auf. Unter der Verbindungsschicht schließt sich die Diffusionsschicht an, welche, falls Fe-M Legierungen (mit M als Nitridbildnern) nitriert worden sind, Nitridausscheidungen enthält. Die Diffusionszone in der Nitrierschicht verbessert die

Ermüdungseigenschaften. Während des Gasnitrierens kann die chemische Aktivität des in der Probenoberfläche gelösten Stickstoffs sehr präzise, durch Änderung des Partialdruckverhältnisses zwischen Ammoniak und Wasserstoff (auch als Nitrierkennzahl $r_N = \dfrac{p_{NH_3}}{p_{H_2}^{3/2}}$ bezeichnet), eingestellt werden. Durch Variation der Nitrierkennzahl kann somit die Bildung der Oberflächenphase kontrolliert werden. Obwohl das Nitrieren ein sehr weit verbreitetes Oberflächenbehandlungsverfahren in der Industrie ist, basiert die Anwendungspraxis überwiegend auf phänomenologischen Grundlagen. Dies gilt insbesondere für das Nitrieren von Mehrkomponentensystemen. Grundlagenforschung im Bereich des Nitrierens ist daher erforderlich.

Bislang wurde überwiegend das Nitrierverhalten von einfachen (binären) Modelsystemen untersucht. In der Anwendung werden üblicherweise Stähle mit mehr als einer Legierungskomponente nitriert. Typische Legierungselemente in Nitrierstählen sind Ti, Cr und Al. Das Nitrierverhalten von Fe-Ti, Fe-Cr, und Fe-Al Legierungen ist intensiv untersucht worden. Allerdings gibt es relativ wenig Kenntnis über das Nitrierverhalten von Legierungen mit mehr als zwei Legierungskomponenten, z.B. ternäre Legierungen wie Fe-Cr-Ti oder Fe-Cr-Al. Der Schwerpunkt der vorliegenden Dissertation liegt auf der Untersuchung des Nitrierverhaltens von ternären Legierungssystemen, insbesondere Fe-Cr-Me$_2$ (mit Me$_2$= Al oder Ti) als Funktion des Atomverhältnisses Cr/Me$_2$.

6.2 Experimentelles

6.2.1 Probenpräparation

Abgüsse von Fe-Ti-Cr (siehe Kapitel 2 und 4) und Fe-Cr-Al (siehe Kapitel 3) Legierungen wurden aus reinem Fe, reinem Cr, reinem Ti und reinem Al, mit Hilfe eines Lichtbogen- und eines Induktionsofens, hergestellt. Die Fe-Ti-Cr Legierungen Legierungen wurden in Form von Knöpfen, mit einem Durchmesser von ca. 40mm und einer Höhe von 15mm, gegossen. Die Fe-Cr-Al Legierungen wurden in Form eines Zylinders, mit einem Durchmesser von 10 mm und einer Länge von 100 mm, abgegossen. Die genaue Zusammensetzung der Fe-Me$_1$-Me$_2$ Legierungen wurde durch die Anwendung von (i) „inductive coupled plasma-optic emission spextroscopy" (ICP-OES) für die Bestimmung der Konzentrationen von Cr und Ti (oder Al), (ii) „combustion method" für die Bestimmung der Konzentrationen der leichten Elemente C und S und (iii) „hot extraction" zur Bestimmung der Konzentrationen der leichten Elemente O und N ermittelt. Die gegossenen Knöpfe bzw. Zylinder wurden zu Folien kaltgewalzt. Um die Walztextur zu vermindern wurden die Abgüsse in unterschiedlichen Richtungen gewalzt. Aus den Folien wurden rechteckige Proben geschnitten. Die erhaltenen Folien wurden geschliffen und poliert (bis zu einer Körnung von 1 µm). Die so präparierten Folien wurden in einer mit Argon gefüllten Quarzampulle eingekapselt und bei 800°C (für die Fe-Ti-Cr Legierungen) sowie 700°C (für die Fe-Cr-Al Legierungen) für 2h ausgelagert, um eine rekristallisierte Mikrostruktur zu erhalten (Korngrenze ca. 30-50 µm).

Vor dem Nitrieren wurden die Proben ein weiteres Mal geschliffen poliert (bis zu einer Körnung von 1 µm) und im Ethanol-Ultraschallbad gereinigt.

6.2.2 Nitrieren

Das Nitrieren wurde in einem Mehrzonenofen unter einem Ammoniak/Wasserstoff Gasfluss bei den Temperaturen 560°C oder 580°C ± 1°C durchgeführt. Die Gasflüsse wurden exakt durch Massenflussregler eingestellt. Es wurde eine lineare Gasgeschwindigkeit von 13.5 mm/s (bei Raumtemperatur) eingestellt. Diese Geschwindigkeit ergibt sich aus der Gasflussrate von 500 ml/min bei einem Ofeninnendurchmesser des Quarzrohres von 28 mm.

6.2.3 Probencharakterisierung

Bei allen Proben wurde eine Phasenanalyse mittel Röntgendiffraktometrie (XRD) vor und nach dem Nitrieren durchgeführt. Auftretende Phasen wurden anhand ihrer 2θ Position im Diffraktogramm identifiziert.

Mikrohärtetiefenprofile wurden durch die Durchführung von Härtemessungen über den Probenquerschnitt, mittels eines Vickers-Mikrohärteprüfgerätes, erstellt.

Die Struktur und Morphologie der Nitridausscheidungen wurde durch Transmissionselektronenmikroskopie (TEM) untersucht. TEM Proben wurden an unterschiedlichen Probentiefen der Nitrierschicht entnommen und durch Jet-Elektropolieren präpariert. Hellfeld-, Dunkelfeldaufnahmen und Beugungsbilder wurden herangezogen um die Kristallstruktur und die Morphologie der Nitridausscheidungen zu bestimmen. Um die Elementverteilung der Nitridausscheidungen zu bestimmen, wurde „electron energy loss spectroscopy (EELS) durchgeführt.

Elementkonzentrationstiefenprofile wurden durch die Mikrosonde gemessen. Dabei wurde die Elementzusammensetzung der Probe, entlang von Messpunkten, über den Probenquerschnitt (senkrecht zur Probenoberfläche), bestimmt.

6.3 Ergebnisse

6.3.1 Nitridbildung und Überschussstickstoffaufnahme beim nitrieren von ferritischen Fe-Ti-Cr Legierungen

Das Nitrieren von ternären eisenbasierten Fe-Ti-Cr Legierungen führt zur Bildung von kohärenten kubischen $Ti_{1-x}Cr_xN$ Nitriden in der Ferritmatrix. Separate TiN und CrN treten nicht auf. Die Aufnahme von Cr in TiN ist begünstigt da hierdurch die Fehlpassungs-Spannungsfelder in der Ferritmatrix reduziert werden. Die Fehlpassung der kohärenten Nitridausscheidungen mit der umliegenden Ferritmatrix ist stark anisotrop. Als Resultat treten die Nitridausscheidungen plattenförmig (Länge < 30 nm und Dicke < 3 nm) auf und weisen eine Bain Orientierungsbeziehung zur umgebenden Ferritmatrix mit $\{100\}_{\alpha\text{-Fe}}$ habitus Ebenen auf. Die Ausscheidungen sind von einer tetragonal verzerrten Ferritmatrix umgeben. Als Konsequenz treten sowohl kubische als auch tetragonale Reflexe in den Röntgendiffraktogrammen und TEM Beugungsbildern auf. Die Gitterparameter der Mischnitride $Ti_{1-x}Cr_xN$ erhöhen sich mit zunehmendem Ti/Cr Atomverhältniss. Folglich treten die größten Fehlpassungsspannungen bei den größten Ti Konzentrationen auf. Dies wird durch steigende Härtewerte mit zunehmendem Ti/Cr Atomverhältnis bestätigt.

Der Anteil von Überschussstickstoff, gelöst in der Eisenmatrix, $[N]_{strain}$, steigt an mit wachsendem Ti/Cr Atomverhältnis, als Folge einer Zug hydrostatischen Komponente der Fehlpassungsspannung mit steigendem Ti/Cr Atomverhältnis.

6.3.2 Normalstickstoff und Überschussstickstoff Aufnahme durch eisenbassierte Fe-Cr-Al Legierungen

Während dem Nitrieren von Fe-Cr-Al Legierungen bilden sich metastabile Mischnitride $Cr_{1-x}Al_xN$ mit einer kubischen Steinsalzkristallstruktur in der Ferritmatrix; auf diese

Weise umgeht das System der schwierigen Keimbildung von stabilem AlN (hexagonal, Wurtzitstrukturtyp) in der Ferritmatrix. Die leichte Mixnitridkeimbildung und somit die Keimbildungsdichte steigt mit wachsendem Cr/Al Atomverhältnis. Dieser Effekt tritt nicht für nitrierte Fe-Cr-Ti Legierungen auf, da beide Gleichgewichtsnitride CrN und TiN die gleiche Steinsalzstruktur aufweisen wie die entsprechende Mischnitridausscheidung $Cr_{1-x}Ti_xN$. Der Grad der Kohärenz an den Grenzflächen der $Cr_{1-x}Al_xN$ nimtt mit steigendem Cr/Al Atomverhältnis zu (TEM Analyse). Dies zeigt die Abnahme des absoluten linearen Fehlpassungsparameters, parallel zur Grenzfläche, δ, mit zunehmenden Cr/Al Atomverhältnis (für die Legierungen untersucht im Bereich zwischen 0.21-2.00), im Gegensatz zum Trend für den Fehlpassungsparameter ε.

Der Betrag des Überschussstickstoffes welcher an der Grenzfläche der Nitidplättchen adsorbiert ist $[N]_{interface}$ steigt mit sinkendem Cr/Me_2 (Me_2 = Al oderTi) Atomverhältnis, da die chemische Affinität für Me_2 für N wesentlich größer ist als die von Cr zu N, und da die Dicke der Nitridplättchen mit sinkendem Cr/Me_2 Atomverhältnis abnimmt. Der Betrag an Überschussstickstoff welcher in der Ferritmatrix $[N]_{strain}$ gelöst ist, nimmt mit steigendem Cr/Me_2 Atomverhältnis für Me_2=Al zu und nimmt für ein steigendes Cr/Me_2 Atomverhältnis, für Me_2=Ti, ab.

6.3.3 Die Kinetik des Nitrierens von ternären Eisen-Basis Fe-aat.%Cr-2at.%Ti Legierungen

Die Entstehung von Stickstoff-Konzentrationstiefenprofilen ist sehr gut durch ein numerisches Diffusionsmodell, welches die Rolle des mobilen Überschussstickstoffs (gelöst in der Ferrit Matrix), und die Rolle des immobilen Überschussstickstoffs (adsorbiert an der Matrix/Nitrid Ausscheidungsgrenzfläche) definiert. Die ermittelten

Resultate stimmen mit der Ausscheidung von Mischnitriden $Cr_{1-x}Ti_xN$, in Übereinstimmung mit den TEM Daten.

Der mobile Überschussstickstoffanteil hat einen deutlichen Einfluss auf die Erhöhung der Diffusionszonentiefe, wohingegen der immobile Überschussstickstoff den Stickstoffanteil der nitrierten Schicht beeinflusst.

Curriculum Vitae

Personal data:

Name: Kyung Sub Jung

Date of birth: 31st January 1980

Place of birth: Busan, South Korea

Nationality: Republic of Korea (South Korea)

Schooling:

1986-1992   **Yongho Elementry school**: Yongho Dong, Busan, South Korea

1992-1995   **Yongho Middle school**: Yongho Dong, Busan, South Korea

1995-1998   **Dongchun High school**: Daeyeon Dong, Busan, South Korea

Higher education:

1998-2005   **Hanyang University, Seoul, South Korea**

                B.Sc. at Faculty of Materials Science and Engineering

2005-2007   **Hanyang University, Seoul, South Korea**

                M.Sc. at Faculty of Materials Science and Engineering

                Laboratory of Physical Metallurgy "Prof. K.S. Lee"

                Thesis title: *Study of hydrogenation properties of Mg based*
                composite metal hydride prepared by adding metal oxide/
                Li based metal hydride

Dissertation:

2007-2011   **Max Planck Institue for Intelligent Systems (formerly Max**
                Planck Institute for Metals Research), Stuttgart, Germany
                and Institue for Materials Research, University of Stuttgart

                PhD student at Department Prof. Dr. Ir. Eric J. Mittemeijer

                Research Theme: *Nitriding of Iron-based ternary alloys;*
                Fe-Ti-Cr and Fe-Cr-Al

Acknowledgements

The present work was performed at the Institute for Materials Science of the University of Stuttgart and at the Max Planck Institute for Intelligent Systems (formerly Max Planck Institute for Metals Research), Stuttgart.

First of all, I would like to thank my research supervisor Prof. Dr. Ir. E.J. Mittemeijer for accepting me as a PhD student in his department. I would like to thank him for his outstanding commitment and encouragement, the continuous supervision and the numerous scientific discussions which have considerably contributed to the completion of this work.

I wish to express my sincere appreciation to two other members of my PhD examination, Prof. Dr. J. Bill and Prof. Dr. Th. Schleid, for reviewing my PhD thesis and making constructive comments on this research.

Special thanks to my daily supervisors Dr. R.E. Schacherl and Dr. E. Bischoff for their continuous co-operation and discussions. They have considerably contributed to the successful completion of this work.

I am grateful to all the colleagues and co-workers at the Max Planck Institute in Stuttgart, for their assistance during my research and residence in Stuttgart.

I especially want to thank my Korean friends (and also their families), my friends in the Dept. Mittemeijer (in particular Eric, Holger, Thomas and Sairam) and my IMPRS-AM friends who made my stay in Stuttgart pleasant and enjoyable.

Finally, I feel extremely grateful to my beloved family in Korea for their endless love, support and encouragement.